FINGER-POWERED THERMOPLASTIC MICROFLUIDIC ELECTROCHEMICAL ASSAY FOR DIAGNOSTIC TESTING USING A MOBILE PHONE

By

Tung-Yi Lin

A DISSERTATION

Submitted to
Michigan State University
in partial fulfillment of the requirements
for the degree of

Mechanical Engineering – Doctor of Philosophy

2018

ABSTRACT

FINGER-POWERED THERMOPLASTIC MICROFLUIDIC ELECTROCHEMICAL ASSAY FOR DIAGNOSTIC TESTING USING A MOBILE PHONE

By

Tung-Yi Lin

Point-of-care (POC) testing has gained considerable attention in recent years due to its ability to provide diagnostic information without the need for centralized laboratory facilities or bulky equipment. This has been achieved, in part, by advances in micro-electro-mechanical system (MEMS) and analytical chemistry, which has resulted in the miniaturization and integration of sensitive biosensors and fluidic components. Recently, researchers have demonstrated the use of mobile phones for POC testing, which offers the advantages of portability and wireless data transmission. Many mobile phone-based POC tests are based on optical imaging or colorimetric assays, which are useful for some diagnostic applications, but lack the accuracy and sensitivity required for the diagnosis of many important diseases. Moreover, these devices employ microfluidic chips fabricated using glass, polydimethylsiloxane (PDMS) or paper, which require complex microfabrication or surface treatments, or offer limited fluidic control.

In this dissertation, we explored the development of plastic-based microfluidic chips for rapid electrochemical measurements of protein biomarkers using a mobile phone biosensing platform. We first investigated UV/ozone (UVO) surface treatment on plastics to better understand its usefulness for microfluidic POC applications. We found that UVO-treated poly(methyl methacrylate) (PMMA), cyclic olefin copolymer (COC) and polycarbonate (PC) experience hydrophobic recovery within 4 weeks and the rate at which it occurs is dependent on the UVO treatment duration. Furthermore, we discovered that the hydrophobic recovery of UVO-treated COC and PC can be inhibited by storing them in dehumidified or vacuum conditions. UVO-treated plastics were also used for protein adsorption measurements, which showed that UVO treatment minimized protein adsorption and this effect is correlated with the treatment duration. Lastly, we

demonstrated capillary-driven flows in UVO-treated PMMA microchannels, which revealed that the flow rate can be tuned by adjusting the treatment duration.

We also explored the development of new fabrication methods for generating plastic microfluidic devices. In particular, we have demonstrated for the first time the use of 3D printed metal molds for fabricating plastic microchannels via hot embossing. Through the optimization of the powder composition and processing parameters, we generated stainless steel molds with superior material properties (density and surface finish) and replication accuracy compared with previously reported 3D printed metal parts. 3D printed molds were used to fabricate PMMA replicas, which exhibited good feature integrity and replication quality. Microchannels fabricated using these replicas exhibited leak-free operation and comparable flow performance as microchannels fabricated from CNC milled molds for both capillary and pressure-driven flows.

Toward the realization of a shelf stable, electricity-free microfluidic assay for POC testing, we developed a finger-powered microfluidic chip for electrochemical measurements of protein biomarkers. This device employs a valveless, piston-based pumping mechanism which utilizes a human finger for the actuation force. Liquids are driven inside microchannels by pressing on a mechanical piston, which generates a pressure-driven flow. Dried reagents are preloaded in microwells allowing for the entire testing process to be completed on-chip. Additionally, a nonenzymatic detection scheme is employed which circumvents the need for refrigeration. For proof-of-concept, this microfluidic assay was coupled with a mobile phone biosensing platform for quantitative measurements of *Plasmodium falciparum* histidine-rich protein-2 (*Pf*HRP2) in human blood samples. Using this platform, *Pf*HRP2 was detected from 1 to 20 μg/mL with high specificity and each measurement could be completed in ≤ 5 min. In addition, this assay can be stored at room temperature for up to one month with a negligible loss in performance. The results and knowledge presented in this dissertation will provide new insights into the development of plastic microfluidic devices for POC testing as well as other biomedical application.

ACKNOWLEDGEMENTS

This dissertation is the product of my four years efforts since I joined the MSU program in 2013. It was a truly great memory in my life. First and foremost, I would like to thank the guidance of my advisor, Dr. Peter Lillehoj. He has taught me a lot regarding to the projects, course works and the career paths. He is knowledgeable and willing to support all the students. I'm really grateful for his contributions through my PhD years. In addition, I would like to thank all my committee members, including Dr. Wen Li, Dr. Junghoon Yeom and Dr. Manoochehr Koochesfahani. Without they're insightful inputs and valuable comments to my works, I couldn't complete this project.

My gratitude also goes to my labmates that I have met in MSU. First, I would like to Xiyuan Liu, my first labmate, who always generously shared her research experience with me. I also appreciate her advise and help through my PhD years. Furthermore, thanks to Zoe Jiang for her efforts and helps for maintaining the lab. I would like to thank to Trey Pfeiffer, an undergraduate student in mechanical engineering department. He's the smartest undergraduate that I have met in MSU. In addition to his tremendous contribution in the projects, he's actually one of my best friends. He is willing to share his life and entertainments with me and make my PhD career interesting.

Moreover, I would like to extend my acknowledgements to all the faculties supported me within four years. Thanks to one of my collaborators, Dr. Patrick Kwon provided suggestions and supports to the 3D metal printing project. Thanks to Kathryn Severin for her assistance with UV-visible spectroscopy and contact angle measurements. Thanks to Dr. Baokang Bi and Matthew Oonk for their assistance with cleanroom facilities. Thanks to Brian Wright for his supports with the 3D printing and surface profilometer measurement. Thanks to Dr. Per Askeland for his assistance with XPS measurement and element analysis. Thanks to Dr. Reza Loloee and Dr. Melinda Frame for the assistance of microscopy.

Thanks to my main funding source National Institutes of Health organization. This work was funded by the NIH (R01AI113257). I would like to thank to my teammates involved in this project, Sina Parsenjad and Linlin Tu. Sina Parsenjad helped me with development of couple generation circuit devices. He is a friendly person and reachable all the time when I faced electrical problems. Linlin developed a phone application and constantly improved the application interface. For development the prototype, we had many difficulties, and finally achieved all these challenges. I sincerely thank to their patience and contributions for this project. Moreover, I thank Dr. Gorachand Dutta for his assistance with designing and troubleshooting the detection scheme and also thank Dr. Hao Wan for developing the PC software used for recording the sensor data. Thanks to all the collaborators involved in this project, including Dr. Andrew Mason, Dr. Guoliang Xing, Dr. Terrie Taylor, Dr. Karl Seydel and Dr. Mat Reeves.

Lastly, I would like to thank to my family, my friends and my girlfriend, Ting-Wei Lee. I really appreciate their unconditional love and encouragement. They accompany me through entire my PhD career, and bring me a powerful strength in my life.

TABLE OF CONTENTS

LIST OF TABLES

LIST OF FIGURES

Chapter 1. Introduction

1.1 Point-of-care testing

The ability to diagnose patients accurately and promptly is important for subsequent treatment and disease management. In recent years, diagnostic testing has shifted from conventional lab-based assays to point-of-care (POC) tests to reduce the time and costs associated with such testing (Fig. 1-1) [1]. This is especially true for resource-limited countries, which have limited infrastructure, such as continuous electricity and diagnostic equipment. In these regions, patients have difficulty accessing centralized medical facilities due to a lack of resources for transportation, which ultimately hinders treatment. In industrialized countries, such as the U.S., the time required to run many diagnostic tests is long (> 6 hr), which results in multiple return visits and missed opportunities for effective treatments [2]. Therefore, providing fast turnaround results can help medical care providers take appropriate actions and further improve health outcome. POC assays are designed to be simple, rapid, and low cost, making them well suited for medical diagnosis. In addition, POC testing can help medical personnel provide proper clinical management, making it a useful technology for both resource-limited settings and the developed world.

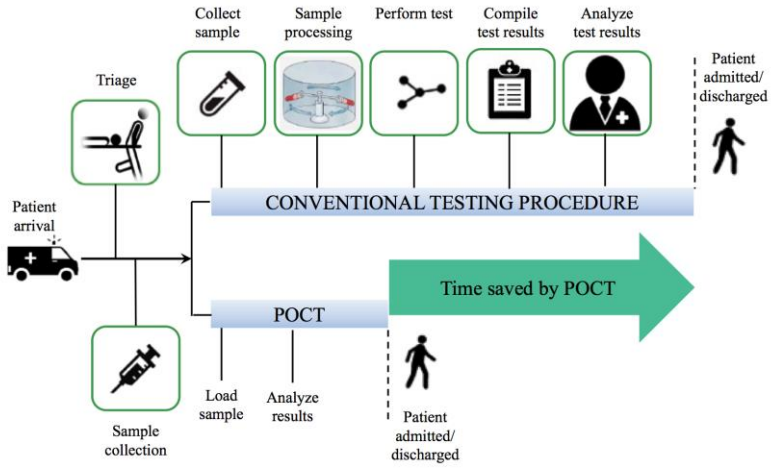

Figure 1-1. Procedures for conventional lab-based diagnostics compared to point-of-care (POC) testing. Image obtained from [1].

A POC device typically employs a biosensor, which is an analytical device for qualitative or quantitative measurements of biomolecular components using a physical-chemical detector [3]. A biosensor typically consists of three components: bioreceptors, transducer and electronics [4] (Fig. 1-2). Bioreceptors are biological elements (proteins, nucleic acids) used for sample recognition, the transducer converts the signal resulting from interaction with analyte to an electrical signal, and the electronics output the signal to the reader as well as performs any needed signal processing (amplification, filtering, etc.). Combining the transducer and electronics can simplify and minimize the size of biosensor. Biosensors can be classified by their physical-chemical properties of the selected transducer, such as thermal, optical, electrical and electrochemical.

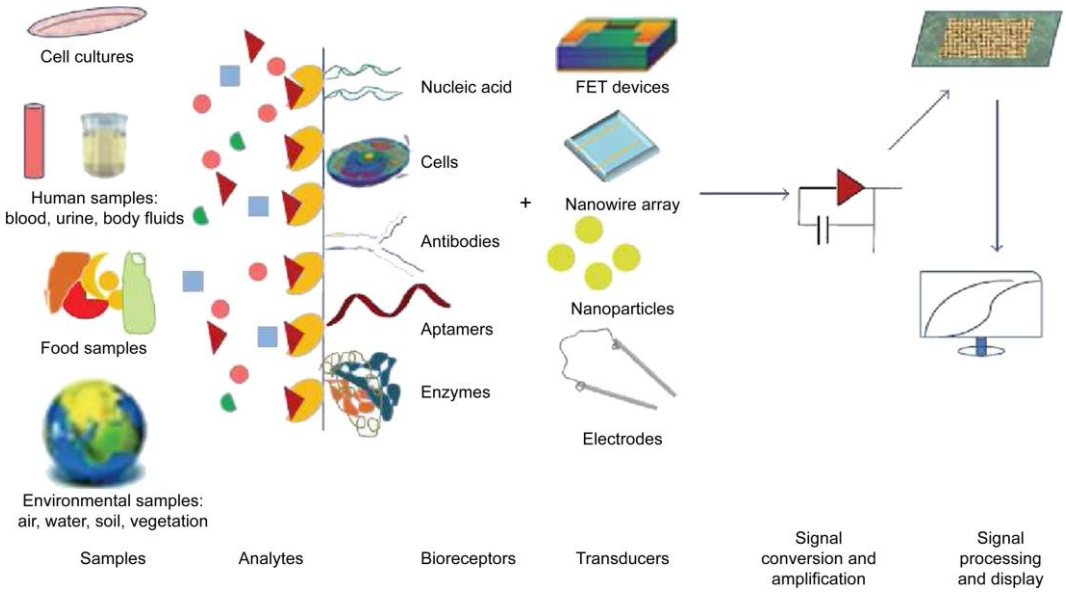

Figure 1-2. Major elements of a typical biosensor. Image obtained from [4].

Lateral flow assays (LFA), such as home pregnancy tests, are one of the simplest and most common types of POC diagnostic devices. LFAs were first introduced in 1980s [5] for pregnancy testing and since then, have been applied to other applications, including infectious disease detection, water/food safety, agricultural contaminants surveillance and drug screening [6]. LFA is

a qualitative test for the detection of analytes in biofluids, where the sample is transported via capillary force on a paper strip and the results are displayed within 5–30 min [7]. LFAs typically contain a control line to confirm the test results and one or more test lines for the target analyte(s). While LFAs are valuable for some POC applications, they only provide qualitative results, which is not useful for diagnostic applications that require biomarker quantification, resulting in the need for advanced POC technologies.

1.2 Electrochemical biosensors

There are two main detection methods for measuring analytes in biofluids: optical (fluorescence, colorimetric) and electrical (electrochemical, impedance). Colorimetric is a popular technique since it is rapid, simple and easy to fabricate. It is a method to determine the concentration of analyte based on the color change. However, the false positive or false negative signal could be generated from the background color, which results in an inaccurate measurement. Recently, the role of electrochemical immunosensors in clinical analysis has increased significantly due to their high selectivity and sensitivity [8]. More than half of the biosensors applied for detection of pathogens are based on electrochemistry technology [9]. Since it is low cost, highly sensitive, and portable, electrochemical biosensors are the most favorable among all sensing techniques.

The sensing principle for an electrochemical biosensor is based on an electrochemical reaction between a reporter molecule and a substrate solution, which results in the generation of an electrical signal based on current (amperometric or cyclic voltammetry), potential (potentiometry) or charge (coulometry) as shown in Fig. 1-3 [3]. Alternatively, electrochemical impedance spectroscopy (EIS) detects changes in the capacitance and resistance properties of electrode surface due to analyte binding.

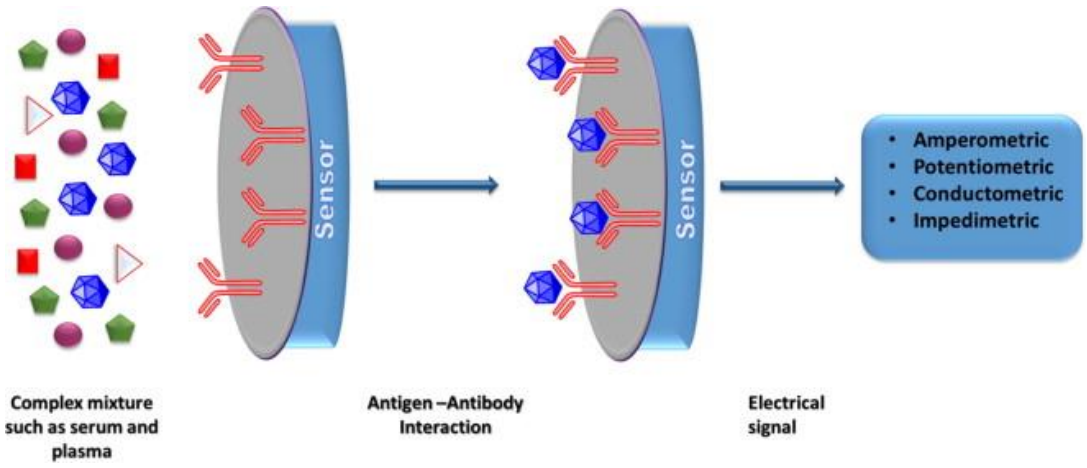

Figure 1-3. Process flow of a typical biosensor. Image obtained from [3].

1.2.1 Immobilization of bioreceptors

The immobilization of the bioreceptors is one of the most important aspects for developing a biosensor. The analytical performance and stability of the biosensor are both heavily influenced by the immobilization process. There are several methods to immobilize bioreceptors on a sensor surface, including entrapment, adsorption, covalent bonding, cross-linking and affinity interactions, as shown in Fig. 1-4 [11].

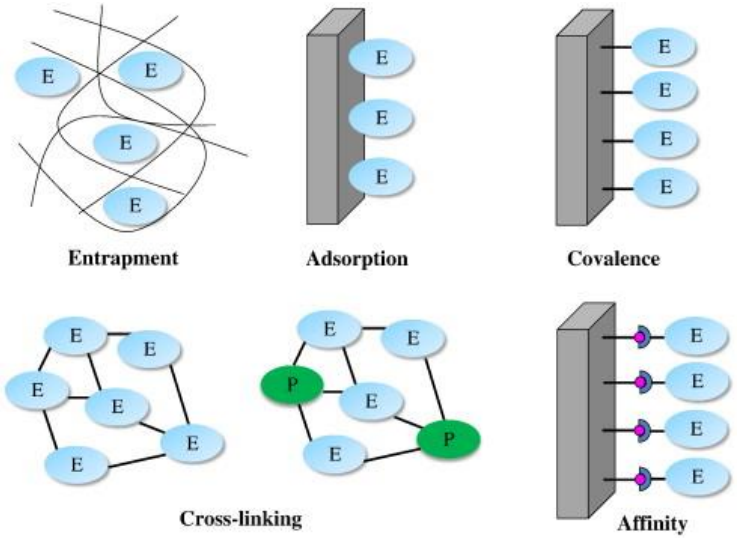

Figure 1-4. Schematic of main methods for immobilizing bioreceptors on a senor surface. Image obtained from [11].

1.2.2 Principle of electrochemical sensing

An electrochemical biosensor consists of several components, including sensing electrodes, potentiostat, and a read-out device. A typical electrochemical setup is based on a three-electrode potentiostat, including a working electrode, reference electrode and counter electrode as shown in Fig. 1-5 [8,9]. The working electrode is where the reaction occurs, which must be a stable material, such as carbon or gold. The reference electrode maintains its potential and is used as a reference for measuring changes in electrical properties of the working electrode. The counter electrode allows electric charge to flow, thus, there is no current flow between working electrode and reference electrode, resulting in a stable potential. The voltage between working electrode and reference electrode is controlled by the potentiostat. An electrochemical process involves a redox (reduction and oxidation) reaction where electrons are transferred from a chemical substance that is oxidized to one that is being reduced, and both oxidation and reduction processes occur simultaneously. For example, reduction is the gaining of electrons from the oxidation process, which loses electrons. The energy of the electrodes is raised when a negative potential is applied, and results in electrons required from electrode to solution (reduction current occurs). On the other hand, the energy can be lowered when a positive potential is applied, which results in an oxidation current.

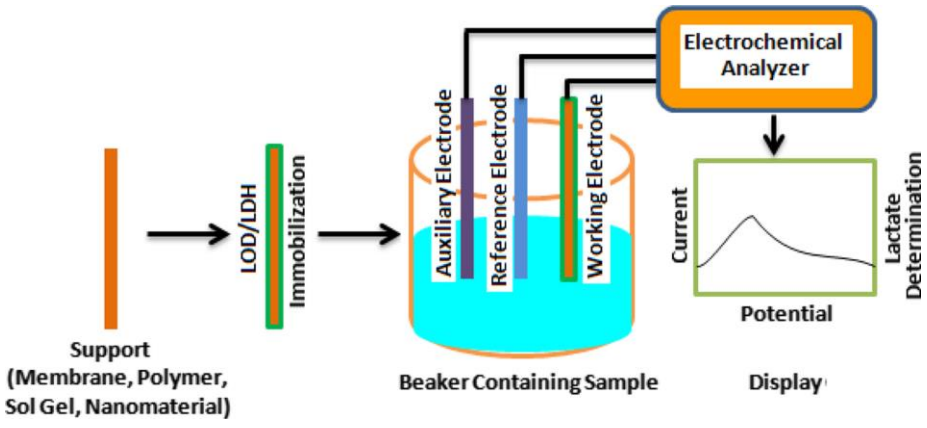

Figure 1-5. Example of an electrochemical measurement process for the detection of lactate. Image obtained from [9].

1.2.3 Amperometric biosensors

Amperometry is one of the most popular methods for the development of analytical biosensors, which is also the most sensitive techniques of all electrochemical sensing methods [14]. In this technique, a fixed potential is applied between the working and reference electrodes, and the resulting current signal is measured. The magnitude of the applied voltage is based on an oxidation or reduction generated from electroactive species on the sensor surface. The concentration of the target analyte in the sample is linearly proportional to the peak value of generated current. Amperometry usually requires an external potentiostat for generating electrical signals on the electrodes, as well as an external electronics to read out the results. However, combining the transducer and electronics together can significantly reduce the overall device size and improve device performance [15].

Clark *et al.* demonstrated the first electrochemical sensor for glucose detection based on oxygen sensors. In this device, glucose and oxygen undergo a redox reaction in the presence of glucose oxidase [16]. Subsequently, numerous diagnostic applications based on amperometry have been developed and many tangible applications of amperometry techniques have been developed. Liu *et al.* developed an enzyme-free sensor employing nanocubes with graphene as electrocatalysts for the detection of glucose and H_2O_2 [17]. The biosensor exhibited a linear response from 0.3 mM to 3.3 mM, and a lower detection limit of 3.3 μM in buffer solution. Ruecha *et al.* demonstrated a paper-based nanocomposite biosensor for the amperometric determination of cholesterol [18]. This biosensor exhibited a lower detection limit of 1 μM with detection range from 50 μM to 10 mM in human serum. To achieve a high sensitivity and selectivity, an appropriate bioassay design and parameter optimization are needed.

There are various methods for fabricating electrodes for electrochemical sensors, including screen-printing and thin-film deposition. Screen-printing is a popular technique due to its low cost, simplicity and scalability. Screen-printed biosensors have been developed for oxygen detection

[19], protein detection [20,21], blood glucose sensing [22], monitoring metal compositions in pesticide detecting [23], and water samples [24]. In screen-printing, the desired electrode material is forced through a custom screen, forming the desired electrode shape on substrate, followed by air drying. While fast and simple, controlling the uniformity of the electrode surface is challenging and prone to defects, which can hinder the analytical performance. In thin-film deposition, material is deposited through a shadow mask onto the substrate via evaporation or sputtering. Although thin-film deposition is more complicated than screen-printing, it can generate 10× smaller features, offers better repeatability and improved surface uniformity.

1.3 Microfluidic-based electrochemical biosensors

Most diagnostic tests are performed using bodily fluids (blood, urine, saliva) which commonly require sample preparation for purifying/concentrating the analytes. In addition, many assays, such as enzyme-linked immunosorbent assay (ELISA) and reverse transcription-polymerase chain reaction (RT-PCR), involve multiple sample processing steps which is time consuming and laborious. To address these limitations, researchers have utilized microfluidics for sample preparation and fluidic processing, which offers the advantages of small sample and reagent volumes (which range from μL to nL), precise fluid control, and fast processing time. For these reasons, biosensors are integrated with microfluidic components, resulting in lab-on-a-chip platforms which can offer automated sample analysis in a portable format (typical dimensions of 10-100 mm) [25]. Several microfluidics-based electrochemical sensors have been developed. Swensen *et al*. developed a microfluidic biosensor system for continuous measurements of cocaine in blood [26]. The aptamer-based sensor chip is integrated with target-specific DNA aptamer and generate electrochemical signal within the microfluidic device.

Silicon and glass were the first materials used for fabricating microfluidic devices. Silicon was a common material for early development of microfluidic devices due to its compatibility with microfabrication technologies. The advantages of silicon-based devices include stable surface

properties, robust chemical/physical properties and well-known fabrication process. However, it usually requires expensive facilities for fabrication, therefore, alternative materials have received more attention [27]. Glass has gained considerable attention for microfluidic devices due to its chemical stability and optical transparency. It is not permeable and exhibits relatively low non-specific protein adsorption [28]. However, the fabrication of glass microfluidic devices requires high temperatures and/or large voltages for bonding glass layers together.

Polymers are another attractive class of materials for microfluidic devices because of their low cost, ease-of-fabrication, and disposability. Polydimethylsiloxane (PDMS) is a silicone material, which has been used for fabricating microfluidic devise for many years due to its excellent optical transparency, biocompatibility, and high compatibility with micromachining processes. The fabrication of PDMS microdevices is achieved via soft lithography which is a well-known fabrication process [29]. While PDMS offers many advantages for microfluidic devices, it is not well suited for some biological applications since its hydrophobic surface can absorb proteins and its fabrication is not amenable to high volume production.

Recently, researchers have been using plastics [25–27], including polystyrene (PS), polymethyl methacrylate (PMMA), polycarbonate (PC) polyethylene terephthalate (PET), polyvinylchloride (PVC) and cyclic olefin copolymer (COC), for microfluidic devices. Similar with PDMS, plastics are low cost, offer good biocompatibility and amenable to surface modification while being more mechanically robust, making them better suited for POC diagnostic devices. While plastics offer several advantages for microfluidic biosensors, more work is needed to develop simple fabrication techniques and robust surface modification strategies.

1.4 Electricity-free microfluidic pumping

1.4.1 Capillary flow

Microfluidic devices usually require external pumps to transport liquids inside microchannels. These pumping components are bulky, expensive and require external power. Alternatively, accurate displacement of microfluidic flows can be achieved by using on-chip micropumps [33]. While micropumps can provide precise, configurable flow rates, they increase the complexity and costs associated with microfluidic devices. The realization of microfluidic platforms that are simple, portable and inexpensive requires alternative means for fluid transport without externally-actuated components. Towards this end, passive pumping is a promising approach that doesn't require any moving components and can greatly simplify device fabrication and operation.

There are several methods for achieving passive pumping, such as thermally-driven, and capillary-driven flows. Among passive pumping methods, one of the most common is capillary pumping which employs surface tension forces to 'pull' liquids through capillaries and microchannels. This approach also offers simplicity in controlling the flow rate which mainly depends on the liquid viscosity, geometry, and surface properties of the channels [34]. In particular, the most important parameter for generating capillary flow is the surface hydrophilicity. Most polymers and plastics are hydrophobic, which hinders their use for capillary driven flows. While much work has focused on hydrophilic surface treatments on polymer surfaces, such as chemical grafting [35], oxygen plasma [36] and UV/Ozone (UVO) treatment [37], further work is needed to characterize hydrophilic surface treatments on plastics. However, capillary flow suffers from several disadvantages, such as difficulty in flow control and fluidic processing (e.g. mixing) [38].

1.4.2 Finger-powered pumping

For active pumping methods, electrical power sources are required to generate pressure head for fluid motion. Recently, an alternative approach for pumping liquids inside microchannels has been demonstrated based on finger actuation, which is reliable and portable, and eliminates the

need for electricity. Various mechanisms for finger-powered pumping have been demonstrated, such as screw based pumping [39], push-and-release action [40], and vacuum activation [41], as shown in Fig. 1-6. Based on this principle, the transport of liquids can be easily achieved via finger actuation. However, valves or diodes are typically required to accurately control the flow direction. Passive components, such as capillary valves [42], hydrophobic valves [43], or elastomer fluidic diodes [44], are favorable since they are simple and do not require external power sources. While functional, these passive components can suffer from poor reliability/reproducibility or require complicated microfabrication. Therefore, simple finger-powered pumping methods that do not require valves are desired.

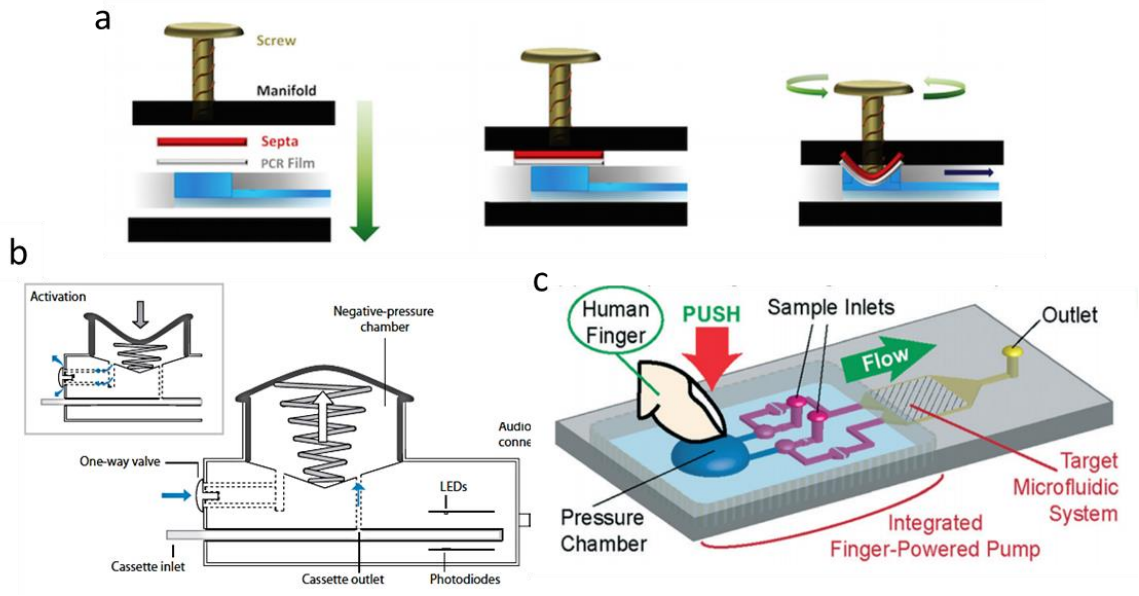

Figure 1-6. Schematic of three types of finger-powered pumping mechanisms: (a) screw-based pumping, image obtained from [39], (b) vacuum activation pumping, image obtained from [40], and (c) push and release pumping, image obtained from [41].

1.5 Mobile phone-based biosensors

Mobile phones have been increasingly utilized for biosensing due to their portability, accessibility and multi-functionality [15]. In particular, mobile phones offer a friendly user

interface, fast data processing and wireless communication. A useful component of modern mobile phones is a high-resolution camera, which has been employed for microscopic imaging. However, the camera quality varies on different models and brands of phones which can hinder the consistency of the results. Mobile phones can also be used as a portable power source [45] which can be used to manipulate liquids in microfluidic chips via electrokinetics. By connecting the phone with an electrical circuit (i.e. potentiostat), it is also possible to provide electrical signals required for performing diagnostic measurements. There are two possible electrical connection points on a mobile phone (audio jack and USB port) that can be used for data transmission. For wireless data transmission, mobile phones offer several routes, including Wi-Fi, Bluetooth or cellular networks (3G/4G), which enables rapid transmission of the results in real-time [46]. These capabilities can also enable for the data to be stored in the Cloud for storing patient medical records.

A smartphone-based fluorescence assay for quantifying albumin in urine was demonstrated by Coskun *et al.* [47]. As shown in Fig. 1-7a, this system employs a fluorescence detector affixed to the phone's camera, and a transparent tube which contains the urine sample. The fluorescent signal is processed through an App on the phone and generates the albumin concentration based on a calibration curve. A lower detection limit of 10 μg/mL is demonstrated with a linear range from 0 to 200 μg/mL. Although this device is fast and fairly simple, the optical components are bulky and complicated which limits its usefulness for POC testing. Alternatively, Stemple *et al.* demonstrated a POC device for protein quantification based on a microbead immunoagglutination assay combined with an optic-scatter system used to detect malaria biomarker [48]. Briefly, the presence of the target antigen within the channel causes the light to scatter, which is captured by the phone camera as shown in Fig. 1-7b. The concentration of analyte in the sample is determined based on the intensity of the scattered light. A detection limit of 1 pg/mL was achieved by using diluting blood, with a detection range from 1 pg/mL to 10 ng/mL. While these results are comparable to the sensitivity of previously demonstrated POC protein assays, further work is

needed to make this system compatible with raw biofluids, such as whole blood. The accuracy and reliability of optical sensing is greatly influenced by various factors, such as environmental lighting or sample composition. Therefore, to address this issue, researchers have developed mobile phone assays based on electric sensors. Lillehoj *et al.* developed a smartphone POC platform based on electrochemical detection for rapid protein quantification in human plasma shown in Fig. 1-7c [49]. In the presence of the target antigen, an electrochemical current is generated which is proportional to the analyte concentration in the sample. The lowest detection limit could be down to 16 ng/mL with a linear range from 0 to 1,024 ng/mL. Due to its portability, simplicity and capability to perform analytical measurements in raw clinical samples, this device offers great potential for POC testing. While promising, this assay requires several sample loading steps and uses an enzymatic substrate which offers limited room temperature stability. Towards a room temperature-stable assay, Laksanasopin *et al.* developed a mobile phone system to perform ELISA for quantifying HIV protein, as shown in Fig. 1-7d [41]. Dried reagents are stored within a microfluidic cartridge and become rehydrated by the diluted blood sample, which is transported by negative pressure generated from a mechanical vacuum spring. The presence of the target analyte causes a change in the optical density. Therefore, assessments of analytes over a dilution range of 1:128 is demonstrated in human blood samples. This device could remain stable at room temperature for up to one month and does not require any external equipment. However, this device only provides a qualitative result, and the optical signals can be affected by blood samples. Thus, there is a need for a shelf stable mobile phone biosensor which can generate quantitative and reliable measurements of protein biomarkers using whole blood samples.

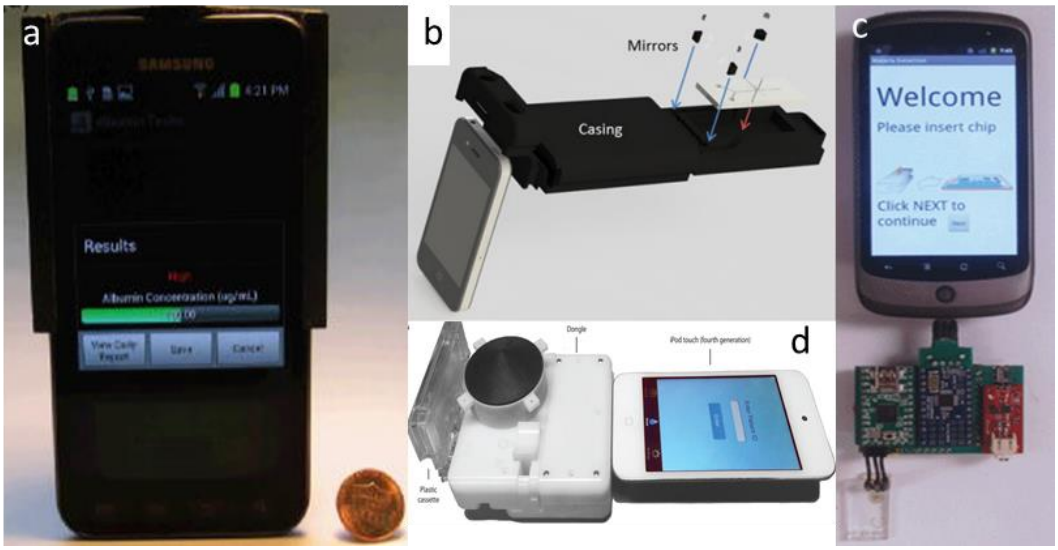

Figure 1-7. Examples of mobile phone-based systems for POC protein measurements. (a) Fluorescent measurement for quantifying albumin in urine. Image obtained from [47]. (b) Optic-scatter detection system for measuring protein amount. Image obtained from [48]. (c) Electrochemical measurement for evaluating malaria protein in human plasma. Image obtained from [49]. (d) Optical measurement on electrode for quantifying HIV protein. Image obtained from [41].

1.6 Objectives

Recent reports on mobile phone biosensors have shown that this technology is capable of rapid, high sensitivity analytical measurements on a portable platform for POC testing. However, existing devices cannot achieve high sensitivity in whole blood samples or exhibit a limited detection range. For example, most protein assays, including the gold standard ELISA, exhibit a detection range from 0.01 ng/mL – 0.1 ng/mL, making it challenging to detect protein markers at concentrations from ng/mL to μg/mL. In addition, many of these assays require multiple samples loading steps or exhibit poor stability at room temperature. Therefore, the goal of this work is to develop a finger-powered, room temperature-stable microfluidic electrochemical assay compatible with a mobile phone-based biosensing platform. This assay will employ an nonenzymatic electrochemical scheme which can measure protein biomarkers in whole blood samples from 1

μg/mL to 20 μg/mL, encompassing the clinical levels found in patients with *P. falciparum* infection [50]. The wide linear detection range of this assay will circumvent the need to run multiple measurements using diluted samples. To simplify testing, dried reagents will be stored on a disposable cartridge and reconstituted by phosphate buffer saline (PBS) which is pumped inside the microchannels via a unique finger-powered pumping mechanism. To achieve this goal, we have pursued the following objectives:

Objective 1: Investigate UVO treatment on thermoplastics

Objective 2: Explore plastic-based microfluidic device fabrication methods

Objective 3: Optimize electrochemical assay for detection of *Pf*HRP2

Objective 4: Develop a finger-powered microfluidic electrochemical assay

The knowledge and technologies generated from this dissertation represent a culmination of the experiences that have been obtained throughout my graduate career and will provide researchers new insights into the development of plastic microfluidic devices for POC testing.

Chapter 2. Investigation of UVO treatment on thermoplastics

2.1 Motivation

While plastics offer several advantages for POC microdevices, one of their main limitations is the lack of robust surface modification strategies, including ones that exhibit long-term stability. UVO treatment is a simple and effective method for making plastic surfaces more hydrophilic. Prior reports on the stability of UVO-treated plastics are limited to four weeks [37], which is not sufficient for applications requiring long-term storage. Therefore, we investigated UVO treatment on plastics to better understand its usefulness for microfluidic POC applications. In addition, we present for the first time findings on the long-term stability of UVO-treated plastics for up to 16 weeks and show that the storage condition has a significant impact on the surface stability. We focused our efforts on PMMA, PC, and COC because these are the most attractive plastics for biomedical applications due to their excellent optical transparency, biocompatibility and manufacturability [51]. Surface characterization of UVO-treated and untreated plastic samples was performed using x-ray photoelectron spectroscopy (XPS), atomic force microscopy (AFM) and contact angle measurements. UVO-treated plastics were also used for protein adsorption studies and capillary-driven flows experiments.

2.2 Methods and materials

2.2.1 UVO treatment and sample storage

PC and PMMA were purchased from McMaster-Carr (Elmhurst, IL) and COC was purchased from Zeon Chemicals (Louisville, KY). For XPS and contact angle measurements, COC and PMMA were cut into 1 cm × 2 cm pieces using a CO_2 laser cutter (Universal Laser Systems, Scottsdale, AZ) and PC was cut using a band saw. UVO treatment was performed using a UVO cleaner (Novascan Technologies, Ames, IA). For stability studies, samples were treated for 20, 40, 60 or 80 min at room temperature and stored in air, a dehumidified chamber (~20% relative humidity) or vacuum-sealed plastic bags (Weston vacuum sealer, Strongsville, OH).

2.2.2 Contact angle measurements

Static contact angle measurements were carried out using a VCA-2000 video contact angle analysis system (AST Products Inc., Billerica, MA). 0.5 µL droplets of distilled water were dispensed onto the samples using a pipette. Contact angle data was acquired at ambient conditions from three different samples at a minimum of three locations per sample. Each data point is plotted as the mean of eight separate measurements with outliers removed. New samples were used for each set of measurements.

2.2.3 XPS analysis and AFM measurements

XPS spectra were obtained using a Perkin Elmer Phi 5400 ESCA system (Physical Electronics, Chanhassen, MN) at pressures between 10^{-9} and 10^{-8} torr, pass energy of 29.35 eV, and a 45° take-off angle. Elemental composition was calculated from the relative intensities of the C1s and O1s peak areas obtained from the survey spectral after subtraction of a linear background. AFM scans were performed under tapping mode in air using a Cypher atomic force microscope (Asylum Research, Goleta, CA). Samples were imaged using a force constant of 0.2 N/m, scan rate of 2.44 Hz and scan size of 4 µm × 4 µm. Images were processed and analyzed for Root Mean Square (RMS) surface roughness using Igor Pro software (WaveMetrics, Lake Oswego, OR).

2.2.4 Protein adsorption measurements

Horseradish peroxidase (Px)-labeled anti-*Pf*HRP2 antibody was obtained from Immunology Consultants Laboratory, Inc (Lake Oswego, OR) and diluted to 10 µg/mL in phosphate buffered saline (PBS) (Fisher Scientific, Pittsburgh, PA). 3',3',5',5' tetramethylbenzidine substrate (TMB/H_2O_2) was obtained from Neogen (Lexington, KY), and deionized (DI) water (18.3 MΩ-cm) was generated using a Thermo Scientific Smart2Pure water purification system. PMMA, PC and COC were cut into 2 cm × 2 cm pieces and a 7-mm-diameter circular well was formed by attaching an adhesive-backed plastic stencil on the surface. Plastic pieces were exposed to UVO for 20, 40, 60 or 80 min followed by removal of the stencil. 80 µL of

1 μg/mL antibody solution was dispensed onto each piece and incubated for 30 min, rinsed using PBS and DI water, and dried under a stream of purified comprised N_2. This process resulted in the adsorption of enzyme-labelled antibodies on the surface. Pieces were then rinsed using PBS and DI water to remove unabsorbed proteins and dried using N_2. 80 μL of TMB/H_2O_2 was dispensed onto each sample and incubated for 1 min followed by absorbance measurements at 650 nm using a UV-visible spectrometer (Shimadzu, Kyoto, Japan).

2.3 Surface chemistry and morphology of UVO-treated plastics

We assessed the surface wettability of UVO-treated plastics by performing static contact angle measurements PMMA, COC, and PC treated for varying durations (Fig. 2-1). COC and PC exhibit substantial (60.6% ± 2.5% and 70.1% ± 3.2%, respectively) reductions in contact angle with 20 min of UVO exposure, whereas PMMA exhibits a moderate (31.0% ± 2.9%) reduction. However, with 40 min of UVO treatment, the contact angle of PMMA is reduced by 54.7% ± 0.7%, which is similar to COC and PC. With longer treatment times, the contact angles of COC and PMMA reach steady state at 60 min and 80 min for PC, which is indicative of the surface becoming saturated with oxygen-containing species. Among all three plastics, PC exhibits the lowest contact angle of 10.5º ± 0.6° after 80 min of UVO treatment, resulting in a superhydrophilic surface [52]. For PC and PMMA, there is an observable correlation between the treatment duration and surface wettability where longer times result in lower contact angles. In contrast, UVO treatment times > 20 min had a negligible impact on reducing the contact angle of COC, which is consistent with findings reported by Bhattacharyya *et al.* [53]. These results indicate that 20 min UVO treatment is sufficient in generating a hydrophilic surface on all three plastics, where a more substantial enhancement in wettability can be obtained for PMMA and PC with longer treatment durations.

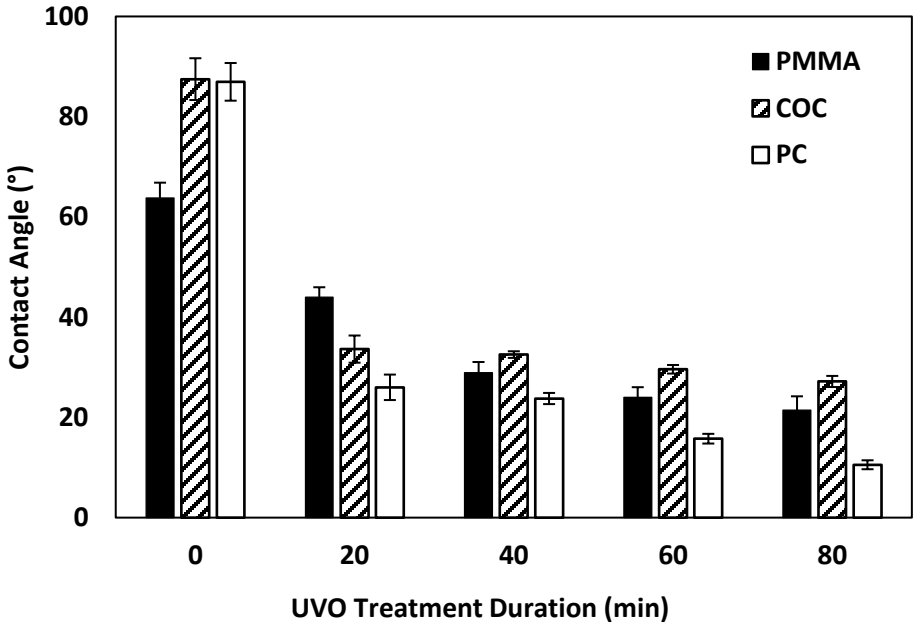

Figure 2-1. Contact angles of PMMA, COC and PC with varying durations of UVO treatment. Each bar represents the mean ± standard deviation (SD) of eight separate measurements.

UVO treatment of plastic results in the generation of an oxide layer on the surface rendering it more hydrophilic. Organic contaminants on the surface are removed via non-destructive atomic layer etching by 185 nm and 254 nm ultraviolet light. In the presence of oxygen, 185 nm light generates ozone while 254 nm light simultaneously excites organic molecules on the surface. The 254 nm light also generates free radicals on the surface that react with oxygen, generating more oxygen-containing species [54]. The generation of these oxygen-containing species increases the surface free energy and lowers the hydrophobicity. To study the change in the surface chemistry as a result of UVO treatment, XPS spectra of plastics exposed to UVO at varying durations were measured and used to calculate the oxygen/carbon (O/C) ratio on the surface. As shown in Table 2-1, all three UVO-treated plastics exhibit significantly higher O/C ratios compared with untreated plastics, which is due to the presence of additional oxygen-containing functional groups and indicative of the formation of an oxide layer. In addition, there is a positive correlation between the O/C ratio and treatment duration where longer UVO exposure results in a higher O/C ratio since

more oxygen-containing species are generated over time. The generation of oxygen species occurs rapidly within the first 20 min and gradually lessens with longer exposure times as the surface becomes saturated. After a certain point (~60 min), the oxygen content on the surface reaches a plateau as indicated by a negligible (< 5%) change in the O/C ratio compared with those of plastics with longer (80 min) UVO exposure.

Table 2-1. XPS analysis of the O/C ratio on the surface of UVO-treated and untreated plastics immediately following UVO exposure.

		PMMA	COC	PC
Untreated		0.34 ± 0.05	0.12 ± 0.02	0.19 ± 0.02
UVO-treated	**20 min**	0.48 ± 0.07	0.42 ± 0.10	0.47 ± 0.12
	40 min	0.54 ± 0.09	0.56 ± 0.06	0.59 ± 0.04
	60 min	0.53 ± 0.02	0.54 ± 0.07	0.55 ± 0.04
	80 min	0.56 ± 0.08	0.55 ± 0.05	0.56 ± 0.04

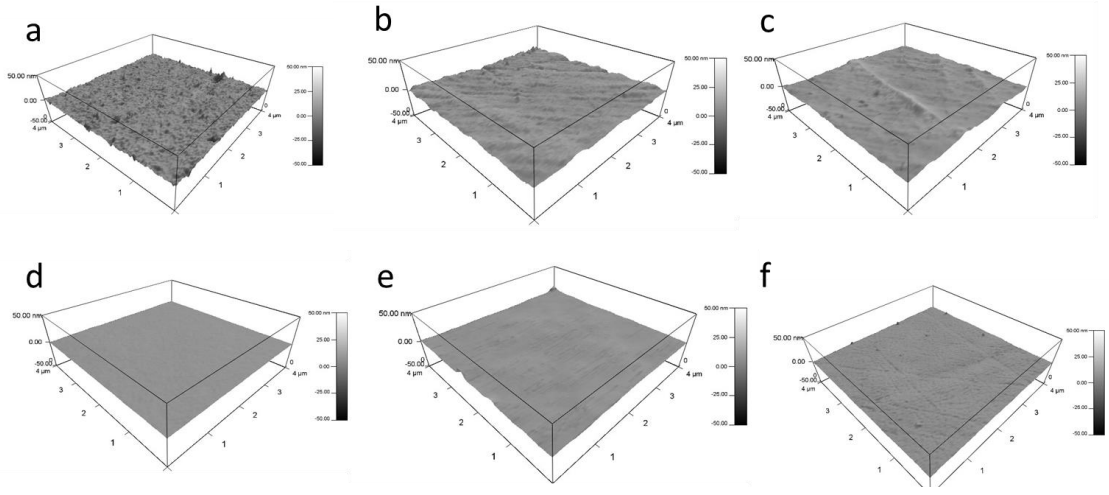

Figure 2-2. AFM tapping mode images of untreated PMMA (a), PC (b), and COC (c), and UVO-treated (80 min) PMMA (d), PC (e) and COC (f). The scan size and z-scale are 4 μm × 4 μm and 50 nm, respectively.

AFM scans and surface roughness measurements of UVO-treated and untreated samples were also obtained to briefly study the influence of UVO treatment on surface morphology as shown in Fig. 2-2. These results show that UVO-treated plastics exhibit smoother surface profiles and 2–7× smaller roughness values compared with untreated plastics as listed in Table 2-2. The smoother surfaces of UVO-treated plastics are due to the removal of organic contaminants via non-destructive etching from the UVO treatment process.

Table 2-2. Surface roughness values (nm) of UVO-treated and untreated plastic samples immediately after treatment and after 16 weeks of storage under different storage conditions.

		PMMA	COC	PC
Untreated, Non-stored		1.99 ± 1.34	2.21 ± 1.64	1.99 ± 1.57
UVO-treated (80 min)	**Non-stored**	0.26 ± 0.21	0.70 ± 0.53	0.83 ± 0.62
	Stored in air	2.76 ± 1.91	2.93 ± 2.36	2.26 ± 1.59
	Stored in vacuum	0.51 ± 0.35	1.10 ± 0.70	1.13 ± 0.62

2.4 Wetting stability of UVO-treated surface

To better understand the long-term stability of UVO-treated plastics, we performed contact angle measurements of plastics treated with UVO for 20 min (Fig. 2-3a), 40 min (Fig. 2-3b), 60 min (Fig. 2-3c) and 80 min (Fig. 2-3d) over the course of 16 weeks. For this study, plastics were stored under different conditions (air, dehumidified and vacuum) to determine its influence on hydrophobic recovery. Plastic samples stored in air, dehumidified and vacuum conditions are represented as black, grey and white markers, respectively, in Fig. 2-3. When stored in air, COC experiences substantial hydrophobic recovery within 4 weeks while PC and PMMA experience moderate hydrophobic recovery. In general, this trend is consistent for all four treatment times. When stored in air for > 4 weeks, the degree of hydrophobic recovery increases slightly for all three plastics, with the exception of COC treated for > 40 min, which steadily increases over time. More

importantly, these measurements show that the influence of the storage condition on the hydrophobic recovery is different for each type of plastic. For PMMA, the storage condition had a minimal impact on the surface stability for the duration of the study, particularly samples treated > 40 min. This trend is similar for PC, however after 12 weeks, there is a noticeable increase in the contact angle for samples stored in air. In contrast, the storage condition had a significant impact on the surface stability of COC where the hydrophobic recovery was dramatically reduced by storing samples under vacuum. These results indicate that the surface stability can be enhanced by longer UVO exposure and storing plastics in either a dehumidified or vacuum environment.

XPS spectra of UVO-treated (80 min) plastics stored for 16 weeks under different conditions were also obtained and used to calculate O/C ratios, which are presented in Table 2-3. Compared with freshly treated samples (Table 2-1), the O/C ratios for stored samples are lower, indicating a reduction in the concentration of oxygen-containing species on the surface due to hydrophobic recovery. UVO-treated plastics stored in air exhibit substantially smaller O/C ratios by 50% compared with those freshly treated. In contrast, UVO-treated plastics stored in dehumidified and vacuum conditions exhibit smaller (~10% and ~5%, respectively) reductions in the O/C ratio. These results are consistent with our long-term contact angle measurements (Fig. 2-3d) which show that hydrophobic recovery is generally more pronounced when stored in air and significantly inhibited when stored in dehumidified or vacuum conditions. The slightly higher O/C ratio exhibited by plastics stored in a dehumidified environment compared with in vacuum is likely due to the adsorption of water molecules on the UVO-treated surfaces, which reacts with the oxide layer thus reducing the oxygen content on the surface. Therefore, the oxide layer of UVO-treated plastics can be maintained by isolating them from moisture-rich environments thereby preserving the surface hydrophilicity.

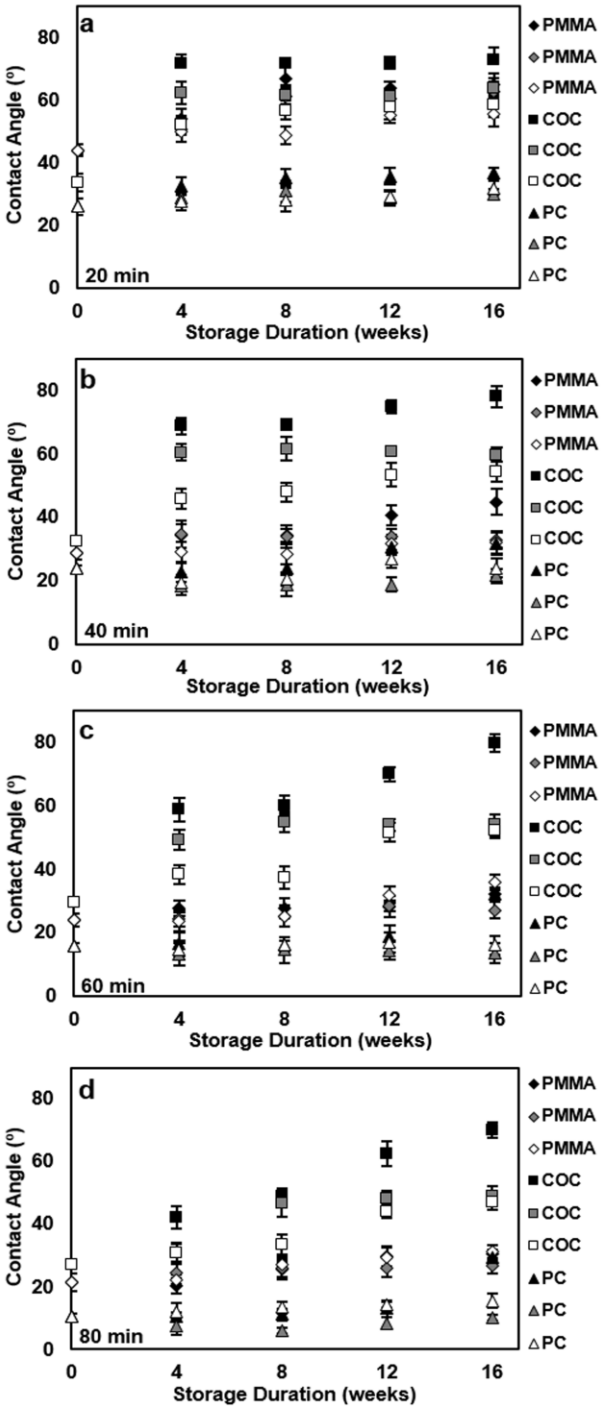

Figure 2-3. Long-term contact angle measurements of PMMA, COC and PC treated for 20 min (a), 40 min (b), 60 min (c) and 80 min (d) under various storage conditions. Black, grey and white markers correspond to storage in air, dehumidified and vacuum conditions, respectively. Each data point represents the mean ± SD of eight separate measurements.

Table 2-3. XPS analysis of the O/C ratio on the surface of UVO-treated and untreated plastics after 16 weeks under different storage conditions.

	PMMA	COC	PC
Air	0.27	0.31	0.34
Dehumidified	0.41	0.38	0.38
Vacuum	0.34	0.34	0.36

2.5 Effectiveness of UVO treatment for capillary flow and protein retention

To demonstrate the effectiveness of UVO-treated microchannels for capillary-driven flow, we performed flow experiments using PMMA microchannels with varying UVO treatment times. Experiments were also carried out using untreated PMMA microchannels for comparison. 40 µL of colored liquid was manually dispensed into the inlet of the microchannels using a pipette. As shown in Fig. 2-4, liquids quickly filled the 80 min-UVO-treated microchannel in < 4 sec while negligible flow was observed in the untreated microchannel.

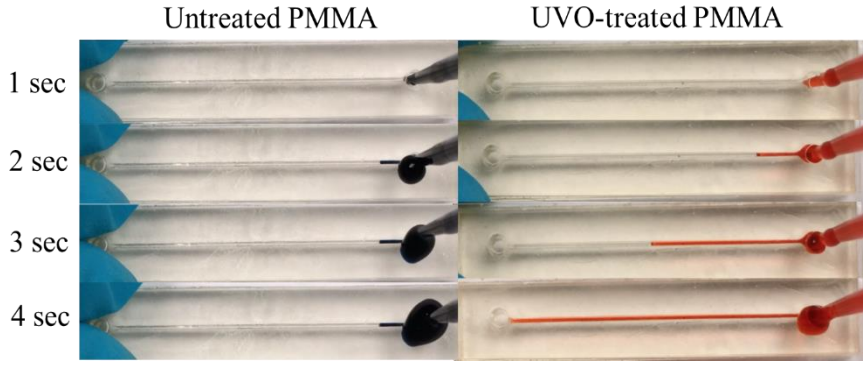

Figure 2-4. Capillary flow in untreated (left) and 80 min UVO-treated (right) PMMA microchannels. Colored dye is dispensed at the inlet of the chips using a pipette.

We also measured the volume flow rate for microchannels with various UVO treatment times (Fig. 2-5). From this plot, we observe that there is a clear correlation between the treatment

time and the flow rate due to the enhanced surface hydrophilicity generated from longer UVO exposure. This method can be applied to more complex microfluidic networks to develop capillary-driven systems that offer enhanced automation for more simplified operation. These results also suggest that UVO-treated microchannels can remain effective in pumping liquids via capillary flow after prolonged periods of storage when properly stored in dehumidified or vacuum conditions.

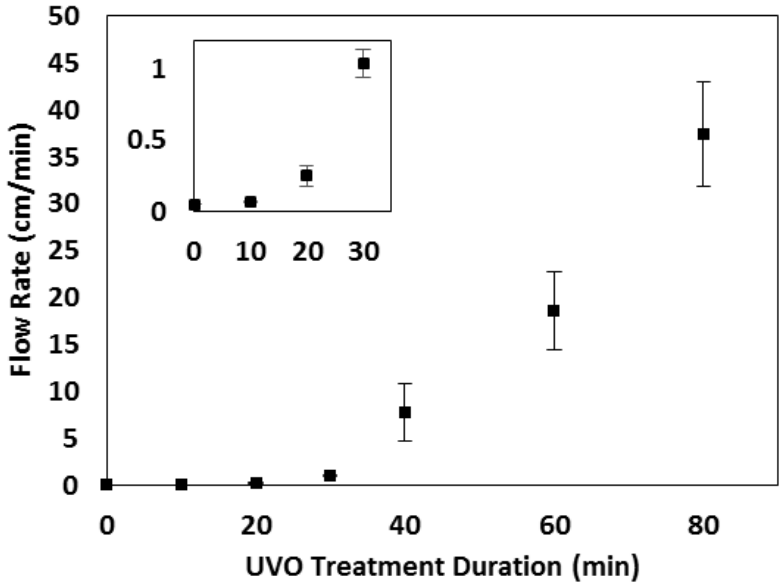

Figure 2-5. Capillary flow rate as a function of UVO treatment duration for PMMA microchannels. Inset shows magnified view of the data points at lower (< 40 min) UVO exposure times. Each data point represents the mean ± SD of three measurements.

Furthermore, the surface hydrophilicity plays an important role in protein adsorption [55]. To investigate the effect of UVO treatment on protein adsorption, we used a colorimetric detection scheme based on an enzymatic reaction between an Px-labeled antibody and a chromogenic substrate. Briefly, a droplet of solution containing Px-labeled antibody was incubated on a plastic sample for 30 min to allow the protein complex to adsorb onto the surface. The surface was rinsed using PBS and DI water to remove unabsorbed proteins followed by the application of the substrate (TMB/H_2O_2). The substrate reacts with the surface-adsorbed Px to generate a distinct blue color.

The absorbance of the droplet was measured at 650 nm using a UV- visible spectrometer, which correlates with the amount of protein adsorbed on the surface. Absorbance measurements were performed on PMMA, COC and PC exposed to UVO at varying durations.

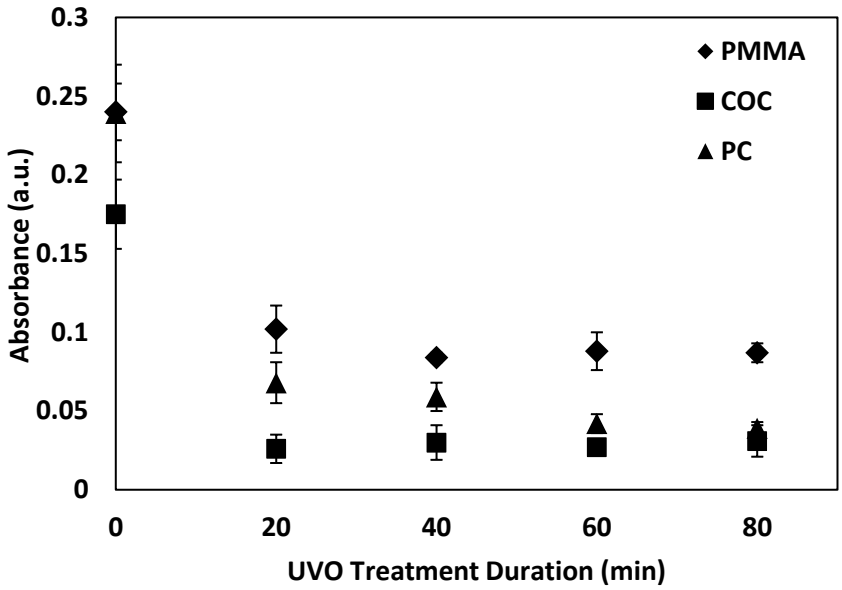

Figure 2-6. Absorbance values of TMB/H_2O_2 on plastics exposed to UVO at varying durations. Each data point represents the mean ± SD of three separate measurements obtained using new samples.

As shown in Fig. 2-6, longer UVO treatment durations resulted in lower absorbance values indicating that more hydrophilic surfaces inhibit the absorption of proteins. These findings are consistent with prior reports on the interactions between proteins and hydrophilic surfaces [56]. Of the three plastics studied, COC exhibited the lowest absorbance values for all treatment times indicating the least amount of protein absorption. In contrast, PMMA exhibited the highest absorbance values, even after 80 min of UVO treatment, indicating more protein adsorption which is likely due to its surface functional groups [57] and ionic strength [58]. These results indicate that 20 min of UVO treatment is sufficient in lowering the overall amount of protein adsorption on

plastic surfaces, where more substantial reductions can be obtained on PC with longer treatment times.

2.6 Summary

In this chapter, we have presented new findings on the surface chemistry, morphology and long-term (16 weeks) stability of UVO-treated plastics through XPS, AFM and contact angle measurements. Specifically, we showed that UVO-treated PMMA, COC and PC experience hydrophobic recovery within 4 weeks and the rate at which it occurs is dependent on the UVO treatment duration. Furthermore, we have discovered that the hydrophobic recovery of UVO-treated COC and PC can be inhibited by storing them in dehumidified or vacuum conditions. XPS measurements revealed that plastics stored in dehumidified and vacuum conditions exhibit higher oxygen content on the surface compared with plastics stored in air. UVO-treated plastics were also used for protein adsorption measurements, which showed that UVO treatment minimizes protein adsorption and this effect is correlated with the treatment duration. Lastly, we demonstrated capillary-driven flows in UVO-treated PMMA microchannels, which revealed that the flow rate could be tuned by adjusting the treatment duration.

Chapter 3. Plastic-based microfluidic device fabrication methods

3.1 Motivation

Various methods exist for fabricating plastic microdevices with each offering its own unique set of advantages and disadvantages [59]. Injection molding, one of the earliest and most common methods, requires expensive machinery and custom dies for each application, making it poorly suited for low volume production. Recent efforts have focused on alternative fabrication techniques, including micromilling [60,61], laser micromachining [62,63], stereolithography [64] and 3D printing [65], which require lower startup costs and can be used for low volume production. While each of these methods is promising, they are limited to certain types of materials or result in diminished material properties (e.g. surface finish, optical transparency).

An alternative method that does not suffer from these limitations is hot embossing [66]–[69]. Hot embossing is a process where a pattern is mechanically stamped into a softened plastic substrate using a rigid mold. For microfluidics applications, molds are typically fabricated from metal or silicon using CNC milling or microfabrication techniques, such as photolithography [70], electroplating [71] and deep reactive ion etching (DRIE) [72]. However, these methods are time consuming, expensive and require skilled technicians. Other than metal and silicon, alternative mold materials have been demonstrated on embossed templates, such as PDMS [73,74] and epoxy [75]–[77]. While these molds can be simpler to fabricate, they tend to suffer from poor reproducibility for multiple embossing cycles. To address these limitations, we explored the use of 3D printing to generate metal molds for hot embossing plastic microfluidic devices. Through optimization of the powder composition and processing parameters, we were able to generate stainless steel molds with superior material properties (density and surface finish) than previously reported 3D printed metal parts. Molds were used to fabricate PMMA replicas that exhibited good feature integrity and replication quality. Microchannels fabricated using these replicas exhibited leak-free operation and comparable flow performance as those fabricated from CNC milled molds.

We also investigated the fabrication of microfluidic devices using laser ablation and adhesive lamination bonding. Various processing parameters (laser power, laser speed, and scan rate) were characterized for researching laser effectiveness on substrate. Pressure sensitive adhesive film is utilized for providing a leak-free bonding for microfluidic assembly. With utilization of this fabrication process, a single microfluidic device can be created within a minute, with similar performance as devices generated from other fabrication methods.

3.2 Hot embossing using 3D printed molds with thermal bonding

3.2.1 Materials and methods

Microfluidic chips were designed using Siemens NX computer-aided design (CAD) software and printed using an X1-Lab 3D printer (ExOne, North Huntingdon, PA). This 3D metal printing system uses a Binder Jetting process (BJP) where a liquid polymer binder is selectively deposited on metallic powder in a layer-by-layer fashion using a roller. Surface roughness and replication fidelity measurements of printed molds and embossed replicas were carried out using an Olympus FluoView FV1000 confocal laser scanning microscope (CLSM). CLSM scans were collected using a 20× objective (NA = 0.75) scanning at 0.2 μm increments through 120 μm sample thicknesses at a resolution of 256 × 256 pixels. Surface profile images were generated from stacked CLSM scans and processed using MATLAB as previously described [78].

Plastic replicas were generated using 1.5 mm-thick PMMA sheets. Prior to molding, PMMA was rinsed with 2-propanol, deionized (DI) water and dried with compressed N_2 gas. Hot embossing was performed at 1 ton and 120 °C for 30 min using a Carver hot press (Wabash, IN). The temperature was lowered to 90 °C for demolding. The demolding temperature was carefully controlled to ensure adequate surface completion and replication quality. Plate alignment was checked before embossing to ensure uniform force distribution on the PMMA part and the embossing temperatures were closely monitored throughout the process via a thermocouple.

To generate enclosed microchannels, PMMA replicas were thermally bonded to 1.5 mm-thick PMMA pieces using a Carver hot press. Through-holes were generated using a CO_2 laser cutter (Universal Laser Systems, Scottsdale, AZ) to create inlets and outlets. Prior to bonding, PMMA surfaces were treated with UVO for 40 min using a Novascan Technologies UVO cleaner as we addressed in Chapter 2. In addition to making the surfaces more hydrophilic, UVO treatment enables bonding to occur at lower temperatures which minimizes the likelihood of channel collapsing or deformation [54]. PMMA pieces were sandwiched between Al foil to ensure uniform heat distribution and facilitate alignment in the press. The plates were preheated to 80 °C, followed by the application of 1 ton for 10 min. The plates were then cooled to room temperature and the bonded devices were released.

PMMA microchannels were cut normal to their length using a dicing saw (Buehler, Illinois) and cross-sectional images were captured using a JEOL 6620LV scanning electron microscope (SEM) at 10 kV with 50× magnification. For flow comparison studies, PMMA microchannels were also fabricated from stainless steel molds manufactured by CNC milling. The parameters for hot embossing and thermal bonding were kept consistent for both the 3D printed and CNC milled molds. Color dyes were dispensed into the inlets of the microchannels using a pipette and fluid flows were captured using a video camera, which were analyzed for flow rate measurements. Studies to compare pressure-driven flows in 3D printed and CNC milled molds were carried out by infusing PMMA microchannels with a solution of 10 μm diameter polystyrene beads ordered from Sigma (St. Louis, MO) in phosphate buffer solution (PBS) at a concentration of 10^5 particles per mL. Solutions were infused at a constant rate of 10 μL min^{-1} using a KD Scientific syringe pump (Holliston, MA). Flow rates were calculated by tracking the average bead velocity from video recordings.

3.2.2 Fabrication and characterization of 3D printed molds

A major limitation of current metal 3D printing technologies, including BJP, is the relatively poor surface finish of printed parts. For hot embossing, a smooth mold surface is required to facilitate the release of the plastic replica without damaging the embossed features. The surface finish of 3D printed parts can be improved by using very fine powders since thinner deposition layers can be achieved [79]. However, many 3D printing technologies, including BJP, are constraint to larger particles due to limitations with the rollers and build bed. To address these issues, we used a mixture of SS powder with two distinct powder sizes which allows the smaller particles to become nested in the interstitial spacing of the larger particles, as previously reported [80]. Also, we discovered that the final part density was significantly improved by incorporating BN powder. Based on prior experimental studies [80], adding 0.5% wt. BN to the SS powder mixture increased the final part density to 93% at a lower sintering temperature of 1250°C with negligible distortion.

Photographs and CLSM surface profiles of 3D printed molds with varying concentrations of BN are shown in Fig. 3-1. The colors in the surface profile images represent the surface height in the z-dimension. The pure stainless steel mold (Fig. 3-1a) exhibited a surface roughness of 6.61 μm ± 0.71 μm. In contrast, molds containing 0.25%, 0.5% and 0.75% BN exhibited improved surface finishes with surface roughness of 3.83 μm ± 0.53 μm, 3.65 μm ± 0.48 μm and 3.86 μm ± 0.86 μm respectively (Figs. 3-1b-d). These values are 2× lower than the pure stainless steel mold and up to 13× lower than previously reported 3D printed metal parts [81], and demonstrate that the addition of BN greatly improves the surface finish. The mold containing 0.25% BN exhibited smoother surface and roughness is decreased by 3 times. However, a higher concentration of BN powder did not seem to have a significance impact on further improving the surface roughness.

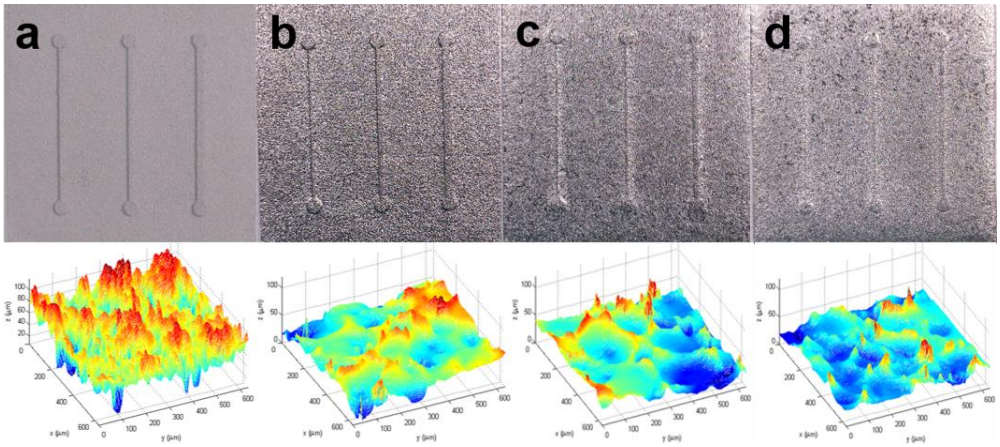

Figure 3-1. Photographs (upper) and surface profiles (lower) of 3D printed molds containing 0% (a), 0.25% (b), 0.5% (c) and 0.75% (d) wt. BN. The scan size and z-scale are 600 µm × 600 µm and 120 µm respectively.

3.2.3 Characterization of PMMA replicas

In this work, PMMA with a Tg of 103°C was used. The embossing parameter was fixed at 120°C and 1 ton for 30 min since this setting allows for good surface completion, as previously reported [82], while minimizing the overall processing time. For assessing mold reproducibility and physical stability, mold feature integrity, width and height were tracked after multiple cycles. There is only negligible shrinking (around 2%) in width and less than 1% happened in height after 20 times of embossing cycles.

To assess the functionality of 3D printed molds for hot embossing, we first studied the surface finish of the replicas. Replicas fabricated from the pure stainless steel mold exhibited a surface roughness of 8.23 µm ± 0.53 µm (Fig. 3-2a) while replicas fabricated from molds containing 0.25%, 0.50%, and 0.75% BN had substantially lower roughness values of 4.7 µm ± 0.84 µm, 4.20 µm ± 0.73 µm, and 4.12 µm ± 1.1 µm respectively (Figs. 3-2b-d).

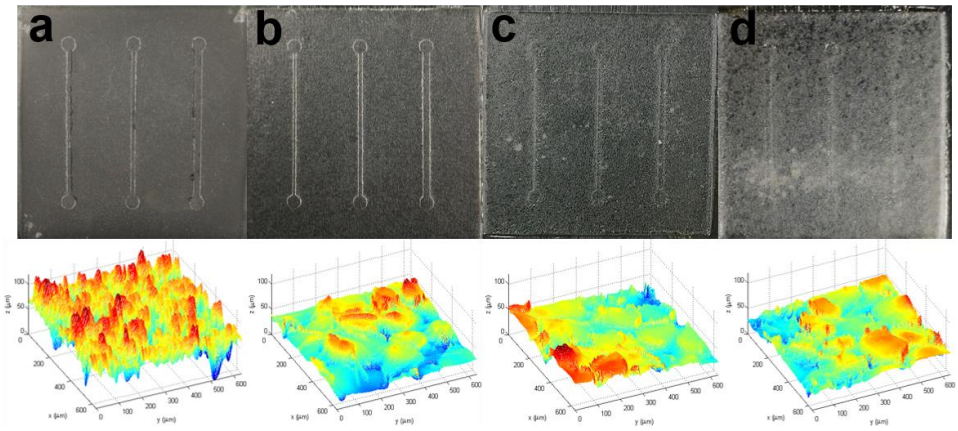

Figure 3-2. Photographs (upper) and surface profiles (lower) of PMMA replicas fabricated from 3D printed molds containing 0% (a), 0.25% (b), 0.5% (c) and 0.75% (d) wt. BN. The scan size and z-scale are 600 µm × 600 µm and 120 µm, respectively.

In addition to improving the surface finish, the inclusion of BN also helped to minimize the presence of defects at the edges of the embossed features that are typically generated during demolding (Fig. 3-3).

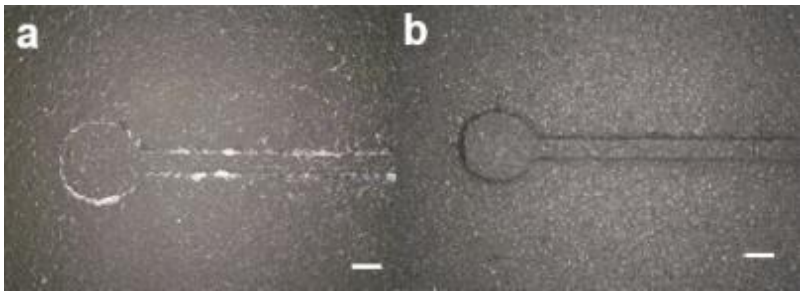

Figure 3-3. Close up images of embossed microfluidic features in PMMA fabricated using the pure stainless steel mold (a) and mold containing 0.25% wt. BN (b). Hot embossing was performed at 120°C and 1 ton for 30 min. Scale bars, 500 µm.

3.2.4 Thermal bonding and the influence of surface roughness

To generate fully enclosed microchannels using embossed components, replicas were bonded to flat pieces of PMMA. There are various methods for bonding plastics including solvent bonding [60,61], thermal bonding [84], and adhesive layer bonding [85]. Of these, thermal bonding

is a simple approach that can generate a strong and permanent bond. However, thermal bonding requires high temperatures and forces that can deform or damage plastic features. To mitigate this issue, a UVO surface treatment was applied to the PMMA surfaces prior to bonding. UVO breaks down the polymer chains and produces more oxygen-containing functional groups on plastic surfaces, which improves the overall bonding strength. Therefore, lower bonding temperatures can be used which helps to preserve the embossed features.

The surface roughness of the embossed part plays an important role in the bonding process. Therefore, we evaluated the bond quality of PMMA microchannels generated using replicas fabricated from 3D printed molds. The integrity of the embossed features after bonding was examined by observing the channel cross section using SEM (Fig. 3-4). Replicas generated using the pure stainless steel mold at 80°C resulted in incomplete bonding, as evident by the interfacial gap as shown in Fig. 3-4a. Fully enclosed microchannels could be generated at higher bonding temperatures (90°C); however, there is evidence of substantial microchannel deformation and shrinking (Figs. 3-4b). However, leak free bonding could be achieved at 80°C using the mold containing 0.25% wt. BN with minimal channel deformation (Fig. 3-4c). The difference in the surface roughness of the embossed parts is quite apparent in regards to bonding microfluidic devices where replicas fabricated from the mold containing 0.25% wt. BN could be bonded at lower temperatures with improved microchannel integrity compared with those fabricated from the pure stainless steel mold.

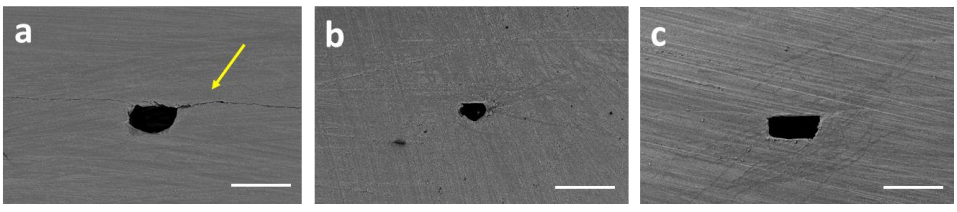

Figure 3-4. SEM images of cross sections of PMMA microchannels fabricated using the pure stainless steel mold and thermally bonded at 80°C (a), 90°C (b) and the mold containing 0.25% wt. BN at 80°C (c). The arrow indicates incomplete bonding. Scale bars, 500 µm.

3.2.5 Microfluidic device testing

To evaluate the functionality of microfluidic devices embossed using 3D printed metal molds, PMMA microchannels were fabricated and tested using colored dyes. Due to the UVO treatment prior to thermal bonding, the inner surfaces of the microchannels were made hydrophilic, and liquids could be driven inside the channels via capillary flow. We tested two different shaped microchannels: serpentine and zig-zag. As shown in Fig. 3-5a, colored dyes quickly filled both microchannels with no observable leaking. To further validate the capabilities of microdevices fabricated from 3D printed molds, straight microchannels were tested with pressure-driven flows and visually monitored over time. As shown in Fig. 3-5b, there are no signs of leaking after 1, 5, 10 and 20 min of continuous fluid flow and provides further evidence that these devices exhibit leak-free operation.

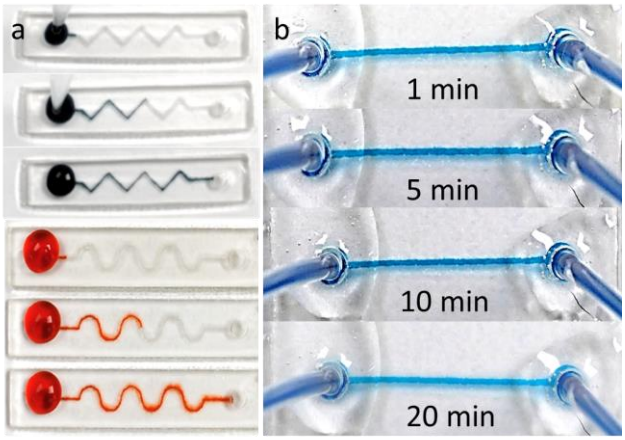

Figure 3-5. (a) Capillary flow in PMMA microchannels fabricated from 3D printed molds. Colored dye is dispensed at the inlet of the chips using a pipette. (b) Pressure-driven flow inside a PMMA microchannel fabricated from a 3D printed mold.

Experiments were also performed to compare the flow performance in straight microchannels fabricated from molds generated using 3D printing and CNC milling, as a benchmark. We first measured the capillary flow rate in three different channel widths (200 µm, 400 µm, and 800 µm) using DI water. As shown in Fig. 3-6, capillary flow rates for microchannels

fabricated from 3D printed molds were comparable to those fabricated from the CNC milled mold. We also used PMMA microchannels for pressure-driven flows and measured the average flow velocities. These results are consistent with the capillary flow rate measurements and shows that there is no significant difference between flow rates in microchannels fabricated from 3D printed molds and CNC milled molds. These results indicate that plastic microfluidic devices fabricated from 3D printed molds offer nearly identical flow performance as those fabricated from traditional manufacturing methods (i.e. CNC milling).

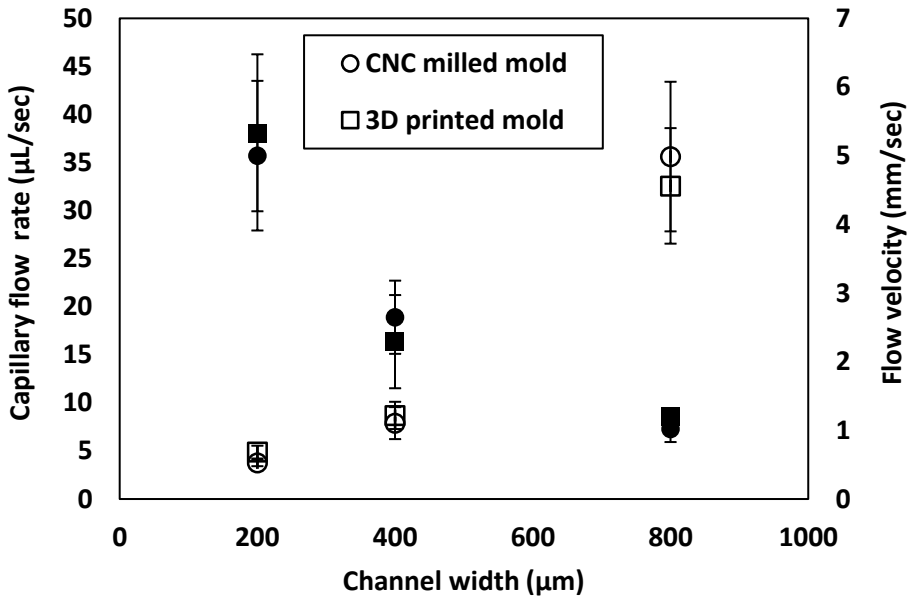

Figure 3-6. Comparison of flow performance in PMMA microchannels fabricated from 3D printed molds (squares) and CNC milled molds (circles). Capillary flow rates and pressure-driven flow rates are plotted as hollow and solid markers, respectively. Each data point represents the mean ± SD of three measurements for capillary flow experiments and five measurements for pressure-driven flow experiments.

While these preliminary results are promising, there are still several limitations with this approach. First, the lateral resolution is limited to ~200 µm. Second, the entire fabrication process is relatively time-consuming, taking 1 hr to make single plastic device. Therefore, we focused our

efforts on using laser cutting to fabricate microfluidic cartridges. The lateral resolution is limited to 100 μm, which is sufficient for this application while offering rapid fabrication.

3.3 Laser ablation with adhesive lamination bonding

While using 3D printed molds to fabricate microfluidic devices via hot embossing offers several unique advantages, it suffers from a few limitations. First, the lateral resolution is currently limited to ~200 μm. Second, the entire fabrication process is relatively time-consuming, taking 1 hr to make single plastic device. Therefore, we explored an alternative fabrication technique based on laser ablation and adhesive lamination bonding to fabricate microfluidic cartridges. Recently, laser cutting/etching has become a popular method for fabricating polymer microfluidic device due to its speed, simplicity and reproducibility. Machining microfluidic devices with a CO_2 laser cutter on PMMA has been reported for nucleic acid sensing [86]. While laser ablation has limitations with respect to microchannel lateral resolution (~100 μm) and relatively large (μm) surface roughness, it is still a promising technique for prototyping plastic microdevices. Laser ablation of plastics is typically carried out using a CO_2 laser system. Most polymers and plastics leave contamination residue on the surface and generate toxic gas after cutting. We have investigated the effectiveness of laser ablation on three plastics including PMMA, PC and COC. PC did not process well with the laser system as the material showed characteristic charring and yellowing at the processed areas. COC did not process favorably via laser ablation and resulted in heavy melt accumulation on the COC surface. Among all types of plastics, PMMA is the most suitable for laser ablation exhibiting fairly sharp cuts and minimal residue.

3.3.1 Materials and methods

Microfluidic devices were fabricated by etching microfluidic features in PMMA using a CO_2 laser cutter, followed by bonding using double-sided adhesive film (Adhesive Research, Glen Rock, PA). A schematic of our microfluidic cartridge fabrication process is shown in the Fig. 3-7. Adhesive film was applied on both sides of middle PMMA layer. Microfluidic features were

generated in the middle and top layers using CO_2 laser ablation, and then bonded together with an additional bottom layer.

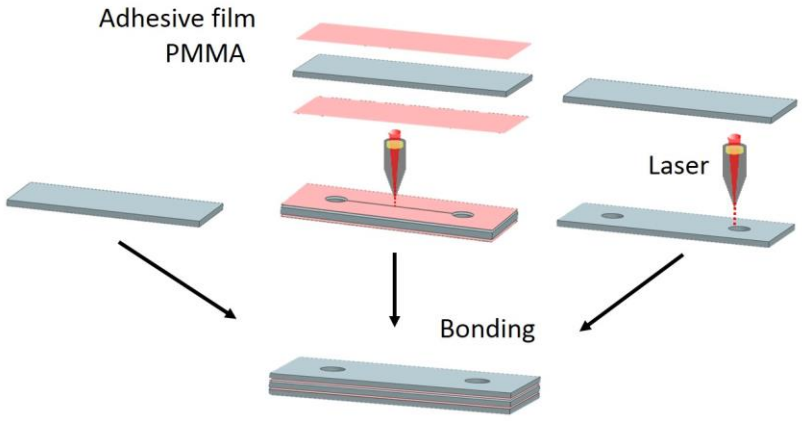

Figure 3-7. Microfluidic cartridge fabrication process based on CO_2 laser ablation and adhesive lamination bonding.

3.3.2 Optimization of operating settings for laser ablation of PMMA

The shape and size of the ablated features are largely influenced by the operating settings, such as beam focus, beam profile, exposure time and the power intensity. In order to better control the ablation process, we optimized various settings. For these studies, we fixed the exposure time and performed z-axis alignment to ensure that the beam was precisely focused on top of substrate. We first evaluated the size of ablated feature based on different CO_2 power settings (Table 3-1). The length of the feature was similar under different power setting, and the width slightly increased with higher power. However, the depth of the feature was significantly increased from 30W to 48W. At 48W power, the ablated feature was ~4× deeper than that at 30 W. These results indicate that it is possible to generate high aspect ratio features, with a minimal increase in the lateral dimensions) simply by increasing the power.

Table 3-1. Ablation feature size with respect to different power settings on PMMA. Each measurement is the average of five different samples.

Power	30W	36W	42W	48W
Length (µm)	710	734	737	737
Width (µm)	244	248	260	263
Depth (µm)	130	296	394	512

We also evaluated the feature size by fixing the exposure time (2 sec) and power (42 W) and modifying the number of passes of the laser. The results are shown in Table 3-2. For this study, the PMMA sample was ablated by performing multiple passes of the laser at the same position. With an increasing number of passes, the feature depth becomes deeper, with doubling with two passes and tripling with three passes. Interestingly, the width of the feature remained constant with a slight increase (~ 5%) in the feature length.

Table 3-2. Ablation feature size with respect to number of passes 42W on PMMA. Each measurement is the average of five different samples.

Power	42W	42W	42W
Number of Passes	1	2	3
Length (µm)	737	761	770
Width (µm)	260	266	265
Depth (µm)	394	694	966

The generation of fully enclosed microfluidic devices typically requires the bonding of multiple pieces. There are various of factors that need to be considered when bonding plastic pieces together, such as bonding strength, materials compatible and manufacturability [87]. Several methods are capable of generating leak-free bonding for polymer microfluidic device, including,

thermal bonding, solvent bonding, localized welding and lamination bonding. Lamination bonding (adhesive bonding) is an attractive technique since it is easy to perform, inexpensive and does not alter the device features or materials properties. For these reasons, we employed lamination bonding to fabricate our microfluidic cartridges.

3.4 Summary

In this chapter, we have demonstrated two different approaches for fabricating plastic microfluidic devices. In the first approach, replicas were generated via hot embossing using 3D printed molds and bonded together using thermal bonding. Using optimized powder composition and processing parameters, we were able to generate 3D printed molds with superior material properties and replication accuracy. Specifically, we show that a SS powder mixture incorporating 0.25% wt. BN powder dramatically improves the part density and surface finish. These enhancements enable for smoother surface finish of the plastic replicas and improved integrity of the embossed features. PMMA microchannels fabricated using this method exhibited leak-free operation with comparable flow performance as microchannels fabricated from CNC milled molds for both capillary and pressure-driven flows. In the second approach, microfluidic features were created on PMMA using laser ablation and bonded together using adhesive lamination bonding. Various operating parameters, including laser power and number of passes, were optimized enabling for more precise control of feature size, ultimately improving the utility of this technique for fabricating plastic microdevices.

Chapter 4. Electrochemical assay development for *Pf*HRP2 quantification

4.1 Motivation

Immunoassay have widely been used in clinical testing for more than thirty years because they are the most suitable and effective analytical method [88]. There are several commercial assays with high sensitivity and accuracy, such as ELISA (Fig. 4-1). However, these assays usually suffer from complicated sample preparation, and poor stability. For POC test development, it is desired to develop a room-temperature assay for high sensitivity measurements of protein biomarkers in whole blood samples. To achieve this, we investigated two different detection schemes and studied various assay parameters, including the immobilization of bioreceptors, concentration of the antibodies/reagents, optimization of substrate and applied potential.

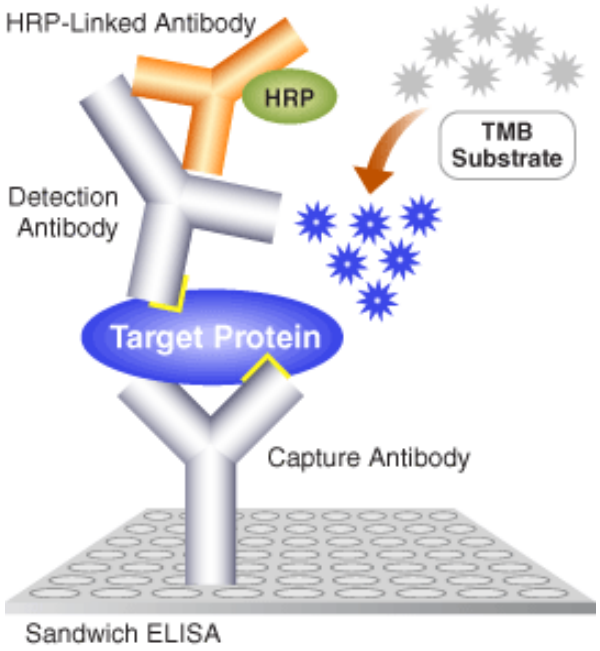

Figure 4-1. Schematic of sandwich ELISA. Target protein is encapsulated between two layers antibodies, followed by TMB reacting with Px and generate signal. The signal should be proportional to the concentration of target protein. Image obtained from [88].

4.2 Horseradish peroxidase-based electrochemical assay

A schematic of the *Pf*HRP2 electrochemical assay is shown in Fig. 4-2. Anti-*Pf*HRP2 IgM is immobilized on the working electrode (Fig. 4-2a). In the absence of *Pf*HRP2 antigen, the Px-conjugated detection antibody is washed away during the rinsing step and a negligible signal is generated. However, when *Pf*HRP2 is present in the sample, it binds to sensor surface (Fig. 4-2b) allowing surface immobilization of the Px-conjugated detection antibody (Fig. 4-2c). Upon application of a bias potential, an electrochemical reaction takes place between Px and substrate (i.e. TMB), resulting in a high signal (Fig. 4-2d). Based on this scheme, the concentration of *Pf*HRP2 in the sample is proportional to the current generated during the electrochemical reaction. In this chapter, we are introducing various bioassay development methods and evaluate their performance.

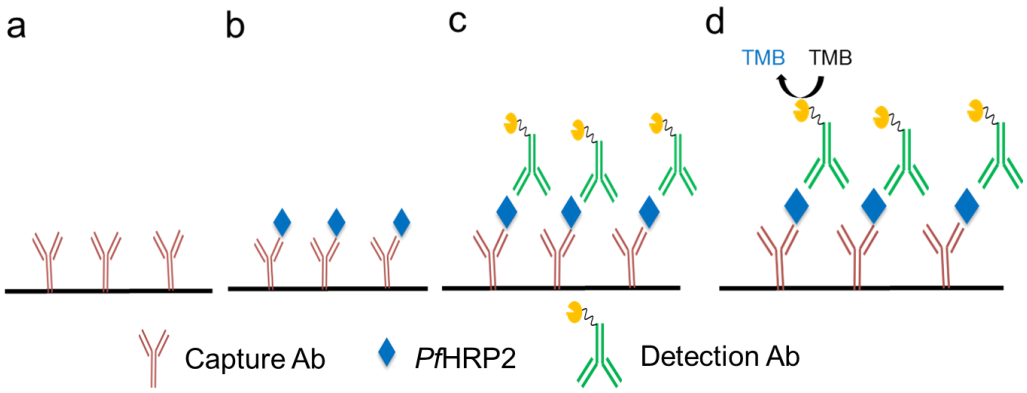

Figure 4-2. Schematic of an enzymatic PfHRP2 electrochemical assay. (a) The sensor is immobilized with capture antibody on surface. (b) If present, sample binds to the capture antibody. (c) Detection antibody is immobilized on the sensor via binding to sample, forming a sandwich structure. (d) Peroxidase reacts with substrate generating a current that is proportional to the PfHRP2 concentration.

4.2.1 Materials and methods

Gold sensor chips were purchased from GeneFluidics (Irwindale, CA). Amperometric measurements were performed using a multichannel electrochemical workstation obtained from

GeneFluidics. Before electrochemical testing, gold sensors were carefully examined for defects, such as debris and scratches. Anti-*Pf*HRP2 mouse IgM (capture antibody) and Px-conjugated anti-*Pf*HRP2 mouse IgG (detection antibody) were obtained from Immunology Consultants Laboratory (Portland, OR). Recombinant *Pf*HRP2 was purchased from CTK Biotech (San Diego, CA). Samples were prepared by serially diluting *Pf*HRP2 antigen in PBS, human plasma or whole blood (Bioreclamation Inc., Westbury, NY). Bovine serum albumin (BSA), phosphate buffer solution (PBS), PBS-casein, hydrogen peroxide (H_2O_2), 4-Aminophenol (4AP), dimethyl sulfoxide (DMSO), Traut's Reagent (2-iminothiolane) and ethylenediaminetetraacetic acid (EDTA) were purchased from Sigma. DI water was generated using a Thermo Scientific Smart2Pure water purification system (Tustin, CA).

For analyte measurements, 40 µL of capture antibody was immobilized onto the sensing region using a pipette, and incubated on the sensor for 1 hr followed by rinsing with PBS and drying with N_2 gas. The antibody-immobilized sensor was incubated with 40 µL of PBS-casein for 30 min at 25ºC to block the surface from nonspecific binding. The sensor was then rinsed with PBS, dried using N_2 gas, followed by adding 40 µL sample and 40 µL detection antibody and substrate sequentially. Next, the application of a −200 mV bias potential was applied on the working electrode after 1 min. All electrochemical measurements were performed at room temperature under ambient conditions using new sensors.

4.2.2 Antibody immobilization optimization

Protein immobilization is an important step for preparing the biosensor surface since the amount of immobilized protein affects the sensitivity and detection range. There are several immobilization methods to attach proteins onto a sensor surface, which can be grouped into three main categories: physical adsorption, covalent bonding and bioaffinity interactions [62,63] as shown in Fig. 4-3. Since random orientation and structural deformation leads to a loss of protein activity, a suitable immobilization is required to retain biological activity. We have assessed

different immobilization methods to determine the one that offers the optimal detection performance.

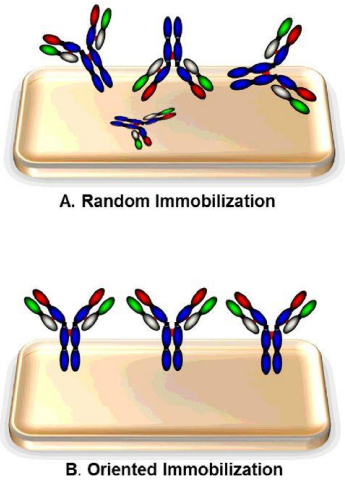

Type of Immobilization	*Type of Interaction*	*Functional group*	*Orientation*
Adsorption	Electrostatic; hydrophobic interactions;	Various	Random
Entrapment	Entrapment		Random
Covalent coupling	Amine coupling	$-NH_2$	Random
	Thiol Coupling	-SH	Specific
	Coupling via glycan moiety	-CHO	Specific
Affinity	Intermediate protein (A/G); Avidin-biotin	Fc region	Specific

Figure 4-3. Different methods for performing immobilization and functional groups used for orienting antibodies on substrate [62]

4.2.2.1 Physical absorption

Proteins can be absorbed on surfaces via intermolecular forces, mainly through electrostatic attraction, and hydrophobic and polar interactions. As a result, proteins are likely to be heterogeneous and randomly oriented on the electrode. The main drawbacks of this method are weak attachment resulting from the random orientation which may result in proteins being washed away during rinsing.

The preliminary results shown in Fig. 4-4 were generated using sensors employing physical adsorption for the immobilization of capture antibodies. Briefly, we incubated capture antibodies on the sensor for 2 hr, sequentially added antigen (*Pf*HRP2) serial diluted in PBS from 16 ng/mL to 1,024 ng/mL, added detection antibody conjugated with Px, followed by the addition of TMB/H_2O_2 substrate for electrochemical reaction (TMB was first selected as our substrate and we will further discuss it in the following sections). The resulting electrochemical signal was acquired

by applying a -200 mV bias potential. As shown in Fig. 4-4, the analyte concentration is proportional to the current up to 256 ng/mL.

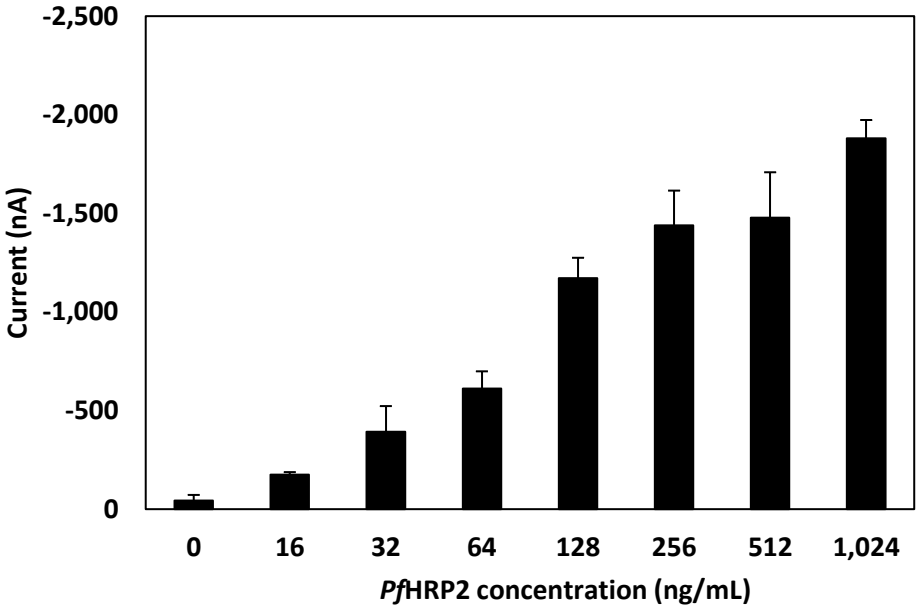

Figure 4-4. Amperometric signals of PfHRP2 diluted in PBS using sensors prepared by physical absorption immobilization technique. Each bar represents the mean ± SD of four measurements.

4.2.2.2 Amine group covalent binding

For the physical absorption immobilization method, it is difficult to control the antibody orientation, resulting in randomly-oriented antibodies on the surface. In a sandwich ELISA scheme, the antigen only binds to a single epitope on the capture antibody. Therefore, if the epitope is not oriented upward, the probability for capturing the target antigen is lowered. In addition, the forces acting between the antibody and the substrate mainly depend on low-energy interactions, which results in weak antibody binding strength to the substrate. Multiple sample-pipetting and residue-washing steps can destabilize antibody attachment, so this approach is not practical for ELISA-based assays.

Therefore, an alternative covalent binding method was studied. Covalent attachment immobilization is a frequently used method in microfluidic assays [89]. The activated surface reacts

with amino acid residues on the protein to form a stable linkage. In this approach, antibodies are covalently bound to the gold surface, as shown in Fig. 4-5. The chemical bonds are usually generated by reagent treatment, such as chemical self-assembly and plasma treatment [91]. Carboxyl, amine and thiol group are typical chemical bonds used for antibody attachment. Carboxyl-based covalent bonding on gold has been used for many years for the immobilization of proteins [92]. For carboxyl self-assembly on gold, 11-Mercaptoundecanoic acid (11-MUA) is applied to the surface for 2 hr at 10 mM (these conditions are selected based on optimization). For activating the carboxyl groups, [1-ethyl-3-(3-dimethylaminopropyl) carbodiimide] (EDC) in combination with N-hydroxysuccinimide (NHS) at a 2:1 ratio was applied on to gold substrate and incubated for 1 hr. Capture antibody was then added, which linked with the gold electrode via amine chemical bonding. The spiked sample and substrate were subsequently added to the surface to generate an electrochemical reaction. Electrochemical measurements were taken with a potential bias at -200 mV, and the results are shown in Fig. 4-6.

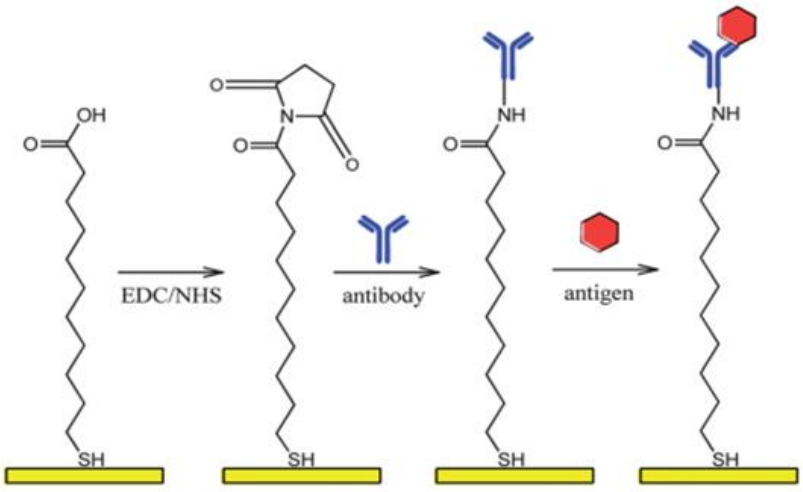

Figure 4-5. Schematic of 11-MUA self-assembly on gold electrode and subsequent immobilization of capture antibody and antigen. Image obtained from [93].

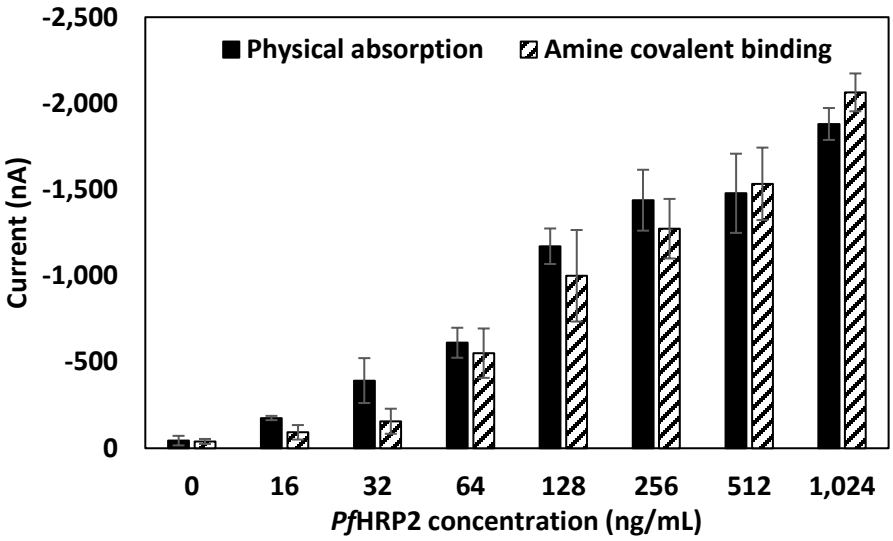

Figure 4-6. Amperometric signals of PfHRP2 diluted in PBS via amine- group covalent binding immobilization technique. Each bar represents the mean ± SD of four measurements.

Covalent binding exhibited stronger bonding compared to physical absorption and prevented enzyme release into the reaction environment. Absorption binding resulted from weak non-specific forces, such as van der Waals, hydrophobic attraction, and hydrogen bonds which are weaker than chemical covalent bond. In addition, covalent binding method increases enzyme activity when couple with substrate supports [94]. Even though there are two more steps for primary antibody immobilization, the amine covalent binding method is considered to facilitate long-term storage and reusability of immunosensors [95]. Based on our preliminary results shown in Fig. 4-6, the amine binding method showed similar signals from 0 to 1,024 ng/mL as the physical adsorption method. However, amine groups generated higher currents at higher *Pf*HRP2 concentrations above 512 ng/mL. These results indicate that there is more capture antibody immobilized on the sensor and has the ability to capture more analyte in the sample, therefore generating a higher signal.

Another parameter that we investigated was the incubation time. For traditional ELISA, it requires 6 hr to perform a single measurement. It is desirable to develop a faster diagnostic test which can provide prompt results to patient and medical technicians. In order to achieve this goal, various techniques have been explored to reduce the incubation times, including the use of nanomaterials [96], magnetic stirring [97] and electrophoresis [98]. Alternatively, the incubation time of reagent preparation can be dramatically reduced via electrokinetic-assisted protein transport [68,69]. Specifically, applying a bias potential on non-uniform electrodes generates electrokinetics forces which transports biomolecules closer to the surface, resulting in faster protein recognition and binding. We employed this technique for our assay and optimized the electric field parameters, resulting in an incubation time of 5 min which is 12× faster than ELISA. *Pf*HRP2 recognition was achieved by applying 400 mV for 3 min, and detection antibody binding step was assisted by a 200 mV for 1.5 min. The performance of this technique was evaluated by measuring buffer samples spiked with *Pf*HRP2 from 0 ng/mL to 1,024 ng/mL compared with an incubation-based approach.

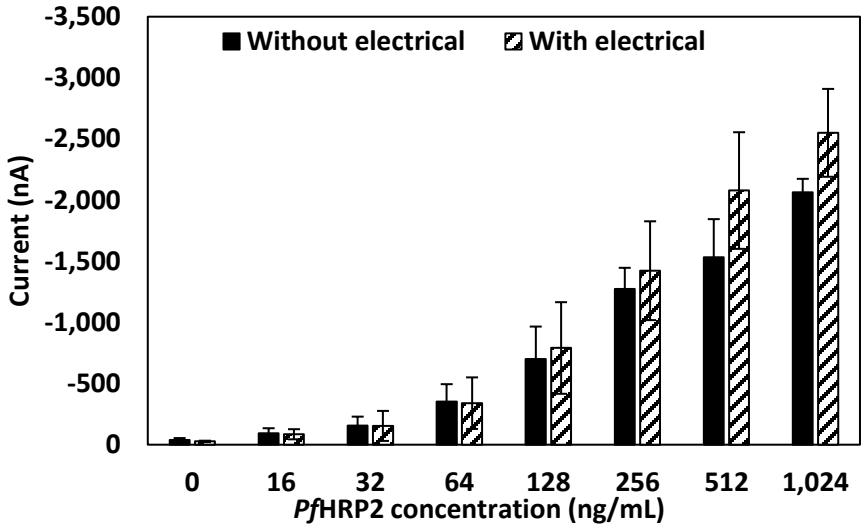

Figure 4-7. Amperometric signals of PfHRP2 diluted in PBS obtained from electric field-assisted sensors (solid) and sensors undergoing incubation. Each bar represents the mean ± SD of two measurements.

As shown in Fig. 4-7, the signals for electrical field-assisted sensors are (1.3×) higher than the signals obtained using a standard incubation method. Based on these results, electrical field-driven protein recognition/binding not only minimizes the testing time but also results in improved signal-to-background ratio (SBR) and less incubation time.

Measurements of *Pf*HRP2 at higher concentrations were performed in PBS, plasma and whole blood to evaluate the detection range of this assay. As shown in Fig. 4-8, measurements from only PBS matrix exhibited a linear relationship. In general, signals in whole blood are slightly higher than in plasma samples due to matrix effect. However, human plasma samples exhibited better SBR than whole blood samples, therefore detection limit of whole blood is constrained in this bioassay. Human blood contains lipids which can bind to the antibody-coated sensor and interfere with protein recognition and binding [101]. In addition, red blood cells contain hemoglobin which exhibits pseudo peroxidase activity [102], which can interfere with the electrochemical reaction if the immune complex is not well washed. Furthermore, the detection signals in both blood and plasma were substantial lower compared with PBS and further work will focus on improving the assay performing in biofluids.

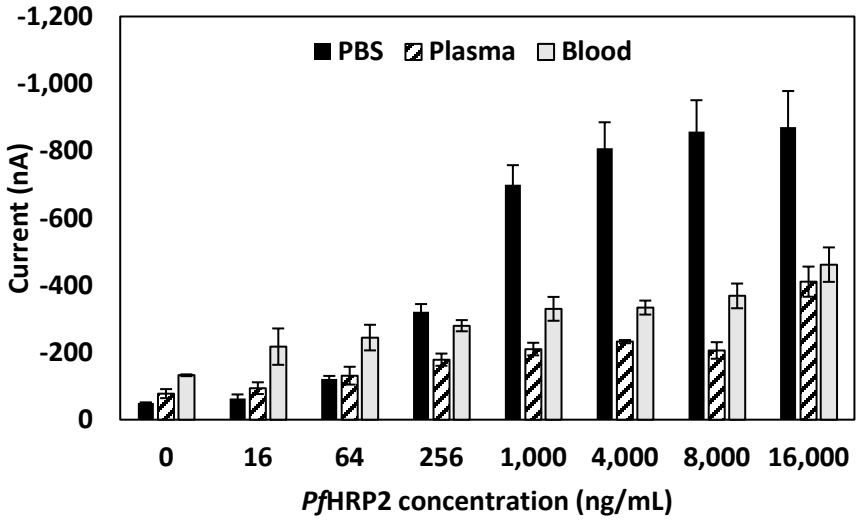

Figure 4-8. Amperometric signals of PfHRP2 diluted in PBS (black), human plasma (striped) and human blood (gray). Each bar represents the mean ± SD of four measurements.

4.2.2.3 Thiol group covalent binding immobilization method

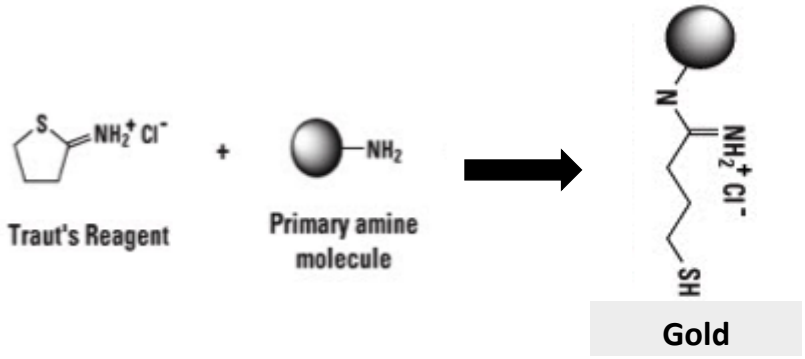

Figure 4-9. Schematic of the working mechanism for thiol group immobilization method. Image modified from [103].

We investigated another approach for antibody immobilization based on thiol-group interaction to simplify the immobilization protocol. Using this approach, the 11-MUA incubation and EDC/NHS activation steps can be eliminated from the protocol. The capture antibody is processed by Traut's Reagent forming thiol chemical bonds, as shown in Fig. 4-9. Thiolated antibody solution was prepared by combining 990 µL of PBS (Ethylenediaminetetraacetic acid (EDTA)) containing of 100 µg/mL anti-*Pf*HRP2 IgM with 10 µL of dimethyl sulfoxide (DMSO) (1 mg/mL) in Traut's Reagent, incubating at 25ºC, and centrifugation to remove residual DMSO. Precipitated antibody was reconstitute using PBS and incubated on the gold sensor for 1 hr. This immobilization process can be completed in 2 hr with thiol chemical bonds attached to surface. The antibody-immobilized sensor was incubated with PBS-casein mixed with 30% of stabilizer to block the surface from nonspecific binding.

The minimized processing steps for primary antibody immobilization improved the simplicity and convenience of the sensor preparation protocol. Thus, we spiked *Pf*HRP2 in human blood from 0 ng/mL to 16,000 ng/mL and performed the measurement for comparing the result with amine group immobilization method. As shown in Fig. 4-10, the results indicated that the thiol

immobilization method exhibited higher signals and offered a better SBR difference. Therefore, we selected thiol immobilization method as our bioassay development method.

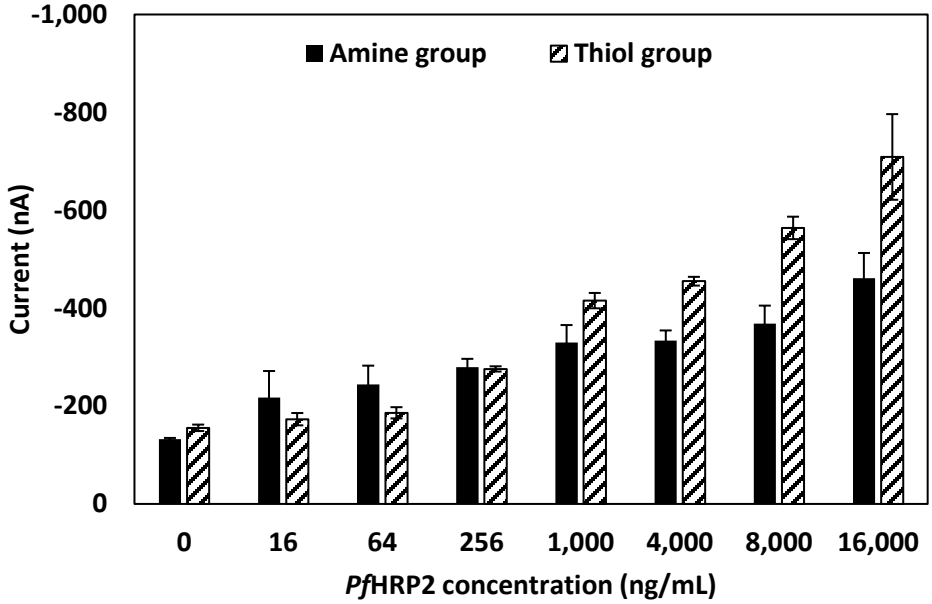

Figure 4-10. Amperometric sensing of PfHRP2 diluted in human blood based on carboxyl group antibody immobilization (solid) and thiol-group antibody immobilization (striped). Each bar represents the mean ± SD of two measurements.

4.2.3 Substrate optimization

In our enzyme-based electrochemical scheme, Px was selected as our reporter conjugated to the detection antibody. TMB is the most common chromogen used for Px and evaluated as the electrochemical substrate [104]. We initially selected TMB as the substrate for Px in ELISA, which usually develops a soluble blue reaction product that may be read at 370 or 655 nm via spectrometer. Moreover, measurement of Px activity can be achieved by using amperometric method [25,71]. The Px-TMB working mechanism is shown in Fig. 4-11, TMB reacts with Px and generates a redox cycling with gold electrode [97]. The value of the signal is proportional to the amount of Px on detection antibody. The preliminary results presented above were all obtained using TMB.

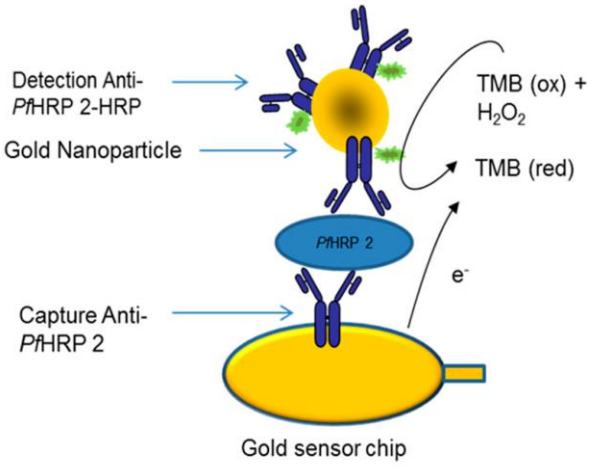

Figure 4-11. Schematic of the detection scheme for PfHRP2 detection based on a redox reaction between an enzyme reporter and TMB+H_2O_2. Image obtained from [97].

For ELISA and many colorimetric immunoassays, TMB is used as the substrate. However, TMB is a light and temperature sensitive chemical, and easily degrades without proper storage. The need for refrigeration and light-protected storage hampers its practicality for POC applications. Also, the detection signal at higher *Pf*HRP2 concentrations is low, therefore, we investigated ways to increase the amperometric signals. There are several ways for enhancing the detection signal in electrochemical assays, such as utilizing nanomaterials for increasing the reaction area and speed, optimizing the immobilization method for capturing more target on the surface, or selecting a mediator for enhancing redox reaction. All these methods are useful, however, considering the simplicity and stability approach, we focused our efforts on substrate optimization.

4AP is an organic compound which can be used for electrochemical reactions and exhibits higher sensitivity due to its distinct redox reaction. In each electrochemical reaction, there are two electrons transfer involved for 4AP redox reaction, which is 2× as much as the TMB reaction [105]. Thus, 4AP will promote electron transportation speed, and generate more current than TMB. Furthermore, TMB as a substrate for Px is more sensitive than other chromogens, which can be degraded by sunlight or fluorescent lights, resulting in poor signal intensity [106], and may produce

false positive signal affecting the accuracy of measurements. Additionally, 4AP can be stored as a solid form making it possible for storage at room temperature without decay; it's a great advantage for applying 4AP as our device substrate. Future work will focus on characterizing the room temperature stability of 4AP.

As shown in Fig. 4-12, there is a linear relation up to 20 µg/mL using 4AP compared with TMB which remains flat from 1 µg/mL to 20 µg/mL. Based on these preliminary results, the use of 4AP as substrate provides us a wider detection range and higher SBRs. These results are consistent with previous reports on achieving lower background current level in Px via catechol/o-benzoquinone redox couple [107].

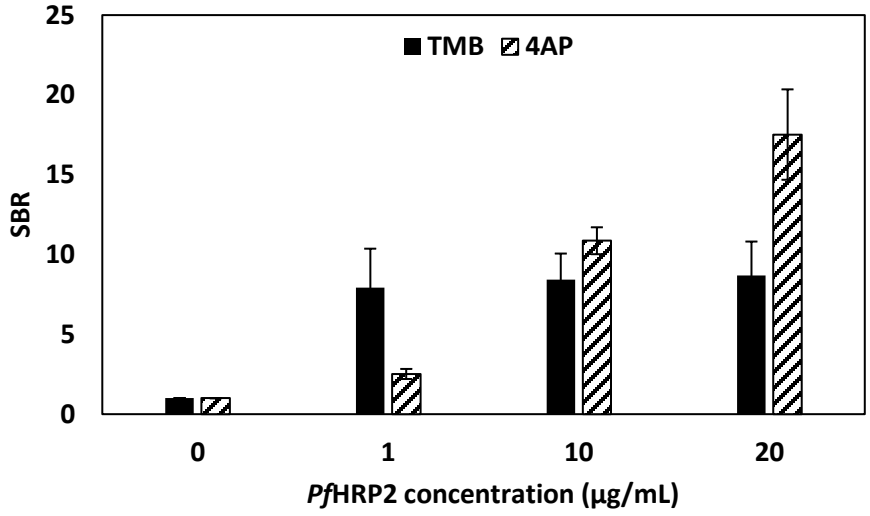

Figure 4-12. Amperometric results were obtained from spiking sample in PBS. Signal-to-background ratio was used for comparing different substrate of 4AP and TMB. There is negligible signal difference for TMB for concentration above 1 µg/mL. Each bar represents the mean ± SD of two measurements.

For amperometric measurements, the value of current is evaluated based on a constant applied potential. Selection of optimal potential for the enzymatic reaction (Px-TMB) is significant. Cyclic voltammetry (CV) was conducted from +200 mv to -600 mV to find the optimal signal for

SBR. The potential range for the reduction reaction occurred between -100 mV to -300 mV. We tested each potential with 50 mV increments, and -200 mV and -150 mV generated the highest SBR. Therefore, *Pf*HRP2 sample was spiked in human plasma samples at varying concentrations from 0.1 µ/mL to 50 µg/mL, and the two bias potentials were applied to evaluate their signal generation. As shown in Fig. 4-13, -150 mV resulted in improved linearity up to 20 µg/mL. Therefore, we selected -150 mV as the bias potential for electrochemical measurements.

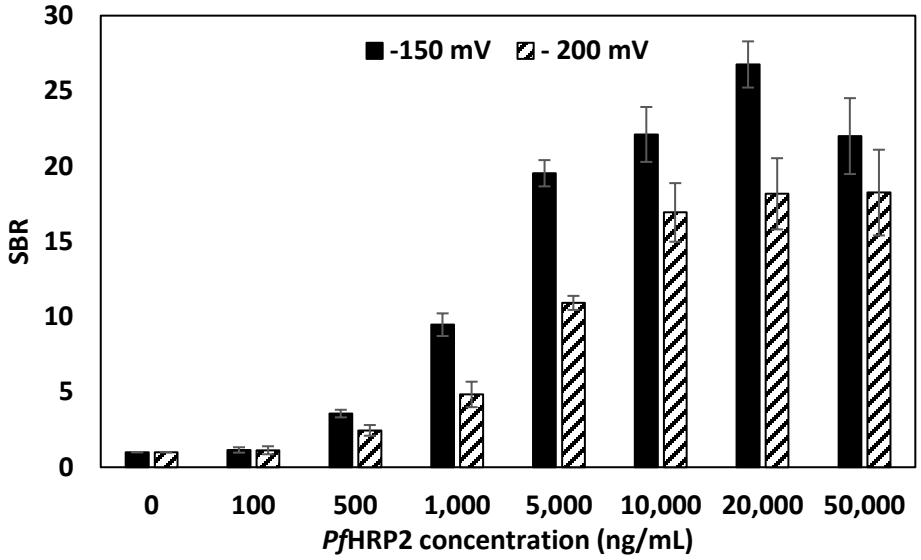

Figure 4-13. Amperometric signals of PfHRP2 diluted in human plasma using a bias potential of -200 mV (solid) and -150 mV (striped). The scheme is based on thiol immobilization method using 4AP as the substrate. Each bar represents the mean ± SD of two measurements.

4.3 Methylene blue-based electrochemical assay

We have developed new approaches for detecting *Pf*HRP2 by using $Ru(NH_3)_6^{3+}$, which relies on methylene blue (MB) as electron mediator for increasing electron transfer within electrochemical redox cycling as shown in Fig. 4-14. The utilization of a mediator assists the electron transfer within electrochemical redox cycling [108]. MB is a well-known electrochemical properties, which has been used as an electron transfer mediator within in redox cycling [105,106]. The electron transfer scheme is formed by $Ru(NH_3)_6^{3+}/Ru(NH_3)_6^{2+}$ redox cycling at the outer sphere

and MB_{ox}/MB_{red} react at the inner surface. When a negative potential is supplied from the power supply, $Ru(NH_3)_6^{3+}$ is reduced to $Ru(NH_3)_6^{2+}$ which reacts with MB_{ox} and oxidizes back to $Ru(NH_3)_6^{3+}$, the electron transfer process for EC redox cycling is enhanced due to regeneration of $Ru(NH_3)_6^{3+}$ for each redox cycling.

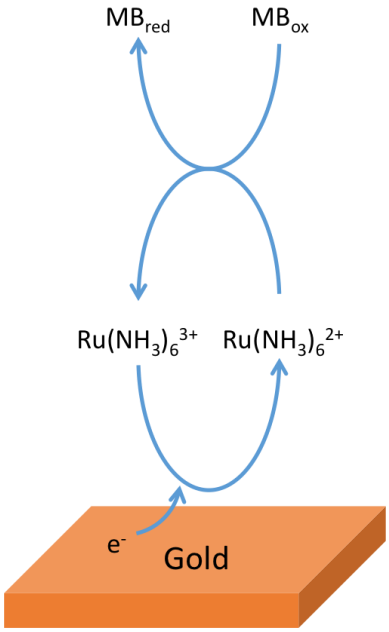

Figure 4-14. Schematic of electrochemical redox cycling based on the redox reaction between MB and $Ru(NH_3)_6^{3+}$.

4.3.1 Materials and methods

For this bioassay development, we utilized the same immobilization method as addressed in Section 4.2.2.3. For the selection of substrate, hexaaminеruthenium(III) chloride ($Ru(NH_3)_6^{3+}$), MB, phosphate-buffered saline (PBS, pH 7.4) and other reagents for buffer solutions were obtained from Sigma-Aldrich (St. Louis, MO). StabilBlock® Immunoassay Stabilizer was obtained from SurModics, Inc.

4.3.2 Antibody immobilization optimization

With the development of this sensor, the protocol we used was identical to what was described in Section 4.2.2.3. The capture antibodies are thiolated with Traut's reagent for 1 hr incubation, followed by immobilized thiolated antibody on gold sensor for 1 hr. Then, we applied a surface blocker, which is a stabilizer containing with PBS-casein for 30 min. After washing away the blocker, compressed N_2 was used to blow away the residues on the gold sensor, which were stored in a dehumidified chamber before assembly with the other pieces. For the negative control sensor, capture antibody was not immobilized on the surface. However, the control sensor was coated with a blocker to prevent *Pf*HRP2 binding. The negative control sensor will generate a background signal, which can be used to determine a false measurement. In the immunoassay electrochemical scheme we proposed, the current value for control sensor is always higher than the testing sensor. With this control sensor, we can validate the accuracy of the test by comparing the result with the background signal generated by the control sensor. Therefore, the quality and reliability of the POC diagnostic can be improved.

4.3.3 Substrate optimization

The bioassay detection scheme is illustrated in Fig. 4-15. The electron transfer rate is faster when there is no *Pf*HRP2 on the electrode surface and results in a higher signal. When the target is bound to the surface, the detection antibody binds to the sensor surface, effective forming an insulating layer. This insulating layer is proportional to the concentration of the protein layer formed on surface and reduces electron transfer with the electrode. However, the detection antibody will be washed away if there is no target on the surface. Then, there is no obstacle for electron transfer when there is no protein insulating layer is formed on the surface. Based on this scheme, a sample without the target analyte should generate a large current, which becomes reduced with increasing concentrations of *Pf*HRP2 in the sample.

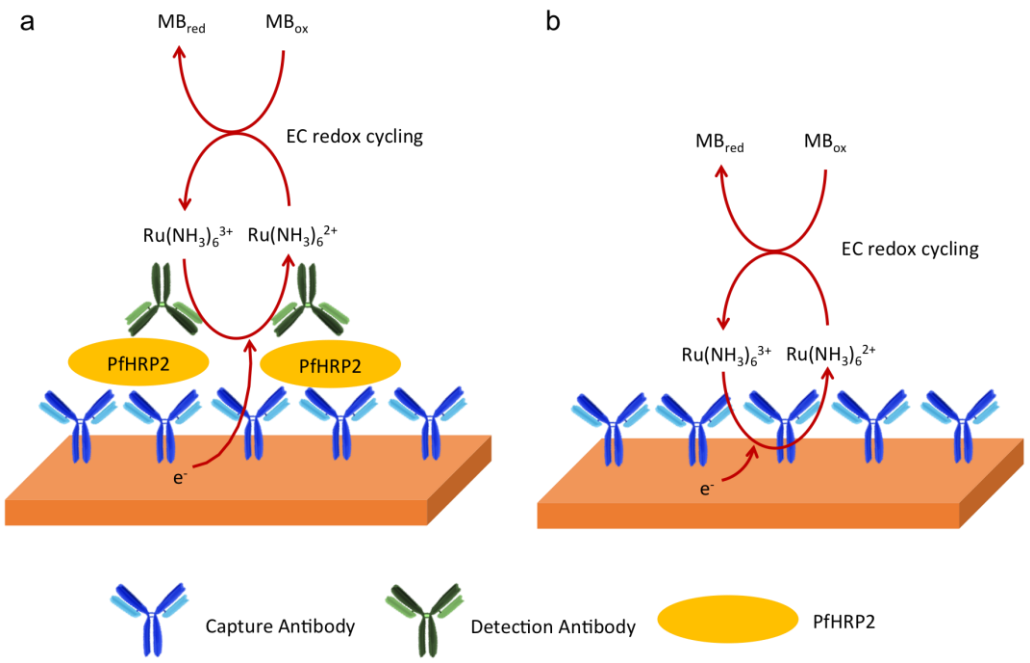

Figure 4-15. Schematic of electron transfer scheme on different antigen–antibody binding conditions. (a) When PfHRP2 is presented on surface, the electron transfer is inhibited. (b) When PfHRP2 is absence, the electron transfer is higher.

4.3.4 Electrical field preparation optimization

For the recognition of antigen binding on epitope of antibodies, it usually requires 1 hr for completing antigen-antibody binding in the corresponding surface. It is reported that the analyte transport rate can be accelerated by the production of an electrical field near the electrode surface [111]. With the electric field-driven incubation steps, it reduces the time-consuming incubation step to 10 min, while also enhancing the assay sensitivity.

In this work, we applied an electric field for assisting the antigen and detection antibody recognition steps. The transport of charged proteins is highly affected by the electrical field generated from electrode surface. It is reported that the more accelerated immunocomplex will be increased by the positive driving potential [100]. We have demonstrated a similar test by various potential of 200 mV, 400 mV, and 600 mV with the same driving time, followed by adding a

substrate for generating the redox cycling. The results showed that 400 mV exhibited the lowest signal, resulting from the most protein layer formed on the surface. However, 600 mV exhibited worse performance than 400 mV since a higher driving potential results in more electrostatic repulsion causing the immunocomplex to be slower than the transport rate.

The potential driving period was as investigated. We have tested the different potential durations from 1 min to 5 min at 400 mV, followed by $Ru(NH_3)_6^{3+}$ and MB reaction. As shown in Fig. 4-16, the lowest signal was generated at 3 min, which indicates that there is the most protein layer developed on the surface. Interestingly, the 4 min driving time exhibited the similar signal to background performance as 3 min driving time. However, it is favorable to apply a shorter driving potential time, thus, 3 min of driving time at 400 mV driving potential was selected for antigen-detection antibody complex formation on the sensor region.

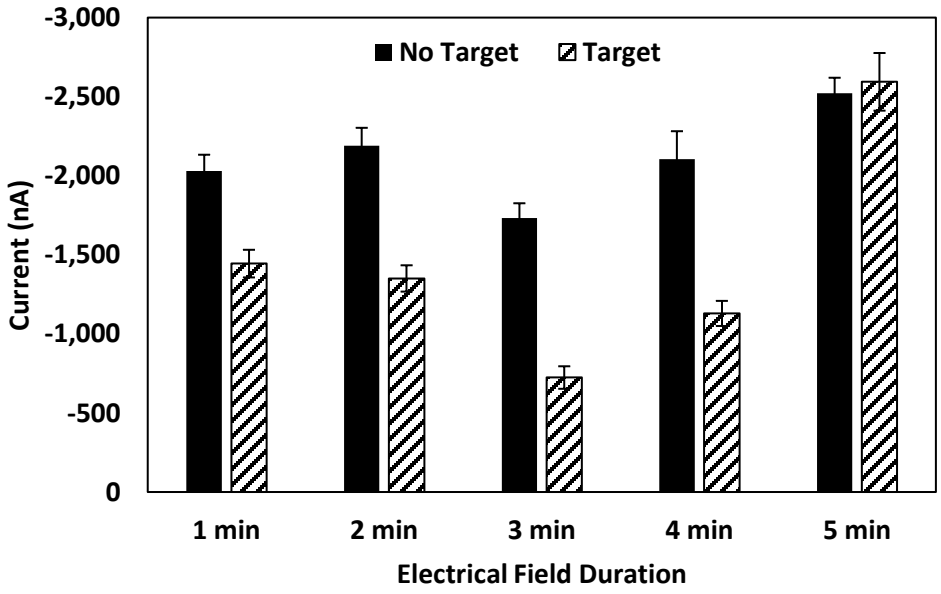

Figure 4-16. Effect of different duration of 400 mV driving potential on whole blood samples containing 10 μg/mL for comparing the value of target and without target. Each bar represents the mean ± SD of three separate measurements obtained using new sensors.

To validate this electric field incubation concept for protein recognition, measurements of human blood spiked with 10 µg/mL *Pf*HRP2 were performed. Measurements were also performed without electrical field preparation for comparison. As shown in Fig. 4-17, the electrical field incubation group exhibited a lower voltammetric detection current, resulted from a larger amount of protein layer forming on the surface. Conversely, there is less protein layer on the surface without an electric field driven, resulting in a higher detection current.

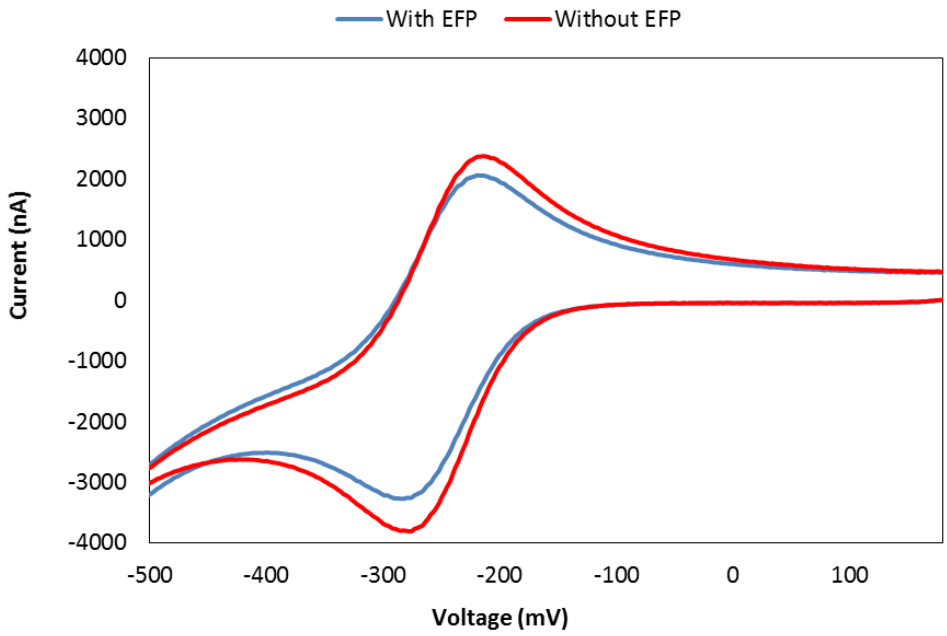

Figure 4-17. Cyclic voltammograms of whole blood samples containing 10 µg/mL with electrical field preparation (EFP) and without EFP using open well chips.

To validate the proposed scheme on the microfluidic cartridge, measurements of human blood spiked with *Pf*HRP2 were also performed. As shown in Fig. 4-18, the 10 µg/mL *Pf*HRP2 sample exhibited a lower voltammertric current signal since the electron transfer rate was inhibited by the protein formation on the substrate. However, the sample without *Pf*HRP2 showed a higher current value due to the negligible protein layer presented on surface and resulted in a faster electron transfer rate.

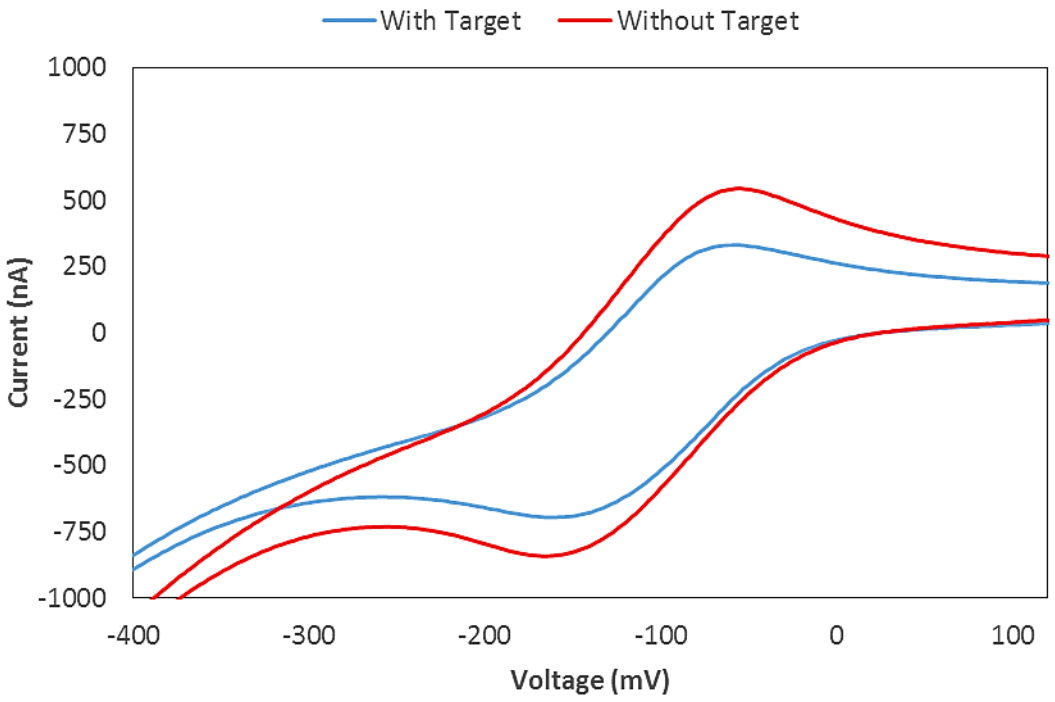

Figure 4-18. Cyclic voltammograms of whole blood samples spiked with 10 µg/mL PfHRP2 and without PfHRP2. The measurement is performed using a microfluidic cartridge.

4.4 Summary

In this chapter, we characterized and optimized the design and performance of an electrochemical assay for *Pf*HRP2 detection. Our initial efforts were focused on an ELISA-based detection scheme using Px and TMB as the reporter and substrate, respectively. We investigated different immobilization methods, including ones based on adsorption, amine covalent binding and thiol covalent binding. Covalent binding resulted in a wider detection range compared with adsorption, however, amine covalent binding is complicated and time-consuming. Thiol covalent binding offered improved performance compared with amine covalent binding while being faster and simpler. We also evaluated two substrates, TMB/H_2O_2 and 4AP/H_2O_2, and the use of electrical field-assisted protein recognition/binding which improved the assay stability and reduced the processing time, respectively. We then focused our efforts on a MB-based electrochemical assay

to enhance assay stability for long-term storage. With the nonenzymatic reagent and stabilized antibody, the proposed immunoassay exhibited higher stability than the first generation assay. Reagents are dried and protected by optimized stabilizing condition, the cartridge stability can maintain for a month at room temperature with minimal signal loss.

Chapter 5. Finger-powered microfluidic pump

5.1 Motivation

Microfluidic pumping based on finger actuation is an attractive method due to its simplicity and ease of fabrication. Prior finger-powered pumps are based on complicated fabrication processing or require additional fluidic components (valves, diodes) which can suffer from poor reproducibility [93–95]. To address these issues, we have explored the development of a valveless, piston-based micropump, which is robust and can easily be incorporated into plastic microfluidic devices.

5.2 Materials and methods

5.2.1 Finger-powered pump fabrication

PDMS prepolymer and curing agents (Sylgard 184) were obtained from Dow Corning (Midland, MI). PDMS was fabricated by mixing PDMS prepolymer and curing agents, degassed and poured onto the molds, and cured for 2 h at 80 °C. Individual PDMS pieces were cut by using CO_2 laser cutter. 1.5 mm-thick PMMA and rubber gaskets were obtained from McMaster-Carr (Elmhurst, IL). Prior to fabrication, PMMA was rinsed with 2-propanol, deionized (DI) water and dried with purified N_2 gas. Capillary tubes were purchased from Sigma (St. Louis, MO) and double-sided adhesive film was purchased from Adhesive Research (Glen Rock, PA). Fluorescent dye for examining washing efficiency within microchannel was ordered from ThermoFisher (Waltham, MA), and the image was captured by fluorescent microscope with absorption/emission wavelength at 347/448 nm. Colored dyes for flow visualization were purchased from a local vendor.

5.2.2 Finger-powered pump characterization

Flow experiments were performed using microchannels having a height of 100 μm, length of 15 cm and varying widths (100 μm, 200 μm, 400 μm, 600 μm, and 800 μm). 80 μL of colored dye was added to the reservoir prior to bonding the top PMMA layer. The flow was initiated by placing metal weights on top of the piston and recorded using a video camera. The flow rate was

calculated from still frame images of the video recordings by measuring the distance of the flow front at specific time intervals. We compared our experimental results with theoretical calculations of 2D pressure-driven flow inside a rectangular microchannel.

Measurements of the actuation force were performed using an M&A Instruments digital push-pull force gauge. The force gage was mounted on a vertical stage and positioned so that the compression rod was aligned with the piston of the cartridge (Fig. 5-1). The force gauge was connected to a PC and measurements were recorded using the manufacturers' software. Measurements were performed using microchannels having various widths filled with colored dye.

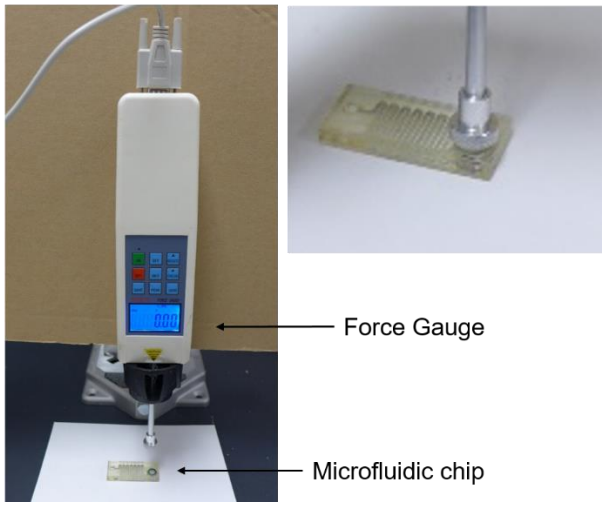

Figure 5-1. Photograph of experimental setup for piston actuation force measurements. The compression rod is aligned with the piston, and the resulting data is transmitted to a PC. The inset shows a close-up view of the compression rod pressing the piston during a measurement.

5.3 PDMS membrane-based pump

The first generation of our finger-powered pump is shown in Fig. 5-2. It consists of two layers of PMMA with a single PDMS layer in the middle, which were bonded together by adhesive film. A positive pressure was applied on the PDMS membrane by depressing it with a finger, resulting in the liquid being pushed into the microchannel. Upon release of the membrane, we

observed that some of the liquid flowed back into the reservoir due to the negative pressure generated from the recovering motion of the membrane. Thus, we investigated methods to fabricate one-way valves inside the microchannel to prevent backflow (Fig. 5-3). For the fabrication of the PDMS valve, a 100-µm thick PDMS flap was etched using a CO_2 laser cutter.

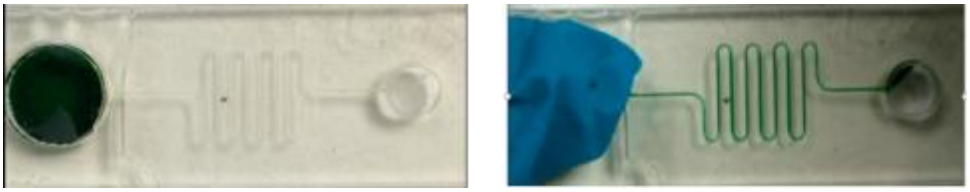

Figure 5-2. Photograph of the PDMS membrane-based pump before (left) and after(right) finger actuation.

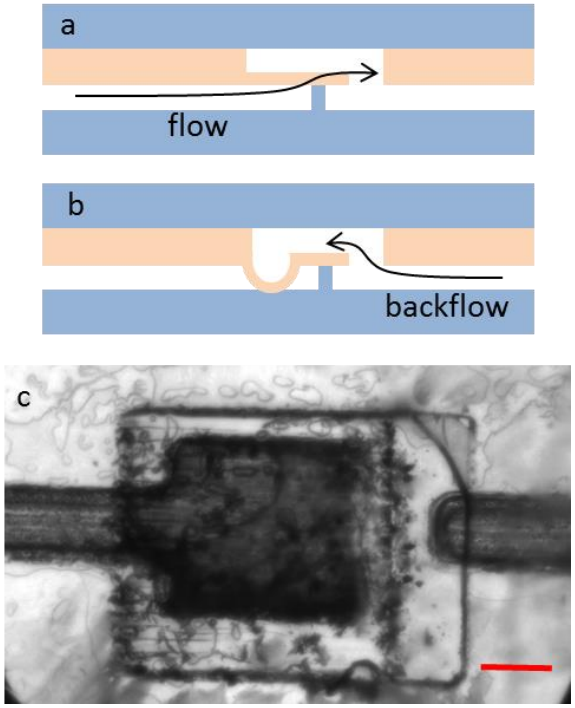

Figure 5-3. (a)(b) Schematic of the working principle of the fluidic valve to regulate flow. (c) Top view the one-way valve captured by optical microscopy. Scale bar, 500 µm.

We integrated three reservoirs into a single cartridge and performed flow testing using colored dye as shown in Fig. 5-4. Although the valve was capable of preventing backflow and regulating the flow direction, it exhibited some limitations. First, the liquid could not fully cover the sensor region, thereby hindering the accuracy of electrochemical reaction. Second, liquid leaking occurred frequently during the third activation step due to weak bonding strength between PDMS and PMMA. Last, the alignment between the PDMS and PMMA layers is complicated, especially for the valve's fabrication which requires precise alignment. Due to these issues and difficulties, we investigated alternative pump designs.

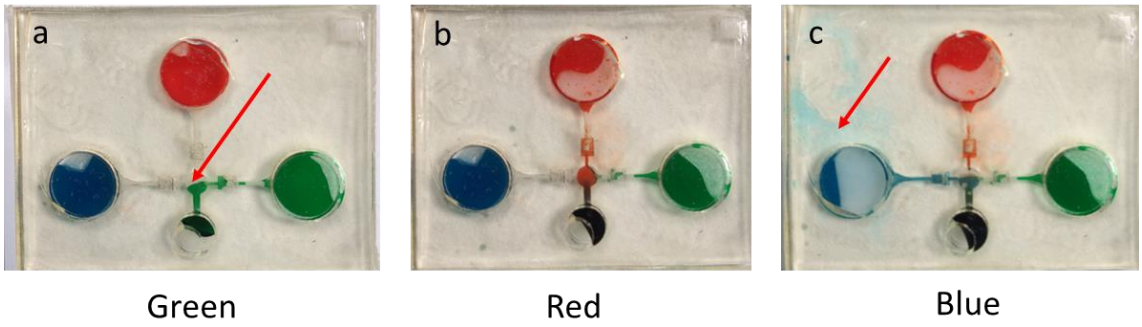

Figure 5-4. Microfluidic cartridge testing using color dyes. (a) The green dye was dispensed toward outlet. The arrow indicates poor liquid coverage for sensor region. (b)(c) Red and green were dispensed sequentially. The arrow reveals blue dye leaking resulting from incomplete bonding.

5.4 Piston-based pump

To address the limitations of the PDMS membrane pump described above, we employed a rigid piston as the transducer element. The design is similar to a mechanical piston, where a rigid piston slides inside a hollow cylinder, as shown in Fig. 5-5. Three different piston designs were investigated. In the first design, the high friction generated between the PDMS and PMMA resulted in the PDMS on the outer layer break, as indicated by the red circle in Fig. 5-5a. In the second design, a thinner PDMS membrane was placed on top of a PMMA notch, as shown in Fig. 5-5b. After the piston was pressed, the head of piston would depress the PDMS membrane in a concave

structure and push the liquid underneath. The membrane formed a closed region after the piston was depressed, to prevent liquid leaking. However, the piston tended to make slight contact with the PMMA via the top of notch after it was depressed, which did not provide sufficient area to keep the piston steady, highlighted by the red circle as shown in Fig. 5-5b. When this occurred, the piston would tilt causing the liquid to leak. Therefore, we modified the design by increasing the height of the PMMA notch, enlarging the reservoir and increasing the piston contact area after it is depressed, as shown in Fig. 5-5c. Also, a circular lid containing double-sided adhesive film was added to the top of the piston to prevent liquid backflow after actuation. Based on this new design, the piston remained oriented upright to prevent leaking. The adhesive film on the underside of the lid bonds to the top surface of the chip after being depressed to prevent backflow.

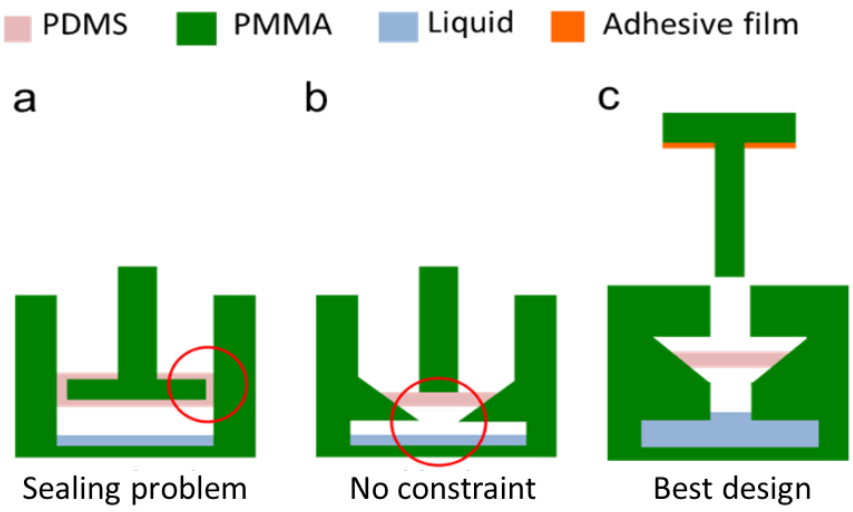

Figure 5-5. Schematics of the three different designs of piston-based finger-powered pumps. Red circles indicates defects during actuation. (a) The PDMS on the outer layer breaks due to the friction force. (b) The depressed piston is tilting and results in leaking. (c) The optimal pump design.

Applying the piston pump design, a mock microfluidic cartridge was designed and filled with colored dye for enhancing visualization. Red dye was added through the capillary tube, and blue dye, DI water, and yellow dye were sequentially pumped into the sensing region from

reservoirs, as shown in Fig. 5-6. The performance of this design was superior to our prior designs and did not suffer from poor sensor coverage or leakage. However, we observed another issue with this design: bubble generation. Air inside the reservoirs formed bubbles in the microchannels after actuation, resulting in channel blockage and poor sensor coverage. Although the piston-based pump is functional, it suffers from poor reliability and requires a time-consuming fabrication process.

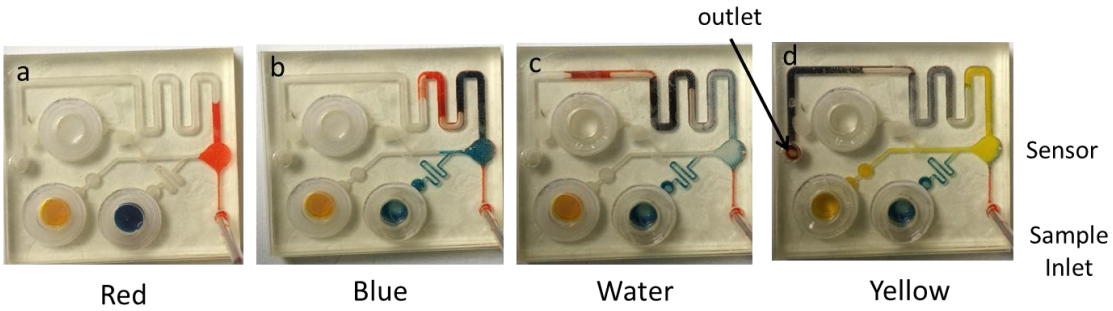

Figure 5-6. Microfluidic cartridge testing with colored dye. (a) Red dye was dispensed via capillary tube, and blue dye (b) DI water (c) and yellow dye (d) were sequentially dispensed by depressing the pistons.

5.5 Gasket-based piston pump

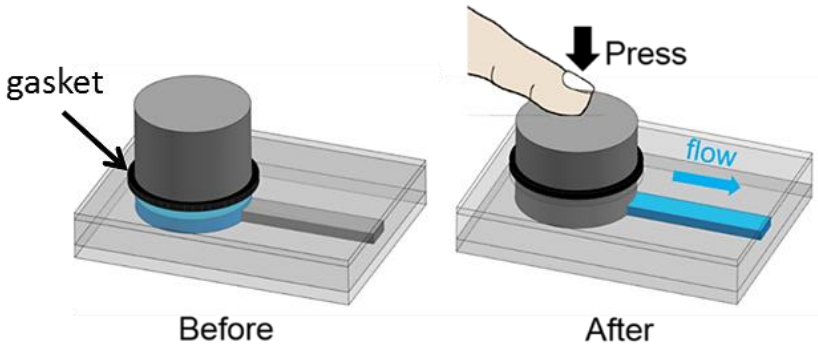

Figure 5-7. Schematic of the modified piston-based microfluidic pump before (left) and after (right) actuation. Arrow indicates the rubber-based gasket to prevent liquid leaking.

To address the limitations of our piston-based pump described above, we modified the design by incorporating a rubber gasket ring to secure the piston in the cartridge which provided a leak-free seal. When the piston is depressed, it generates a uniform force on the liquid, which is driven through the channel as shown in Fig. 5-7. Due to the simple fabrication process, this technique provides further simplicity, reliability, and reproducibility for microfluidic device generation. To evaluate the effectiveness of this design, mock microfluidic cartridges were fabricated, filled with color dyes and tested.

To characterize the functionality of this pump, we performed several experiments to evaluate the effectiveness of the pumping mechanism. First, we evaluated the minimum force to overcome the friction between the rubber gasket and the piston to better understand the force required to actuate the piston. We evaluated the force by placing different weights on top of the piston and noted when the piston started moving downward. The measurements were performed using five new chips and the average force was 1.35 N. However, we observed that the bottom of the gasket became wet after the piston was depressed, which could influence the friction. Therefore, we repeated the experiment with a pre-wetted gasket, and obtained an averaged force of 1.29 N. This result indicates that the friction between the gasket and piston does not dependent on whether the gasket is wet or dry.

To characterize the flow performance of this pump, flow rate measurements were performed using microchannels having varying widths and a fixed pressing force of 1.84 N. As shown in Fig. 5-8, the flow rate is proportional to the channel width where wider channels exhibited larger flow rates. We briefly performed theoretical calculations of the flow rate inside a rectangular microchannel using a simplified 2D model to compare with our experimental results. We first estimated the Reynolds number (Re) using Eq. 5.1, where μ is the fluid viscosity, D_h is the hydraulic diameter of the channel, V is the flow velocity, and ρ is the fluid density. The hydraulic diameter for a rectangular channel is defined as $4A/P$, where A is the cross-section area, and P is

the wetted perimeter. The dimensions of the microchannels were measured using optical microscopy, the flow velocities were measured using still frame images of video recordings of fluid flow in the channel and we assumed the fluid properties of water at 20°C. For microchannels of widths between 100 – 800 μm, the Re ranged from 0.1 to 0.5, which is fully laminar. By inserting these values into Eq. 5.2, we obtain entrance lengths (L_e) less than 10 μm. Since the length of the microchannels is 15 cm, the entrance length is <0.01% of entire microchannel, and we can assume that the flow is fully developed.

$$Re = \frac{\rho V D_h}{\mu} \qquad (5.1)$$

$$\frac{L_e}{D_h} \approx 0.06\, Re \quad [115] \qquad (5.2)$$

We also assumed that the flow inside the microchannel was steady with no-slip boundary conditions at the channel walls and a uniform pressure gradient along the length of the channel. Based on these assumptions, the volumetric flow rate inside a circular microchannel can be described by the Hagen-Poiseuille law (Eq. 5.3), where Q is the volumetric flow rate, R is the radius, L is the channel length and ΔP is the pressure drop across the entire channel.

$$Q = \frac{\pi R^4}{8\mu}\frac{\Delta P}{L} \qquad (5.3)$$

Eq. 5.3 can be simplified as:

$$Q = \frac{\Delta P}{R_H} \quad [116] \qquad (5.4)$$

where R_H is the hydraulic resistance, which is defined by the geometry of channel. The hydraulic resistance for a rectangular channel can be calculated by the summation of Fourier series as shown in Eq. 5.5 [117]

$$R_H = \frac{12\mu L}{wh^3\left(1-\frac{h}{w}\left(\frac{192}{\pi^5}\sum_{n=1}^{\infty}\frac{1}{(2n-1)^5}\tanh\left(\frac{(2n-1)\pi w}{2h}\right)\right)\right)} \qquad (5.5)$$

where *w*, *h* are the width and height of the channel, respectively. For channels with a high aspect ratio ($h/w < 1$), which is typical of microfluidic systems, Eq. 5.5 can be reduced to the following:

$$R_H = \frac{12\mu L}{wh^3}\left[1 - \frac{192h}{\pi^5 w}\tanh\left(\frac{\pi w}{2h}\right)\right]^{-1} \qquad (5.6)$$

By combining Eq. 5.4 and 5.6, we can obtain an expression for *Q* inside a rectangular channel as a function of ΔP and the channel geometry:

$$Q = \Delta P \times \frac{wh^3}{12\mu L}\left[1 - \frac{192h}{\pi^5 w}\tanh\left(\frac{\pi w}{2h}\right)\right] \quad (5.7)$$

To account for the friction between the piston and rubber gasket, 0.5 N was added to ΔP. Comparison of the experimental and theoretical values obtained from Eq. 5.7 is shown in Fig. 5-8.

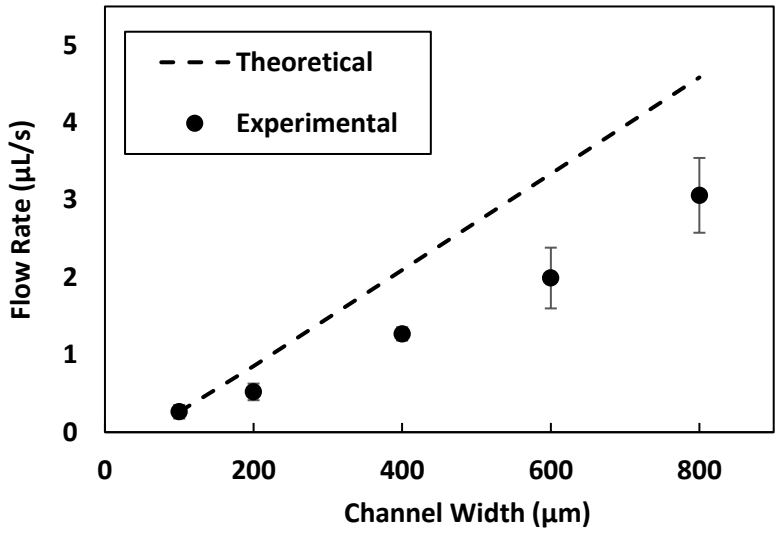

Figure 5-8. Experimental vs. theoretical flow rates for rectangular microchannels 100 µm in height, 15 cm long with varying widths. Each data point is the mean ± SD of five measurements using new chips.

While the overall trends of the experimental and theoretical results are similar, the deviation between the two sets of data is fairly significant, which we attribute to three sources of experimental error. First, our theoretical analysis was based on a rectangular microchannel;

however, the sidewalls of the actual microchannels are slightly angled inward due to the laser cutting process. Therefore, theoretical analysis based on a trapezoidal microchannel could provide a more accurate comparison. Relatedly, the piston is not perfectly cylindrical due to the laser cutting process and the area of the top surface is roughly 5% larger than the bottom surface. Therefore, as the piston is depressed, the contact area with the gasket expands, resulting in a larger friction force. This would cause the actual pressure exerted on the liquid to be less than we predicted, resulting in a lower flow rate. Last, we observed that not all of the liquid is pushed into the microchannel when the piston is pressed. There is a small gap between piston and reservoir which becomes filled with the liquid. Thus, the actual pressure drop will be slightly less than we predicted.

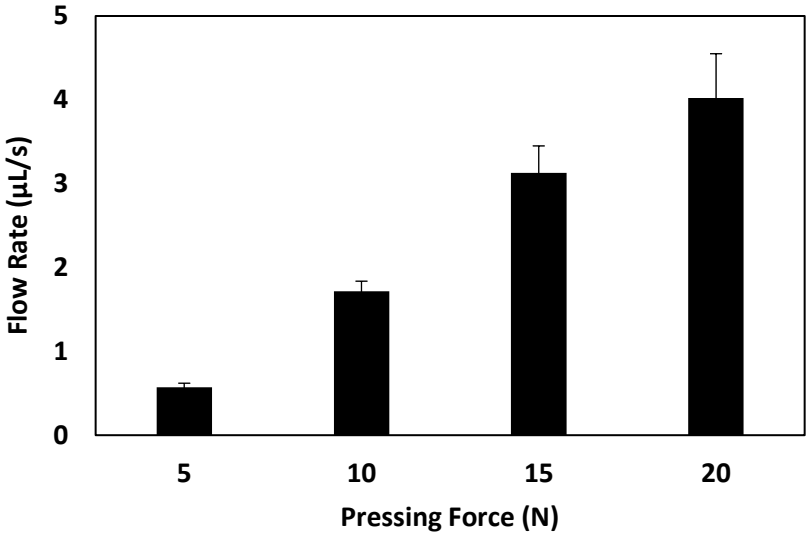

Figure 5-9. Flow rate vs. pressing force for rectangular microchannels 100 µm high, 400 µm wide and 10 cm long. Each bar represents the mean ± SD of five separate measurements.

Next, we evaluated the effect of the pressing force on the flow rate. This experiment was carried out using microchannels 400 µm wide, 100 µm high and 10 cm long filled with colored dye, applying different weights to initiate the flow. As shown in Fig. 5-9, larger pressing forces generated faster flow rates which were proportional to the pressure drop.

Moreover, we carried out an experiment to measure the pressing force required to completely depress the piston with microchannels of varying widths filled will colored dye. As shown in Fig. 5-10, the pressing force is inversely proportional to the channel width since the fluidic resistance is a function of the channel size [118]. Specifically, larger pressing forces are required to pump fluids inside smaller channels. The smallest channel that we tested (100 µm) required ~18 N of force to generate flow at 0.8 µL/s, which is well within the capability of an average human [119].

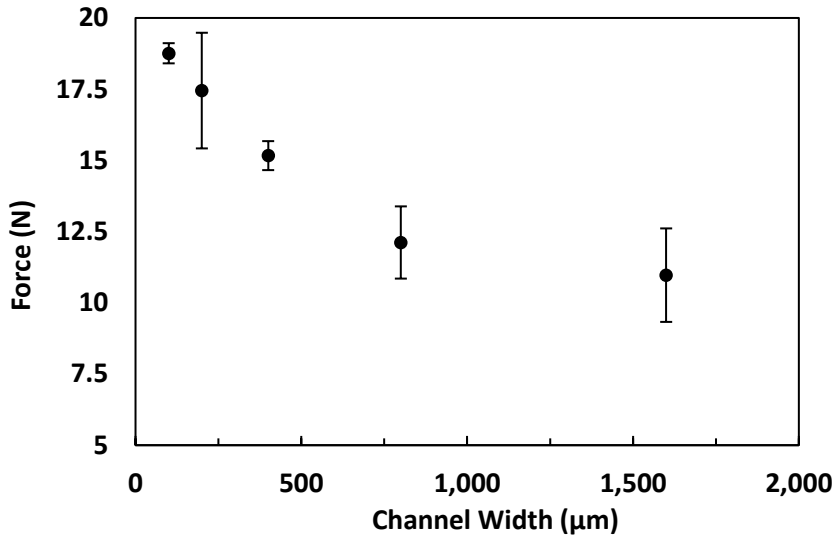

Figure 5-10. Pressing force required to pump water in rectangular microchannels 100 µm high, 10 cm long and of varying widths. Each data point represents the mean ± SD of three separate measurements.

Based on these results, the flow rate of this pump is influenced by the pressing force, which can vary from test to test or person to person. Therefore, we investigated whether the flow rate (pressing force) had a significant impact on the washing efficiency. To evaluate the influence of the pressing force on the washing efficacy, we fabricated a microfluidic device (Fig. 5-11a) incorporating a finger-powered pump and a reservoir pre-loaded with fluorescence dye and PBS, respectively, and applied varying pressing forces (2, 5, 10, and 20 N) to depress the piston.

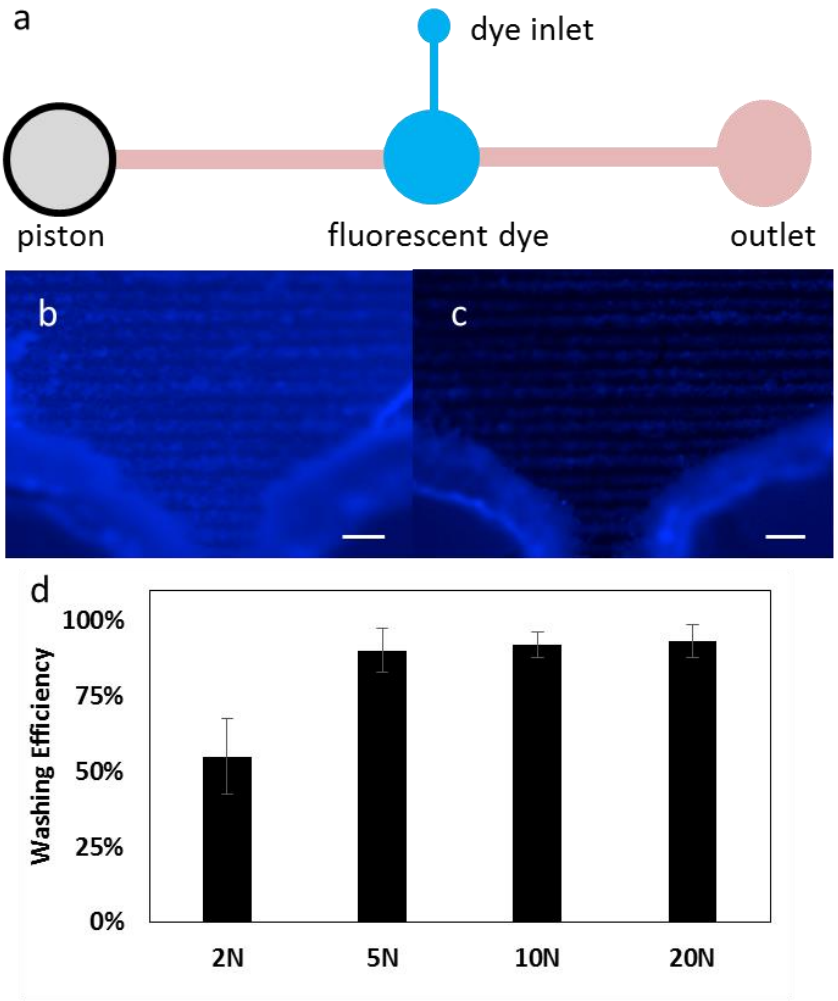

Figure 5-11. (a) Schematic of microfluidic device for evaluating washing efficiency. Fluorescent images of the reservoir before (b) and after (c) washing. Scale bars, 100 µm. (d) Washing efficiency in rectangular microchannels at 100 µm high and 400 µm of varying weights. Each bar represents the mean ± SD of three separate measurements.

The amount of residual dye was quantified by measuring the fluorescence signal in the reservoir following washing via the finger-powered pump. The intensity of the fluorescence signals were quantified using NIS-Element software. Measurements of the background signal (I_B), fluorescence intensity before washing (I_{before}), and after washing (I_{after}) were performed using new microfluidic chips. The background signal was measured at a region on the chip not containing any fluorescence dye. The washing efficiency was calculated using the following equation:

$$Washing\ efficiency = \frac{I_{after} - I_B}{I_{before} - I_B} \times 100\ \% \qquad (5.8)$$

The results of this experiment are shown in Figs. 5-11b-d. Fluorescence images of the reservoir containing the fluorescence dye before and after washing are shown in Fig. 5-11b and c, respectively. The washing efficiency for different pressing forces is presented in Fig. 5-11d, which shows that there is not much improvement in the washing efficiency with pressing forces > 5 N. Therefore, while larger pressing force can generate a faster flow rate, it doesn't improve the washing efficiency or influence the detection performance.

5.6 Summary

In this chapter, we have demonstrated a new finger-powered pump for transporting liquids inside plastic microchannels. This pump consists of a rigid mechanical piston and a rubber gasket. Depressing the piston generates a uniform pressure on the liquid inside the reservoir, which drives it through the channel. The tight clearance between the piston and gasket prevents leaking and backflow after activation. To characterize the effectiveness of this pumping mechanism for transporting liquids inside microchannels, we measured the pressing force required for varying channel widths. These results revealed that the pressing force is inversely proportional to the channel width where larger forces are required to drive liquids in smaller channels. The smallest channel that was tested (100 μm) requires ~18 N of force to generate flow at 0.8 μL/s, which is well within the capability of the average human. Additionally, we observed that the rate at which the piston was depressed had a negligible impact on the flow performance. These results demonstrate that our finger-powered pumping mechanism is a simple and effective method for generating driving liquids in microfluidic devices.

Chapter 6. Microfluidic cartridge development

6.1 Motivation

In Chapters 4 and 5, we presented the development of an electrochemical assay for *Pf*HRP2 detection and a finger-powered pump. In this chapter, we combine these technologies to develop a finger-powered microfluidic electrochemical assay for rapid measurements of *Pf*HRP2 in whole blood samples. Two generations of prototypes were created: the first was based on the enzymatic detection scheme (as described in Section 4.2) and the second was based on a nonenzymatic detection scheme (as described in Section 4.3).

6.2 Materials and methods

6.2.1 Microfluidic cartridge design

The microfluidic cartridge consists of three layers of PMMA. The microfluidic network was designed using AutoCAD software and etched into the PMMA using a CO_2 laser cutter (Universal Laser Systems, Scottsdale, AZ).

6.2.2 Microfluidic cartridge fabrication

The bottom layer consists of circular reservoirs (7 mm in diameter and 1.5 mm deep) for storing liquid reagents. The electrochemical sensor, consisting of a working electrode (WE), reference electrode (RE) and counter electrode (CE), was deposited on the back side of middle layer through a shadow mask, and chromium/gold were sequentially evaporated with thicknesses of 15 nm and 60 nm, respectively using a thermal evaporator (Jefferson Hills, PA).

1.5 mm-thick PMMA and rubber gaskets were obtained from McMaster-Carr (Elmhurst, IL). Prior to fabrication, PMMA was rinsed with 2-propanol, deionized (DI) water and dried with purified N_2 gas. Capillary tubes were purchased from Sigma (St. Louis, MO) and double-sided adhesive film was purchased from Adhesive Research (Glen Rock, PA). The middle and top layers incorporate through-holes for the pistons, capillary tube inlet and air ports. Rubber gaskets were

installed between the middle and top layer, and all three layers were bonded together using double-sided adhesive. The pistons were laser cut from 3-mm-thick PMMA and inserted in each hole after the reagents were dispensed in the reservoirs.

Chemical and protein preparation were carried out as described in Chapter 4, and the fabrication of the finger-powered pump was carried out as described in Chapter 5. Microcontroller LaunchPad and data converter chip were purchased from Texas Instruments (Dallas, TX). Amplifiers and channel multiplexers were purchased from Analog Devices (Norwood, MA). Discrete components and miscellaneous parts were purchased from Digi-Key (Thirf River Falls, MN). For our prototype device, we used a Nexus 5 smartphone running on Android 5.0.2 OS.

6.2.3 Amperometric measurements

Amperometric measurements and signal processing were carried out by a custom detection circuit, named aMEASURE [113] (Fig. 6-1), which was developed by Sina Parsnejad in Dr. Andrew Mason's lab at MSU.

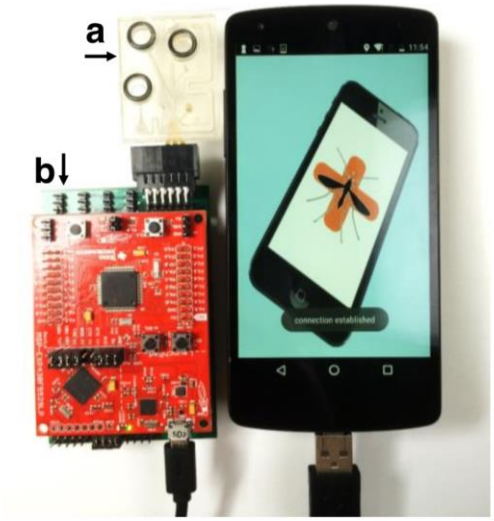

Figure 6-1. Photograph of our mobile phone biosensing platform. The microfluidic chip (a) directly plugs into aMEASURE (b), which is connected to the phone via the microUSB port using a USB OTG adapter.

This circuit is comprised of a custom analog readout board and a microcontroller, which provides a physical/electrical interface between microfluidic chip and the mobile phone. The circuit can support a current signal from 0.94 nA to 2.4 mA, and automatically adapts to response current levels. The circuit consumes very low power (90 mA) and can be powered for up to 7 hr using the mobile phone battery. The microfluidic cartridge (Fig. 6-1a) plugs into aMEASURE via an edgeboard connector. Step-by-step instructions for each measurement and test results are displayed on the phone though a custom Android app, developed by Linlin Tu in Dr. Guoliang Xing's lab at MSU.

6.3 First generation prototype device

6.3.1 Cartridge design

As shown in Fig. 6-2, our microfluidic cartridge consists of four components: reagent storage reservoirs, finger-actuated pistons, microchannel network, and an electrochemical sensor. The pistons are secured in place via rubber gaskets, which effectively seal off the reagents from the environment. Due to the mild hydrophobicity of native PMMA, the liquid reagents remain contained in the reservoirs until piston actuation. Two small air ports are placed downstream of the reservoirs to allow air exhaustion during actuation, thereby preventing bubble generation inside the fluidic network. The arrangement of the sample inlet, microchannels, and reagent reservoirs were designed to facilitate the assay protocol and enhance the detection performance. The capillary tube inlet is connected to the sensing region via a separate channel to minimize diffusion between the sample and reagents. Separate channels were employed for the reporter solution (R1) and substrate (R3) to prevent them from mixing, which would result in a high background signal. However, merging the microchannels for the PBS wash buffer (R2) and substrate (R3) did not have a significant impact on the background signal and was adopted to minimize cartridge size. Based on these design strategies, our microfluidic cartridge does not require any additional fluidic components, such as valves or diodes.

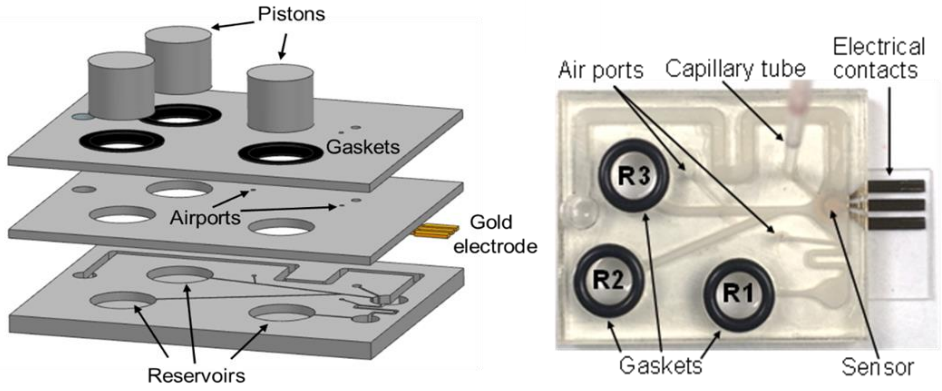

Figure 6-2. Exploded view of microfluidic cartridge (left). Photograph of the assembled microfluidic cartridge with relevant regions labeled. Reservoirs R1, R2 and R3 are designed to preload with a reporter solution, wash buffer and 4AP/H_2O_2 substrate, respectively. The dimensions of the cartridge are 40 mm × 30 mm.

To simplify the testing process, all the sample processing steps are integrated on a microfluidic cartridge. On the middle layer of the cartridge, we immobilized capture antibody on gold sensor and applied blocker to prevent a false-positive signal from non-specific binding. Next, we bonded the three PMMA pieces together using adhesive films. Color dyes were used to visualize fluidic transport within the cartridge, as shown in Fig. 6-3.

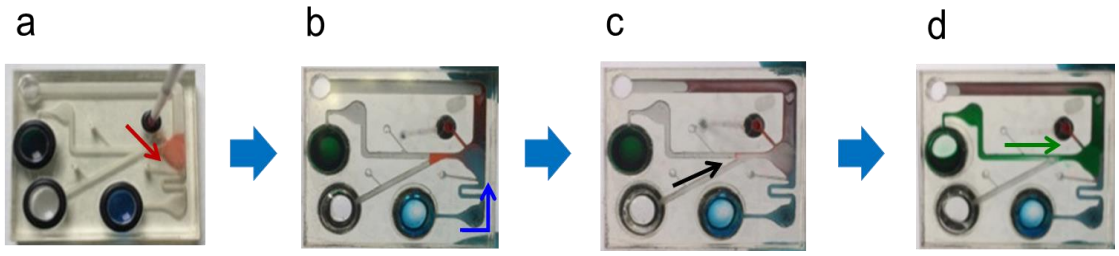

Figure 6-3. Microfluidic cartridge testing with color dye. Red dye was added by capillary tube, and blue dye, DI water and yellow dye were sequentially dispensed by depressing the pistons. (a) The sample is dispensed from capillary tube and flows toward the sensor region. (b) Detection antibody solution flows to the sensor by pressing piston R1. (c) Buffer washes away unbound detection antibodies by pressing piston R2 (d) Substrate flows to the sensor region by pressing piston R3.

The blue dye represents the detection antibody stored in R1, water in R2 represents the washing buffer to wash out the residue left on the sensor region, and the green dye in R3 represents the substrate. The results of this experiment indicate that all three reagents can be sequentially transported to the sensing region with negligible cross-contamination.

6.3.2 Device testing

To evaluate the performance of our prototype device, measurements were performed for *Pf*HRP2 detection, assay specificity and sensitivity. For assay specificity measurements, samples were spiked with three different antigens (*Pf*LDH, DEN-2 and *Pf*HRP2) at 10 µg/mL in PBS. For assay sensitivity measurements, human plasma samples were spiked with *Pf*HRP2 from 0.1 µ/mL to 20 µg/mL. 80 µL of PBS containing 10 µg/mL of anti-*Pf*HRP2 IgG, PBS and 4AP/H_2O_2 substrate were dispensed into reservoirs R1, R2 an R3, respectively, using a pipette. To initiate the assay, 20 µL of sample was dispensed into the cartridge using a capillary tube plunger. Next, a 400 mV electrical field was applied to the sensor for 3 min to facilitate protein recognition and binding. The value for voltage setting and incubation times are already characterized and addressed in Chapter 4. Px-conjugated detection antibody was delivered to the sensor by depressing piston R1. A second electrical field (200 mV) was applied for 1.5 min, followed by a rinsing step to remove unbound antibodies by pressing piston R2. Piston R3 was pressed to deliver the substrate solution, followed by amperometry measurement at a bias potential of -150 mV for 1 min. The entire detection process was completed in ≤ 6 min. Each measurement was performed at room temperature using a new microfluidic cartridge.

We evaluated the specificity of our *Pf*HRP2 assay by performing measurements using irrelevant targets including dengue virus type 2 (DEN-2) and *Pf*LDH, which is another malaria biomarker. The measurements were taken for each sample at 10 µg/mL in PBS. As shown in Fig. 6-4, the sample containing *Pf*HRP2 generated a SBR of ~16, whereas the irrelevant targets generated low SBRs similar to PBS sample (blank control). These results suggest that the capture

and detection antibodies used in this assay specifically bind to only *Pf*HRP2 thereby minimizing the likelihood of false positive measurements.

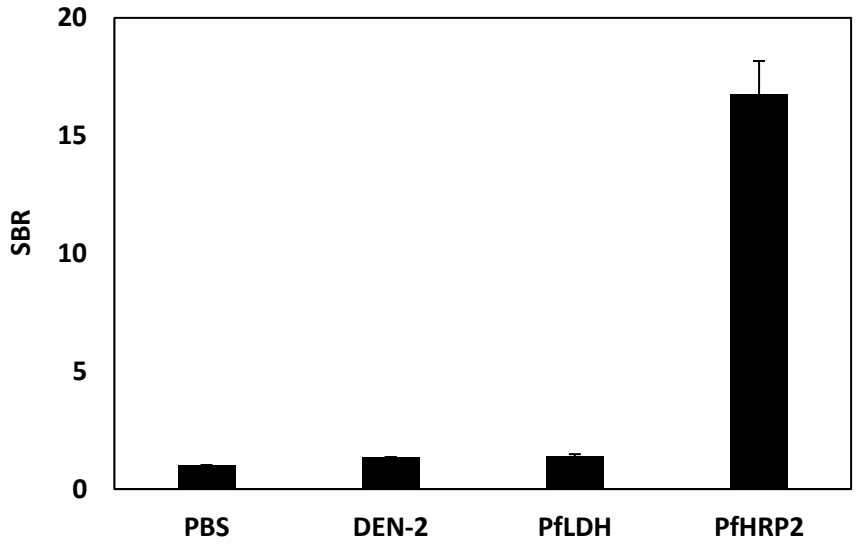

Figure 6-4. Specificity of PfHRP2 assay. Measurements were performed using DEN-2, PfLDH and PfHRP2 in PBS at a concentration of 10 µg/mL, and PBS as a blank control. Each bar represents of the mean ± SD of three separate measurements.

Next, experiments were performed to measure *Pf*HRP2 in human plasma samples at different concentration from 0.1 µg/mL to 20 µg/mL. As shown in Fig. 6-5, amperometric signals were clearly distinguishable at all of the tested concentrations with relatively smooth response profiles and minimal noise. In addition, this assay can detect a wide range of concentrations (0.1 µg/mL - 20 µg/mL), encompassing the clinical levels found in patients with *P. falciparum* infection [50], without sample dilution or concentration.

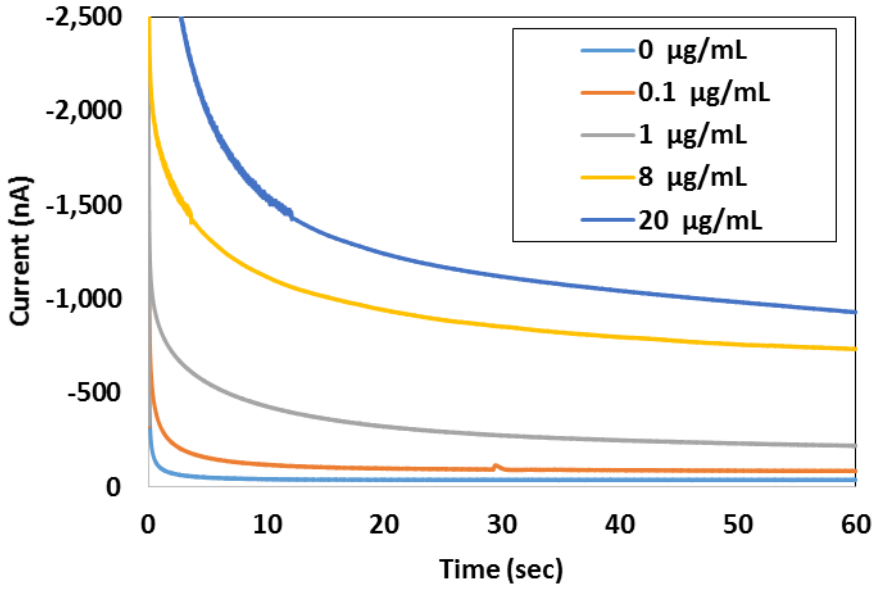

Figure 6-5. Amperometric signals of PfHRP2 diluted in human plasma. Measurements were performed at a bias potential of -150 mV.

6.3.3 Summary

For the first generation device, a wide detection range of 0.1 µg/mL to 20 µg/mL was achieved; however, the linearity was limited to 8 µg/mL. Liquid reagents are stored within the cartridge, thereby simplifying the testing process. Although all the sample processing steps are integrated in the cartridge, each measurement requires multiple steps, which can cause inconsistencies in the test results due to human error. Therefore, a simple cartridge design requiring a fewer number of steps is desired. In addition, the stability of lyophilized detection antibody complex, dried 4AP and H_2O_2 is questionable. H_2O_2 tends to decompose slowly under room temperature, however UV light catalyze the reaction. Additionally, H_2O_2 is a temperature sensitive chemical, which does not allow any freeze-drying or special treatment. It's difficult to dehydrate H_2O_2 under room temperature. Therefore, we are not able to store H_2O_2 under room temperature for a long time; alternative approaches for substrate selection and bioassay development are desired.

6.4 Second generation prototype device

We had a chance to demonstrate our first prototype and performed field-testing at the College of Medicine at the University of Malawi in March, 2017. We received comments and suggestions from the medical technicians there. We also noticed few disadvantages of first generation microfluidic cartridge and devoted time to develop a second generation device. With the redesigned device, it should provide more accurate results, simplify the processing steps and offer an extended shelf life at room temperature.

Also, the first generation of our electrochemical instrument was quite bulky, (2 in. × 3 in. × 1 in.). It is necessary to reduce the size of the instrument and make it portable and convenient for POC application. With the development of an electrical interface, the second generation of aMEASURE2 was developed, which is only 1 in. × 2 in. and consumes 250 mW (average) of power. The second-generation prototype incorporates a smaller detection circuit, and the microfluidic cartridge is connected to the circuit using a single-sided adapter, similar as the first generation device.

6.4.1 Cartridge design

For the first generation of microfluidic cartridge, the fabrication process suffers from poor alignment and results in an inconsistent device. Especially for the bonding of the top and middle layers, poor alignment results in a deviated gasket position which affects the piston movement. The consistency and accuracy of the alignment process affect the device quality and subsequent measurement reliability. To improve the alignment accuracy, an alignment device was developed, which is attached to the bottom of the cartridge, as shown in Fig. 6-6. The plastic holder was made by 3D printing and consists of four, 1-mm-diameter extruded pillars located at the four corners. Using this device, the lateral resolution of the alignment process is increased to 0.5 mm with improved consistency.

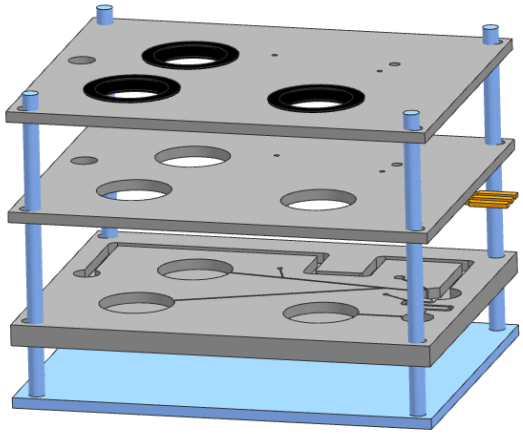

Figure 6-6. Schematic of the alignment device with a lateral resolution of 0.5 mm.

For the second generation device, a second electrochemical sensor was added for a negative control measurement. This negative control sensor does not contain *Pf*HRP2-specific antibodies and therefore generates a background signal. In the future, it is possible to modify this sensor to detect another biomarker, which would enable multiplexed measurements for improved diagnostic information. The microfluidic network was redesigned based on the updated detection scheme and second sensor as shown in Fig. 6-7. This design incorporates dried reagent reservoirs and only 1 piston for the buffer. The layout of sample inlet, microchannels, sensors and dry reagents was redesigned according to the nonenzymatic detection scheme.

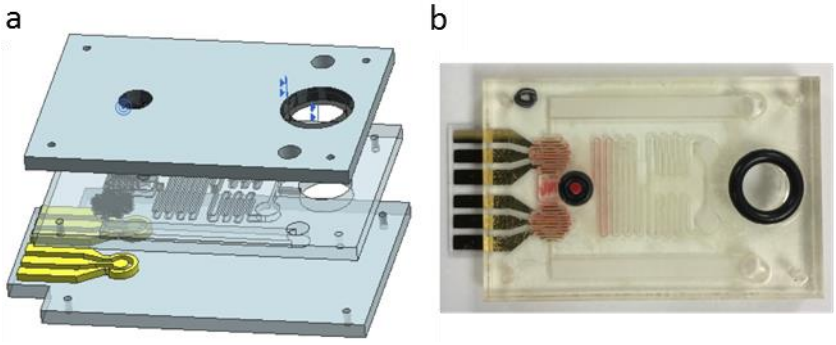

Figure 6-7. Exploded view of microfluidic cartridge (left). Photograph of the assembled microfluidic cartridge (right). Three reservoirs are reduced to one reservoir. The dimensions of the cartridge are 30 mm × 25 mm.

As shown in Fig. 6-8a, dried $Ru(NH_3)_6^{3+}$ and MB were pre-stored in the reservoirs respectively. Separate reservoirs isolated two chemicals before reconstitution. Also, the microchannel network splits equally and contain serpentine regions to improve reconstitution. The gold sensors are prepared using the same procedure as described in Section 6.2.2. Then, we combined the target and detection antibody, adding the steps together. The dried detection antibody is pre-stored in a reservoir designated for blood sample inlet. After the sample is added, the target will mix the detection antibody and generate the binding based on the epitope recognition. Before the mixture flow to the sensor region, we specifically incorporated a serpentine microchannel before flowing to the sensor area as shown in Fig. 6-8b. With the extra serpentine area, there is more contact area and enough time for improving the mixing and binding of the detection antibody/target.

Once the detection antibody, target, and capture antibody are bound to the sensor surface, a substrate solution is added for generating an electrochemical reaction. Unlike H_2O_2, $Ru(NH_3)_6^{3+}$ and MB are both stable at room temperature in dried form. As shown in Fig. 6-8a, we added 5 μL of $Ru(NH_3)_6^{3+}$ and MB in the reservoir, and let both chemicals dry in a low humidity chamber for one day. Once dry, both chemicals are stable without requiring refrigeration. For reconstituting $Ru(NH_3)_6^{3+}$ and MB on the cartridge, 150 μL of PBS is added to the reservoir under the piston. Once the piston is depressed, the liquid flows towards both regions and reconstitutes $Ru(NH_3)_6^{3+}$ and MB, respectively. Followed by a merging region to mix $Ru(NH_3)_6^{3+}$ and MB, and flow to the sensor region. As shown in Fig. 6-8c, compared with previous generation, there is less blood residue remained on the sensor area due to the modified sensor region. Also, the liquid fills with all the areas on the microfluidic cartridge; there is no observable dead volume; and a higher reconstitution rate is developed for all the dried reagents on the cartridge.

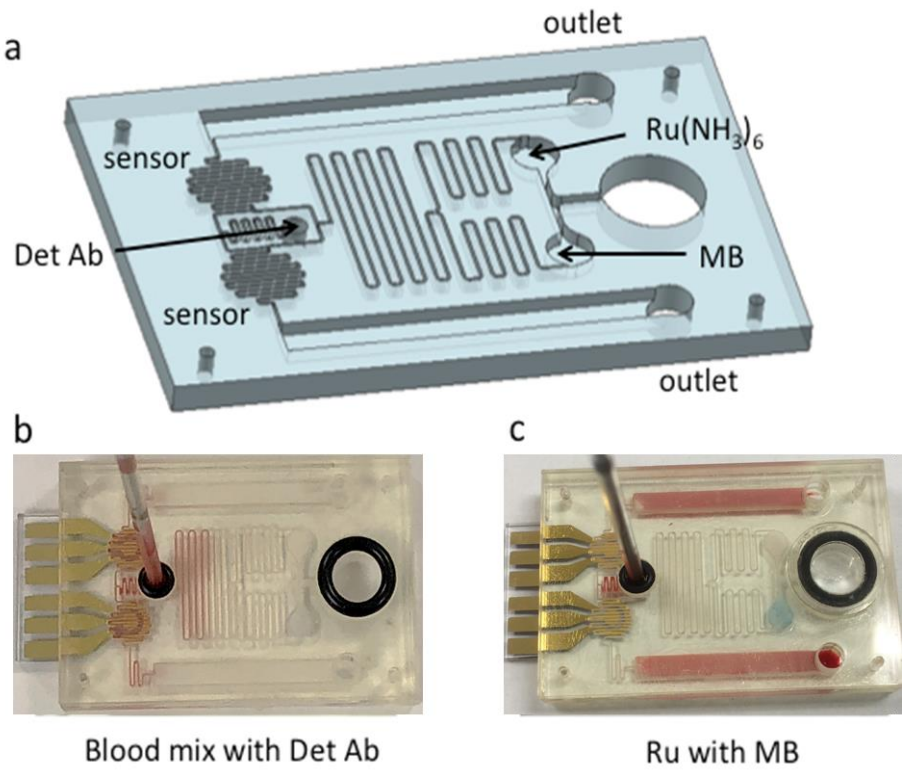

Figure 6-8. (a) Schematic of updated microfluidic cartridge design. (b) Microfluidic cartridge testing with color dye. Blood is added by capillary tube from inlet which contains detection antibody. (c) The blood sample is pumped toward the outlet, and the mixture of MB and $Ru(NH_3)_6^{3+}$ *flows to the sensor region.*

6.4.2 Device testing

The second generation mobile phone biosensing system is shown in Fig. 6-9. The updated microfluidic cartridge plugs into aMEASURE2 circuit board via an adapted connector. Step by step instructions for each step in the detection process are displayed on the mobile phone through a custom Android app interface.

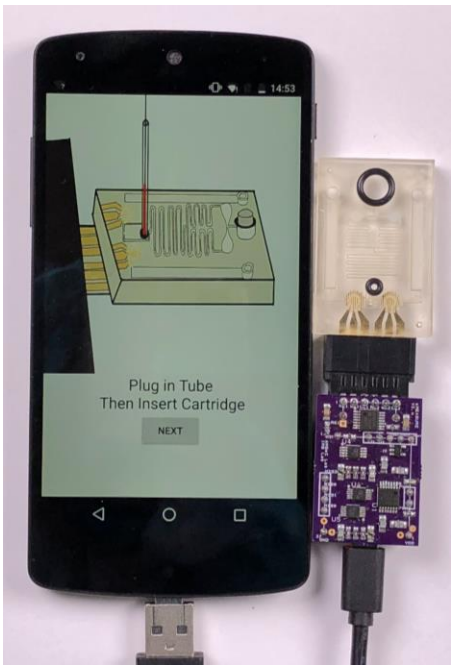

Figure 6-9. Photo of the second generation mobile phone biosensing platform. The size of sensing circuit is minimized to 2 in. × 1 in.

In order to develop a room-temperature stable microfluidic cartridge, dried reagents are required, including the detection antibody, $Ru(NH_3)_6^{3+}$ and MB. Therefore, we optimized the concentration of three reagents, respectively, and determined the optimal concentrations for each reagent is 100 μg/mL, 1mM, and 0.5 mM, respectively. To maintain the activity and formation of protein in a dry condition, the detection antibody is mixed with a 30% stabilizer solution to preserve its activity. After the optimization of the incubation steps, the reagent condition, and applied potential, a batch of microfluidic cartridges were prepared for device testing. A calibration curve (Fig. 6-10) was generated by performing measurements of human blood samples spiked with *Pf*HRP2 from 500 ng/mL to 10,000 ng/mL. Although the detection range is narrower than our first generation of microfluidic cartridge, it exhibits higher linearity ($R^2 = 0.971$) which improves the overall accuracy of this assay.

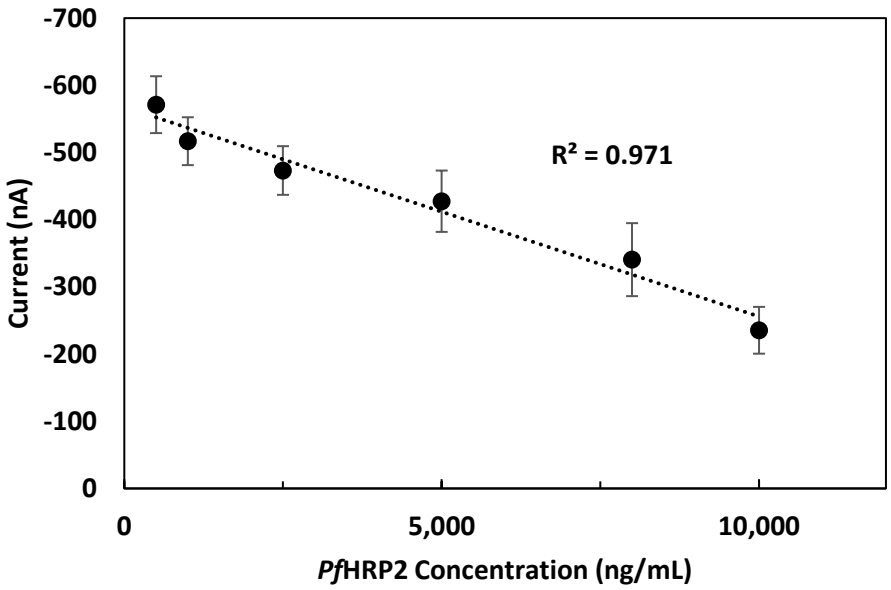

Figure 6-10. The calibration curve generated from our POC system using spiked blood samples. Each data point represents the mean ± SD of three separate measurements obtained using new cartridges.

One of advantages of the second generation microfluidic cartridge is the robustness of the assay scheme. For this scheme, the cartridge can be stored under room temperature without refrigeration due to the stability of $Ru(NH_3)_6^{3+}$ and MB. We then investigated the stability of the microfluidic cartridge performance for a longer storage period. We pre-loaded 5 µL of detection antibodies, $Ru(NH_3)_6^{3+}$ and MB in the cartridge, and stored them in a dehumidified chamber, where humidity is controlled under 30%. We performed measurements using microfluidic cartridge stored for 1 week, 2 weeks, and 1 month to investigate the cartridge stability. For each period, we tested with 1 µg/mL *Pf*HRP2 spiked in human blood using three cartridges and the results are shown in Fig. 6-11. The signals for the target and background remained stable for up to 2 weeks. However, the target signal increased at 1 month storage due to a higher electron transfer rate occurring on the surface. We suspect that the detection antibody does not exhibit the same activity after one month storage, therefore there is less protein layer formed on the electrode, resulting in a higher current

signal. Additionally, the background signal dropped ~50 to 100 nA, suggesting that the substrate activity in the cartridge slightly decreased as well. Although the SBR is decreased after 1 month of storage, the detection signal can still be distinguished from the background.

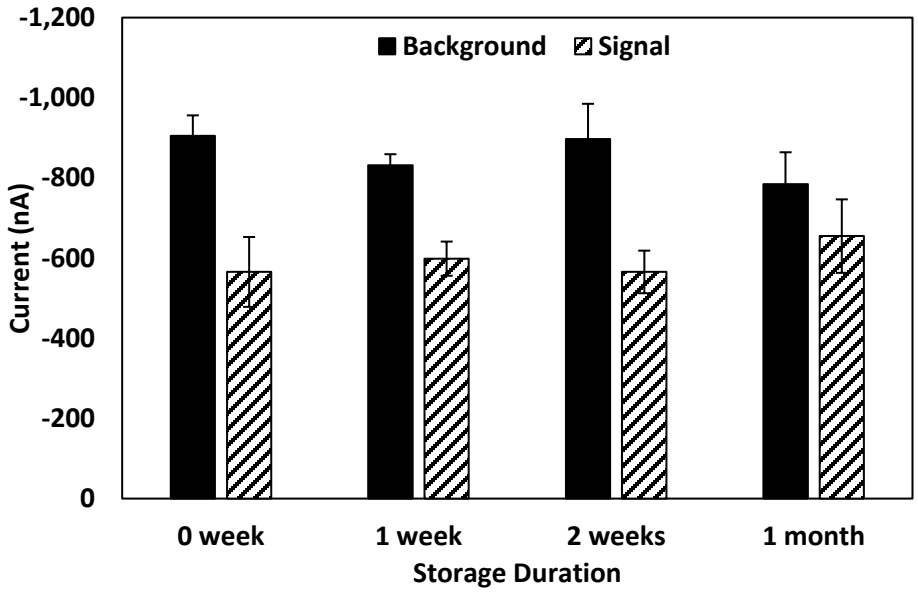

Figure 6-11. Detection current measurement for evaluating microfluidic cartridge stability at 1 µg/mL of PfHRP2 in human blood for 1 month. Each bar represents the mean ± SD of three separate measurements obtained using new cartridges.

6.4.3 Device validation

For the validation of our second generation mobile phone biosensor device, measurements were performed using the mobile phone biosensor and a commercial *Pf*HRP2 ELISA test. Cartridges were prepared for evaluating samples from 1 µg/mL to 20 µg/mL using undiluted blood samples by using capillary tubes pre-loaded with 20 µL of PBS as a dilution buffer. Therefore, the detection range of sample is expanded from 0.5 µg/mL – 10 µg/mL toward 1 µg/mL - 20 µg/mL. Measurements obtained from the ELISA test (CellLab, Australia) were taken as the gold standard. Analytical performance of our device was performed by testing 9 blood samples using both assays.

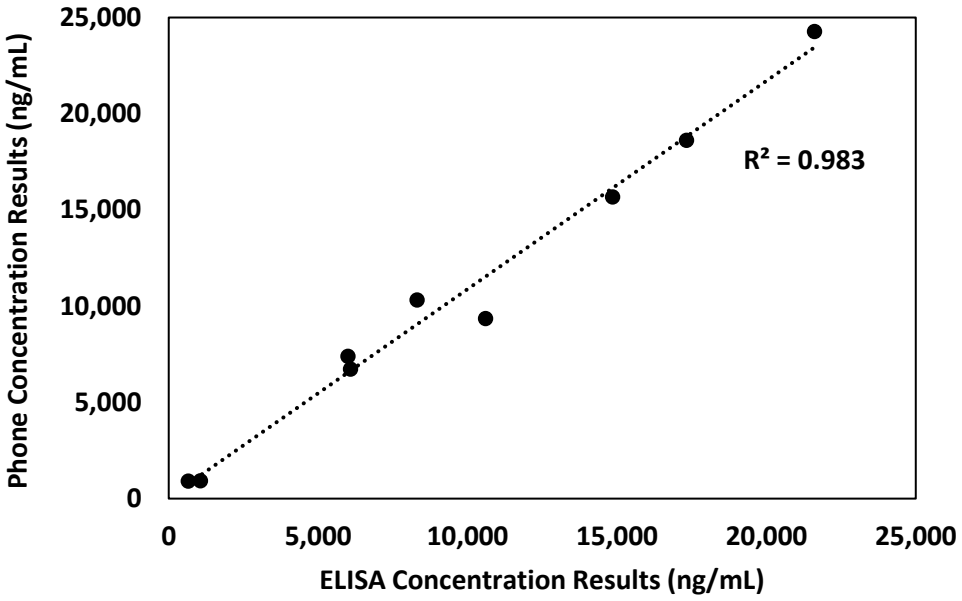

Figure 6-12. Comparison of PfHRP2 measurements of spiked blood samples using ELISA and the mobile phone device.

The result is shown in Fig. 6-12, our proposed device has a similar performance compared with ELISA for measurements of *Pf*HRP2 in spiked blood samples exhibiting good linearity (R^2 correlation coefficient = 0.984). However, there is around 1,000 ng/mL concentration difference for each measurement. Although the value on our device is not exactly same as ELISA, the signal trends of the 9 samples are similar as ELISA. These preliminary results indicate that our POC test can measure *Pf*HRP2 in spiked whole blood samples with similar accuracy as ELISA.

6.5 Summary

In this chapter, we developed two generation prototypes of a finger-powered microfluidic cartridge for rapid electrochemical measurements of *Pf*HRP2 using a mobile phone biosensor platform. For the first generation device, reagents are stored on-chip and fluid transport is accomplished via a unique piston-based pumping mechanism. This electricity-free actuation mechanism is coupled with a high sensitivity, high selectivity electrochemical assay which offers rapid measurements and a wide detection range. For proof-of-concept, this platform was used for

quantitative measurements of *Pf*HRP2 which could be detected from 0.1 µg/mL – 20 µg/mL in spiked blood samples. Each measurement is completed in ≤ 6 min which is 3× faster than our previously reported mobile phone electrochemical biosensor. However, the liquid reagents are degraded on the microfluidic cartridge, the alternative approaches for storing reagent on cartridge is necessary.

For the second generation device, we modified the design of the microfluidic cartridge to incorporate a second sensor and employed a nonenzymatic detection scheme. By using a stabilizer, reagents are dried on chip and can remain stable for up to a month at room temperature with minimal signal loss. In addition, the testing procedure is simplified from three steps to one step. For proof of concept, this platform was used for quantifying *Pf*HRP2 in spiked blood samples with high linearity from 0.5 µg/mL – 10 µg/mL. Each measurement is completed in ≤ 5 min which is faster than our previously developed biosensor in Section 6.3. The validation of this device was carried out by performing measurements of *Pf*HRP2 in spiked blood samples and comparing the results with a *Pf*HRP2 ELISA test, which showed similar analytical performance.

Chapter 7. Conclusions

7.1 Summary of achievements and contributions

In this dissertation, we investigated various strategies towards the development of plastic microfluidic devices for rapid electrochemical measurements of protein biomarkers. First, UV/ozone (UVO) surface treatment was investigated for exploring wetting stability for 16 weeks on three plastics and we noticed the storage condition has a significant impact on the surface stability. Furthermore, we then explored two approaches for fabricating plastic microfluidic devices. We demonstrated for the first time the fabrication of plastic microchannels using 3D printed metal molds. Through optimization of the powder composition and processing parameters, we were able to generate plastic microfluidic chips with similar flowing performance as device made from CNC milled. However, this technique is replaced by CO_2 ablation fabrication method due to the limited resolution. In addition, PMMA was selected as the substrate material among three materials for the microfluidic cartridge due to its stable chemical properties, and compatibility with CO_2 ablation.

Two electrochemical assays for *Pf*HRP2 with corresponding microfluidic cartridges were developed, one based on an enzymatic detection scheme and another based on a nonenzymatic detection scheme. Moreover, towards an electricity-free microfluidic assay, we developed a simple, straightforward and valveless finger-powered pump, which was integrated with two electrochemical assays. By utilizing a nonenzymatic MB-based detection scheme, the stability of microfluidic cartridge is improved with a measurement time $\leq$ 5 min, which is 3× faster than the previously reported mobile phone electrochemical biosensors [41,49]. A detection limit of 1 μg/mL is achieved for this device. Although the sensitivity is lower than previously reported mobile phone devices [41,48,49], this device exhibits a much higher linear detection range 1 μg/mL to 20 μg/mL, which is required for the diagnosis of cerebral malaria. Furthermore, this device uses whole blood samples, which circumvents complicated processing steps, such as centrifugation and dilution.

Owing to its portability, simplicity, and good analytical performance, this platform has the potential to improve POC testing worldwide, particularly in remote and resource-limited settings.

7.2 Future work

The second generation microfluidic cartridge exhibits excellent stability at room temperature for up to 1 month. By utilizing alternative methods to store dried reagents, it may be possible to extend the shelf life of the cartridge. The current generation device employs laser ablation and adhesive bonding which is simple, scalable, and reproducible. However, this approach results in slight residue on the adhesive film and PMMA surfaces. Therefore, modifying the fabrication process to minimize residue generation could improve the detection sensitivity and the limit of detection. In the current prototype device, two sensors are employed for the detection signal and a negative control. By incorporating additional sensors and modifying the microfluidic network, it may be possible to perform multiplexed measurements of multiple biomarkers using a single cartridge. This would provide more thorough diagnostic information and improve subsequent treatment and patient outcomes.

BIBLIOGRAPHY

BIBLIOGRAPHY

[1] B. Srinivasan and S. Tung, "Development and Applications of Portable Biosensors," *Jala*, vol. 20, no. 4, pp. 365–389, Aug. 2015.

[2] P. Lems-Van Kan, H. W. Verspaget, and A. S. Peña, "ELISA assay for quantitative measurement of human immunoglobulins IgA, IgG, and IgM in nanograms," *J. Immunol. Methods*, vol. 57, no. 1, pp. 51–57, Feb. 1983.

[3] D. Grieshaber, R. MacKenzie, J. Vörös, and E. Reimhult, "Electrochemical Biosensors - Sensor Principles and Architectures," *Sensors*, vol. 8, no. 3, pp. 1400–1458, Mar. 2008.

[4] J. P. Chambers, B. P. Arulanandam, L. L. Matta, A. Weis, and J. J. Valdes, "Biosensor recognition elements," *Curr. Issues Mol. Biol.*, vol. 10, no. 1–2, pp. 1–12, 2008.

[5] D. Mark, S. Haeberle, G. Roth, F. von Stetten, and R. Zengerle, "Microfluidic lab-on-a-chip platforms: requirements, characteristics and applications," *Chem. Soc. Rev.*, vol. 39, no. 3, pp. 1153–1182, Feb. 2010.

[6] G. A. Posthuma-Trumpie, J. Korf, and A. van Amerongen, "Lateral flow (immuno)assay: its strengths, weaknesses, opportunities and threats. A literature survey," *Anal. Bioanal. Chem.*, vol. 393, no. 2, pp. 569–582, Jan. 2009.

[7] K. M. Koczula and A. Gallotta, "Lateral flow assays," *Essays Biochem.*, vol. 60, no. 1, pp. 111–120, Jun. 2016.

[8] I. Diaconu, C. Cristea, V. Harceaga, G. Marrazza, I. Berindan-Neagoe, and R. Sandulescu, "Electrochemical immunosensors in breast and ovarian cancer," *Clin. Chim. Acta*, vol. 425, pp. 128–138, Oct. 2013.

[9] D. Meadows, "Recent developments with biosensing technology and applications in the pharmaceutical industry," *Adv. Drug Deliv. Rev.*, vol. 21, no. 3, pp. 179–189, Oct. 1996.

[10] E. B. Bahadir and M. K. Sezginturk, "Applications of electrochemical immunosensors for early clinical diagnostics," *Talanta*, vol. 132, pp. 162–174, Jan. 2015.

[11] A. Sassolas, L. J. Blum, and B. D. Leca-Bouvier, "Immobilization strategies to develop enzymatic biosensors," *Biotechnol. Adv.*, vol. 30, no. 3, pp. 489–511, May 2012.

[12] J. Newman and K. E. Thomas-Alyea, *Electrochemical Systems*. John Wiley & Sons, 2012.

[13] M. Culebras, C. M. Gómez, and A. Cantarero, "Review on Polymers for Thermoelectric Applications," *Materials*, vol. 7, no. 9, pp. 6701–6732, Sep. 2014.

[14] J. Wang, "Electrochemical biosensors: Towards point-of-care cancer diagnostics," *Biosens. Bioelectron.*, vol. 21, no. 10, pp. 1887–1892, Apr. 2006.

[15] X. Liu, T.-Y. Lin, and P. B. Lillehoj, "Smartphones for cell and biomolecular detection," *Ann. Biomed. Eng.*, vol. 42, no. 11, pp. 2205–2217, Nov. 2014.

[16] L. C. Clark, “MONITOR AND CONTROL OF BLOOD AND TISSUE OXYGEN TENSIONS.,” *Trans.-Am. Soc. Fro Artif. Intern. Organs*, vol. 2, no. 1, pp. 41–48, Apr. 1956.

[17] M. Liu, R. Liu, and W. Chen, “Graphene wrapped Cu2O nanocubes: Non-enzymatic electrochemical sensors for the detection of glucose and hydrogen peroxide with enhanced stability,” *Biosens. Bioelectron.*, vol. 45, pp. 206–212, Jul. 2013.

[18] N. Ruecha, R. Rangkupan, N. Rodthongkum, and O. Chailapakul, “Novel paper-based cholesterol biosensor using graphene/polyvinylpyrrolidone/polyaniline nanocomposite,” *Biosens. Bioelectron.*, vol. 52, pp. 13–19, Feb. 2014.

[19] N. J. Ronkainen-Matsuno, J. H. Thomas, H. B. Halsall, and W. R. Heineman, “Electrochemical immunoassay moving into the fast lane,” *TrAC Trends Anal. Chem.*, vol. 21, no. 4, pp. 213–225, Apr. 2002.

[20] A. Hemben, J. Ashley, and I. E. Tothill, “Development of an Immunosensor for PfHRP 2 as a Biomarker for Malaria Detection,” *Biosensors*, vol. 7, no. 3, p. 28, Jul. 2017.

[21] W. S. Bauer *et al.*, “Rapid concentration and elution of malarial antigen histidine-rich protein II using solid phase Zn(II) resin in a simple flow-through pipette tip format,” *Biomicrofluidics*, vol. 11, no. 3, p. 34115, May 2017.

[22] J. M. van Emon, *Immunoassay and Other Bioanalytical Techniques*. CRC Press, 2016.

[23] E. V. Gogol, G. A. Evtugyn, J.-L. Marty, H. C. Budnikov, and V. G. Winter, “Amperometric biosensors based on nafion coated screen-printed electrodes for the determination of cholinesterase inhibitors,” *Talanta*, vol. 53, no. 2, pp. 379–389, Nov. 2000.

[24] S. Laschi, I. Palchetti, and M. Mascini, “Gold-based screen-printed sensor for detection of trace lead,” *Sens. Actuators B Chem.*, vol. 114, no. 1, pp. 460–465, Mar. 2006.

[25] C. R. Ispas, G. Crivat, and S. Andreescu, “Review: Recent Developments in Enzyme-Based Biosensors for Biomedical Analysis,” *Anal. Lett.*, vol. 45, no. 2–3, pp. 168–186, Jan. 2012.

[26] J. S. Swensen *et al.*, “Continuous, Real-Time Monitoring of Cocaine in Undiluted Blood Serum via a Microfluidic, Electrochemical Aptamer-Based Sensor,” *J. Am. Chem. Soc.*, vol. 131, no. 12, pp. 4262–4266, Apr. 2009.

[27] M. Pumera, A. Merkoçi, and S. Alegret, “New materials for electrochemical sensing VII. Microfluidic chip platforms,” *TrAC Trends Anal. Chem.*, vol. 25, no. 3, pp. 219–235, Mar. 2006.

[28] P. N. Nge, C. I. Rogers, and A. T. Woolley, “Advances in Microfluidic Materials, Functions, Integration, and Applications,” *Chem. Rev.*, vol. 113, no. 4, pp. 2550–2583, Apr. 2013.

[29] D. C. Duffy, J. C. McDonald, O. J. A. Schueller, and G. M. Whitesides, “Rapid Prototyping of Microfluidic Systems in Poly(dimethylsiloxane),” *Anal. Chem.*, vol. 70, no. 23, pp. 4974–4984, Dec. 1998.

[30] W. Dungchai, O. Chailapakul, and C. S. Henry, “Electrochemical Detection for Paper-Based Microfluidics,” *Anal. Chem.*, vol. 81, no. 14, pp. 5821–5826, Jul. 2009.

[31] Z. Nie *et al.*, "Electrochemical sensing in paper-based microfluidic devices," *Lab Chip*, vol. 10, no. 4, pp. 477–483, Feb. 2010.

[32] M. Reches, K. A. Mirica, R. Dasgupta, M. D. Dickey, M. J. Butte, and G. M. Whitesides, "Thread as a Matrix for Biomedical Assays," *ACS Appl. Mater. Interfaces*, vol. 2, no. 6, pp. 1722–1728, Jun. 2010.

[33] D. J. Laser and J. G. Santiago, "A review of micropumps," *J. Micromechanics Microengineering*, vol. 14, no. 6, p. R35, 2004.

[34] P. Woias, "Micropumps—past, progress and future prospects," *Sens. Actuators B Chem.*, vol. 105, no. 1, pp. 28–38, Feb. 2005.

[35] C. Jönsson *et al.*, "Silane–dextran chemistry on lateral flow polymer chips for immunoassays," *Lab Chip*, vol. 8, no. 7, pp. 1191–1197, Jun. 2008.

[36] I. Beaulieu, M. Geissler, and J. Mauzeroll, "Oxygen plasma treatment of polystyrene and Zeonor: substrates for adhesion of patterned cells," *Langmuir ACS J. Surf. Colloids*, vol. 25, no. 12, pp. 7169–7176, Jun. 2009.

[37] P. M. van Midwoud, A. Janse, M. T. Merema, G. M. M. Groothuis, and E. Verpoorte, "Comparison of Biocompatibility and Adsorption Properties of Different Plastics for Advanced Microfluidic Cell and Tissue Culture Models," *Anal. Chem.*, vol. 84, no. 9, pp. 3938–3944, May 2012.

[38] J. Castillo-León and W. E. Svendsen, *Lab-on-a-Chip Devices and Micro-Total Analysis Systems: A Practical Guide*. Springer, 2014.

[39] D. S. Kim, S. H. Lee, C. H. Ahn, J. Y. Lee, and T. H. Kwon, "Disposable integrated microfluidic biochip for blood typing by plastic microinjection moulding," *Lab Chip*, vol. 6, no. 6, pp. 794–802, May 2006.

[40] K. Iwai, K. C. Shih, X. Lin, T. A. Brubaker, R. D. Sochol, and L. Lin, "Finger-powered microfluidic systems using multilayer soft lithography and injection molding processes," *Lab. Chip*, vol. 14, no. 19, pp. 3790–3799, Oct. 2014.

[41] T. Laksanasopin *et al.*, "A smartphone dongle for diagnosis of infectious diseases at the point of care," *Sci. Transl. Med.*, vol. 7, no. 273, p. 273re1-273re1, Feb. 2015.

[42] T.-S. Leu and P.-Y. Chang, "Pressure barrier of capillary stop valves in micro sample separators," *Sens. Actuators Phys.*, vol. 115, no. 2–3, pp. 508–515, Sep. 2004.

[43] H. Andersson, W. van der Wijngaart, P. Griss, F. Niklaus, and G. Stemme, "Hydrophobic valves of plasma deposited octafluorocyclobutane in DRIE channels," *Sens. Actuators B Chem.*, vol. 75, no. 1–2, pp. 136–141, Apr. 2001.

[44] M. L. Adams, M. L. Johnston, A. Scherer, and S. R. Quake, "Polydimethylsiloxane based microfluidic diode," *J. Micromechanics Microengineering*, vol. 15, no. 8, p. 1517, 2005.

[45] D. Quesada-González and A. Merkoçi, "Mobile phone–based biosensing: an emerging 'diagnostic and communication' technology," *Biosens. Bioelectron.*

[46] J. Jiang *et al.*, "Smartphone based portable bacteria pre-concentrating microfluidic sensor and impedance sensing system," *Sens. Actuators B Chem.*, vol. 193, pp. 653–659, Mar. 2014.

[47] A. F. Coskun, R. Nagi, K. Sadeghi, S. Phillips, and A. Ozcan, "Albumin testing in urine using a smart-phone," *Lab. Chip*, vol. 13, no. 21, pp. 4231–4238, Nov. 2013.

[48] C. C. Stemple, S. V. Angus, T. S. Park, and J.-Y. Yoon, "Smartphone-based optofluidic lab-on-a-chip for detecting pathogens from blood," *J. Lab. Autom.*, vol. 19, no. 1, pp. 35–41, Feb. 2014.

[49] P. B. Lillehoj, M.-C. Huang, N. Truong, and C.-M. Ho, "Rapid electrochemical detection on a mobile phone," *Lab Chip*, vol. 13, no. 15, pp. 2950–2955, Jul. 2013.

[50] K. B. Seydel *et al.*, "Plasma concentrations of parasite histidine-rich protein 2 distinguish between retinopathy-positive and retinopathy-negative cerebral malaria in Malawian children," *J. Infect. Dis.*, vol. 206, no. 3, pp. 309–318, Aug. 2012.

[51] A. Piruska *et al.*, "The autofluorescence of plastic materials and chips measured under laser irradiation," *Lab. Chip*, vol. 5, no. 12, pp. 1348–1354, Dec. 2005.

[52] S. H. Tan, N.-T. Nguyen, Y. C. Chua, and T. G. Kang, "Oxygen plasma treatment for reducing hydrophobicity of a sealed polydimethylsiloxane microchannel," *Biomicrofluidics*, vol. 4, no. 3, p. 32204, Sep. 2010.

[53] A. Bhattacharyya and C. M. Klapperich, "Mechanical and chemical analysis of plasma and ultraviolet–ozone surface treatments for thermal bonding of polymeric microfluidic devices," *Lab Chip*, vol. 7, no. 7, pp. 876–882, Jun. 2007.

[54] C. W. Tsao, L. Hromada, J. Liu, P. Kumar, and D. L. DeVoe, "Low temperature bonding of PMMA and COC microfluidic substrates using UV/ozone surface treatment," *Lab Chip*, vol. 7, no. 4, pp. 499–505, Mar. 2007.

[55] M. Malmsten, "Ellipsometry studies of the effects of surface hydrophobicity on protein adsorption," *Colloids Surf. B Biointerfaces*, vol. 3, no. 5, pp. 297–308, Jan. 1995.

[56] M. Rabe, D. Verdes, and S. Seeger, "Understanding protein adsorption phenomena at solid surfaces," *Adv. Colloid Interface Sci.*, vol. 162, no. 1–2, pp. 87–106, Feb. 2011.

[57] Y. Arima and H. Iwata, "Effect of wettability and surface functional groups on protein adsorption and cell adhesion using well-defined mixed self-assembled monolayers," *Biomaterials*, vol. 28, no. 20, pp. 3074–3082, Jul. 2007.

[58] S. Pasche, J. Vörös, H. J. Griesser, N. D. Spencer, and M. Textor, "Effects of Ionic Strength and Surface Charge on Protein Adsorption at PEGylated Surfaces," *J. Phys. Chem. B*, vol. 109, no. 37, pp. 17545–17552, Sep. 2005.

[59] H. Becker and L. E. Locascio, "Polymer microfluidic devices," *Talanta*, vol. 56, no. 2, pp. 267–287, Feb. 2002.

[60] D. J. Guckenberger, T. E. de Groot, A. M. D. Wan, D. J. Beebe, and E. W. K. Young, "Micromilling: a method for ultra-rapid prototyping of plastic microfluidic devices," *Lab Chip*, vol. 15, no. 11, pp. 2364–2378, May 2015.

[61] M. E. Wilson *et al.*, "Fabrication of circular microfluidic channels by combining mechanical micromilling and soft lithography," *Lab. Chip*, vol. 11, no. 8, pp. 1550–1555, Apr. 2011.

[62] S.-C. Wang, C.-Y. Lee, and H.-P. Chen, "Thermoplastic microchannel fabrication using carbon dioxide laser ablation," *J. Chromatogr. A*, vol. 1111, no. 2, pp. 252–257, Apr. 2006.

[63] H. Klank, J. P. Kutter, and O. Geschke, "CO(2)-laser micromachining and back-end processing for rapid production of PMMA-based microfluidic systems," *Lab. Chip*, vol. 2, no. 4, pp. 242–246, Nov. 2002.

[64] A. K. Au, W. Lee, and A. Folch, "Mail-order microfluidics: evaluation of stereolithography for the production of microfluidic devices," *Lab. Chip*, vol. 14, no. 7, pp. 1294–1301, Apr. 2014.

[65] P. J. Kitson, M. H. Rosnes, V. Sans, V. Dragone, and L. Cronin, "Configurable 3D-Printed millifluidic and microfluidic 'lab on a chip' reactionware devices," *Lab Chip*, vol. 12, no. 18, pp. 3267–3271, Aug. 2012.

[66] Y. Zhao and T. Cui, "Fabrication of high-aspect-ratio polymer-based electrostatic comb drives using the hot embossing technique," *J. Micromechanics Microengineering*, vol. 13, no. 3, p. 430, 2003.

[67] M. B. Esch, S. Kapur, G. Irizarry, and V. Genova, "Influence of master fabrication techniques on the characteristics of embossed microfluidic channels," *Lab Chip*, vol. 3, no. 2, pp. 121–127, May 2003.

[68] S. Miserere, G. Mottet, V. Taniga, S. Descroix, J.-L. Viovy, and L. Malaquin, "Fabrication of thermoplastics chips through lamination based techniques," *Lab Chip*, vol. 12, no. 10, pp. 1849–1856, Apr. 2012.

[69] L. J. Kricka, P. Fortina, N. J. Panaro, P. Wilding, G. Alonso-Amigo, and H. Becker, "Fabrication of plastic microchips by hot embossing," *Lab. Chip*, vol. 2, no. 1, pp. 1–4, Feb. 2002.

[70] J. Greener *et al.*, "Rapid, cost-efficient fabrication of microfluidic reactors in thermoplastic polymers by combining photolithography and hot embossing," *Lab. Chip*, vol. 10, no. 4, pp. 522–524, Feb. 2010.

[71] R. Novak, N. Ranu, and R. A. Mathies, "Rapid fabrication of nickel molds for prototyping embossed plastic microfluidic devices," *Lab Chip*, vol. 13, no. 8, pp. 1468–1471, Mar. 2013.

[72] Q. Xia and S. Y. Chou, "Fabrication of sub-25 nm diameter pillar nanoimprint molds with smooth sidewalls using self-perfection by liquefaction and reactive ion etching," *Nanotechnology*, vol. 19, no. 45, p. 455301, Nov. 2008.

[73] V. N. Goral, Y.-C. Hsieh, O. N. Petzold, R. A. Faris, and P. K. Yuen, "Hot embossing of plastic microfluidic devices using poly(dimethylsiloxane) molds," *J. Micromechanics Microengineering*, vol. 21, no. 1, p. 17002, 2011.

[74] G. S. Fiorini, G. D. M. Jeffries, D. S. W. Lim, C. L. Kuyper, and D. T. Chiu, "Fabrication of thermoset polyester microfluidic devices and embossing masters using rapid prototyped polydimethylsiloxane molds," *Lab Chip*, vol. 3, no. 3, pp. 158–163, Aug. 2003.

[75] T. Koerner, L. Brown, R. Xie, and R. D. Oleschuk, "Epoxy resins as stamps for hot embossing of microstructures and microfluidic channels," *Sens. Actuators B Chem.*, vol. 107, no. 2, pp. 632–639, Jun. 2005.

[76] R. K. Jena, C. Y. Yue, and K. X. Yun, "Effect of a CNT based composite micromold on the replication fidelity during the microfabrication of polymeric microfluidic devices," *RSC Adv.*, vol. 4, no. 24, pp. 12448–12456, Feb. 2014.

[77] E. W. K. Young *et al.*, "Rapid Prototyping of Arrayed Microfluidic Systems in Polystyrene for Cell-Based Assays," *Anal. Chem.*, vol. 83, no. 4, pp. 1408–1417, Feb. 2011.

[78] J. A. Olortegui-Yume and P. Y. Kwon, "Crater wear patterns analysis on multi-layer coated carbides using the wavelet transform," *Wear*, vol. 268, no. 3, pp. 493–504, Feb. 2010.

[79] M. Vaezi and C. K. Chua, "Effects of layer thickness and binder saturation level parameters on 3D printing process," *Int. J. Adv. Manuf. Technol.*, vol. 53, no. 1–4, pp. 275–284, Mar. 2011.

[80] T. Do *et al.*, "Improving Structural Integrity with Boron-based Additives for 3D Printed 420 Stainless Steel," *Procedia Manuf.*, vol. 1, pp. 263–272, Jan. 2015.

[81] S. Sandron *et al.*, "3D printed metal columns for capillary liquid chromatography," *Analyst*, vol. 139, no. 24, pp. 6343–6347, Nov. 2014.

[82] H. Becker and U. Heim, "Hot embossing as a method for the fabrication of polymer high aspect ratio structures," *Sens. Actuators Phys.*, vol. 83, no. 1–3, pp. 130–135, May 2000.

[83] L. Brown, T. Koerner, J. H. Horton, and R. D. Oleschuk, "Fabrication and characterization of poly(methylmethacrylate) microfluidic devices bonded using surface modifications and solvents," *Lab. Chip*, vol. 6, no. 1, pp. 66–73, Jan. 2006.

[84] Y. Sun, Y. C. Kwok, and N.-T. Nguyen, "Low-pressure, high-temperature thermal bonding of polymeric microfluidic devices and their applications for electrophoretic separation," *J. Micromechanics Microengineering*, vol. 16, no. 8, p. 1681, 2006.

[85] E. M. Hamad *et al.*, "Inkjet printing of UV-curable adhesive and dielectric inks for microfluidic devices," *Lab Chip*, vol. 16, no. 1, pp. 70–74, Dec. 2015.

[86] J.-Y. Cheng, C.-W. Wei, K.-H. Hsu, and T.-H. Young, "Direct-write laser micromachining and universal surface modification of PMMA for device development," *Sens. Actuators B Chem.*, vol. 99, no. 1, pp. 186–196, Apr. 2004.

[87] C.-W. Tsao and D. L. DeVoe, "Bonding of thermoplastic polymer microfluidics," *Microfluid. Nanofluidics*, vol. 6, no. 1, pp. 1–16, Jan. 2009.

[88] J. P. Gosling, "A decade of development in immunoassay methodology," *Clin. Chem.*, vol. 36, no. 8 Pt 1, pp. 1408–1427, Aug. 1990.

[89] D. Kim and A. E. Herr, "Protein immobilization techniques for microfluidic assays," *Biomicrofluidics*, vol. 7, no. 4, Jul. 2013.

[90] S. Sharma, H. Byrne, and R. J. O'Kennedy, "Antibodies and antibody-derived analytical biosensors," *Essays Biochem.*, vol. 60, no. 1, pp. 9–18, Jun. 2016.

[91] F. Darain, M. A. Wahab, and S. C. Tjin, "Surface Activation of Poly(Methyl methacrylate) by Plasma Treatment: Stable Antibody Immobilization for Microfluidic Enzyme-Linked Immunosorbent Assay," *Anal. Lett.*, vol. 45, no. 17, pp. 2569–2579, Nov. 2012.

[92] T. T. Le, C. P. Wilde, N. Grossman, and A. E. G. Cass, "A simple method for controlled immobilization of proteins on modified SAMs," *Phys. Chem. Chem. Phys. PCCP*, vol. 13, no. 12, pp. 5271–5278, Mar. 2011.

[93] A. Ahmad and E. Moore, "Electrochemical immunosensor modified with self-assembled monolayer of 11-mercaptoundecanoic acid on gold electrodes for detection of benzo[a]pyrene in water," *Analyst*, vol. 137, no. 24, pp. 5839–5844, 2012.

[94] N. R. Mohamad, N. H. C. Marzuki, N. A. Buang, F. Huyop, and R. A. Wahab, "An overview of technologies for immobilization of enzymes and surface analysis techniques for immobilized enzymes," *Biotechnol. Biotechnol. Equip.*, vol. 29, no. 2, pp. 205–220, Mar. 2015.

[95] Q. Yu, Q. Wang, B. Li, Q. Lin, and Y. Duan, "Technological Development of Antibody Immobilization for Optical Immunoassays: Progress and Prospects," *Crit. Rev. Anal. Chem.*, vol. 45, no. 1, pp. 62–75, Jan. 2015.

[96] J. Wang, G. Liu, M. H. Engelhard, and Y. Lin, "Sensitive Immunoassay of a Biomarker Tumor Necrosis Factor-α Based on Poly(guanine)-Functionalized Silica Nanoparticle Label," *Anal. Chem.*, vol. 78, no. 19, pp. 6974–6979, Oct. 2006.

[97] K. Tanaka and H. Imagawa, "Rapid and reagent-saving immunoassay using innovative stirring actions of magnetic beads in microreactors in the sequential injection mode," *Talanta*, vol. 68, no. 2, pp. 437–441, Dec. 2005.

[98] V. N. Morozov and T. Y. Morozova, "Electrophoresis-Assisted Active Immunoassay," *Anal. Chem.*, vol. 75, no. 24, pp. 6813–6819, Dec. 2003.

[99] W. J, Y. Y, Y. F, and J. H, "Electric field-driven strategy for multiplexed detection of protein biomarkers using a disposable reagentless electrochemical immunosensor array.," *Anal. Chem.*, vol. 80, no. 15, pp. 6072–6077, 2008 2008.

[100] D. Du, J. Wang, D. Lu, A. Dohnalkova, and Y. Lin, "Multiplexed Electrochemical Immunoassay of Phosphorylated Proteins Based on Enzyme-Functionalized Gold Nanorod

Labels and Electric Field-Driven Acceleration," *Anal. Chem.*, vol. 83, no. 17, pp. 6580–6585, Sep. 2011.

[101] J. Tate and G. Ward, "Interferences in Immunoassay," *Clin. Biochem. Rev.*, vol. 25, no. 2, pp. 105–120, May 2004.

[102] A. I. Alayash, R. P. Patel, and R. E. Cashon, "Redox Reactions of Hemoglobin and Myoglobin: Biological and Toxicological Implications," *Antioxid. Redox Signal.*, vol. 3, no. 2, pp. 313–327, Apr. 2001.

[103] "Pierce Traut's Reagent (2-iminothiolane) - Thermo Fisher Scientific." [Online]. Available: https://www.thermofisher.com/order/catalog/product/26101. [Accessed: 02-Jan-2018].

[104] P. Fanjul-Bolado, M. B. González-García, and A. Costa-García, "Amperometric detection in TMB/HRP-based assays," *Anal. Bioanal. Chem.*, vol. 382, no. 2, pp. 297–302, May 2005.

[105] P. A. Rogers, W. M. Chilian, I. N. Bratz, R. M. Bryan, and G. M. Dick, "H2O2 activates redox- and 4-aminopyridine-sensitive Kv channels in coronary vascular smooth muscle," *Am. J. Physiol. Heart Circ. Physiol.*, vol. 292, no. 3, pp. H1404-1411, Mar. 2007.

[106] D. B. Rye, C. B. Saper, and B. H. Wainer, "Stabilization of the tetramethylbenzidine (TMB) reaction product: application for retrograde and anterograde tracing, and combination with immunohistochemistry.," *J. Histochem. Cytochem.*, vol. 32, no. 11, pp. 1145–1153, Nov. 1984.

[107] H. J. Kang, M. A. Aziz, B. Jeon, K. Jo, and H. Yang, "Strategy for Low Background-Current Levels in the Electrochemical Biosensors Using Horse-Radish Peroxidase Labels," *Electroanalysis*, vol. 21, no. 24, pp. 2647–2652, Dec. 2009.

[108] M. Zhang and W. Gorski, "Electrochemical Sensing Platform Based on the Carbon Nanotubes/Redox Mediators-Biopolymer System," *J. Am. Chem. Soc.*, vol. 127, no. 7, pp. 2058–2059, Feb. 2005.

[109] J.-Z. Xu, J.-J. Zhu, Q. Wu, Z. Hu, and H.-Y. Chen, "An Amperometric Biosensor Based on the Coimmobilization of Horseradish Peroxidase and Methylene Blue on a Carbon Nanotubes Modified Electrode," *Electroanalysis*, vol. 15, no. 3, pp. 219–224, Mar. 2003.

[110] H. Yao, N. Li, S. Xu, J.-Z. Xu, J.-J. Zhu, and H.-Y. Chen, "Electrochemical study of a new methylene blue/silicon oxide nanocomposition mediator and its application for stable biosensor of hydrogen peroxide," *Biosens. Bioelectron.*, vol. 21, no. 2, pp. 372–377, Aug. 2005.

[111] J. Wu, Y. Yan, F. Yan, and H. Ju, "Electric Field-Driven Strategy for Multiplexed Detection of Protein Biomarkers Using a Disposable Reagentless Electrochemical Immunosensor Array," *Anal. Chem.*, vol. 80, no. 15, pp. 6072–6077, Aug. 2008.

[112] K. Iwai, K. C. Shih, X. Lin, T. A. Brubaker, R. D. Sochol, and L. Lin, "Finger-powered microfluidic systems using multilayer soft lithography and injection molding processes," *Lab Chip*, vol. 14, no. 19, pp. 3790–3799, Aug. 2014.

[113] C. Peng and Y. S. Ju, "Finger-Powered Electro-Digital-Microfluidics," *Methods Mol. Biol. Clifton NJ*, vol. 1572, pp. 293–311, 2017.

[114] K. Xu, M. R. Begley, and J. P. Landers, "Simultaneous metering and dispensing of multiple reagents on a passively controlled microdevice solely by finger pressing," *Lab Chip*, vol. 15, no. 3, pp. 867–876, Jan. 2015.

[115] L. S. Han, "Hydrodynamic Entrance Lengths for Incompressible Laminar Flow in Rectangular Ducts," *J. Appl. Mech.*, vol. 27, no. 3, pp. 403–409, Sep. 1960.

[116] K. W. Oh, K. Lee, B. Ahn, and E. P. Furlani, "Design of pressure-driven microfluidic networks using electric circuit analogy," *Lab Chip*, vol. 12, no. 3, pp. 515–545, 2012.

[117] R. J. Cornish and M. Sc, "Flow in a pipe of rectangular cross-section," *Proc R Soc Lond A*, vol. 120, no. 786, pp. 691–700, Oct. 1928.

[118] B. J. Kirby, *Micro- and Nanoscale Fluid Mechanics: Transport in Microfluidic Devices*. Cambridge University Press, 2010.

[119] C. A. Crosby and M. A. Wehbé, "Hand strength: Normative values," *J. Hand Surg.*, vol. 19, no. 4, pp. 665–670, Jul. 1994.

[120] J. H. Sung and M. L. Shuler, "Prevention of air bubble formation in a microfluidic perfusion cell culture system using a microscale bubble trap," *Biomed. Microdevices*, vol. 11, no. 4, pp. 731–738, Aug. 2009.